THE UNIVERSITY *of* EDINBURGH

COMPUTATIONAL MESOSCALE MODELLING OF CONCRETE MATERIAL UNDER HIGH STRAIN RATE LOADING

Thesis submitted in fulfilment of the requirements for the degree of Doctor of Philosophy

By

Zhenhuan Song

Supervisors:

Prof. Yong Lu

Prof. Michael Rotter

The University of Edinburgh

Feb. 2013

Declaration

This thesis, entitled “Computational mesoscale modelling of concrete material under high strain rate loading”, is submitted to the Institute for Infrastructure & Environment, The School of Engineering, The University of Edinburgh, Scotland, UK, for the Degree of Doctor of Philosophy.

The research, on which this thesis is based, was carried out between May 2008 and August 2011 under the supervision of Professor Yong Lu. It is solely the work of the author except where otherwise acknowledged in the text. It has not formed the basis of a submission for any other degree.

Several publications have been produced based on this thesis project, including:

- **Song, Z.H.** and Lu, Y. (2011). Mesoscopic analysis of concrete under excessive high strain-rate compression and implications on interpretation of test data. *Journal of Impact Engineering*, 46.

- **Song, Z.H.** and Lu, Y. (2011). Numerical simulation of concrete confined by transverse reinforcement. *Computers and Concrete*, 8(1).

- **Song, Z.H.** and Lu, Y. (2011). An algorithm for generation of 3D meso-structure of concrete for finite element analysis. 19th Association of Computational Mechanics for Engineering Conference. Edinburgh, UK.

- **Song, Z.H.** and Lu, Y. (2010). Concrete response to higher strain rate compression using mesoscopic analysis. The First International Conference of Protective Structures. Manchester, UK.

- Lu, Y. and **Song, Z.H.** (2011). A mesoscopic modelling perspective of response of concrete to high strain-rate loading. Eighth International Conference on Structural Dynamics. Leuven, Belgium.

- Lu, Y., **Song, Z.H.** and Tu, Z.G. (2010). Analysis of dynamic response of concrete using a mesoscale model incorporating 3D Effects. *International Journal of Protective Structures*, 1(2).

- Lu, Y., **Song, Z.H.** and Tu, Z.G. (2009). Numerical simulation study of the strain rate effect on concrete in compression considering material heterogeneity. 9th Int. Conf. on the Mechanical and Physical Behaviour of Materials under Dynamic Loading. Brussels, Belgium.

- Lu, Y., **Song, Z.H.** and Tu, Z.G. (2009). Mesoscale analysis of concrete material under dynamic loading, International Workshop on Structures Response to Impact and Blast. Haifa, Israel.

Signed:

Zhenhuan Song

University of Edinburgh

Date submitted:

Abstract

Cement-based composite materials are widely used in engineering applications. The strength and damage patterns of such materials depend upon the properties of the constituent components as well as the microstructure. Three scale levels are generally recognized in the analysis of the mechanical behaviour of composites, namely, macro-scale, meso-scale, and nano- or atomistic scale. Modelling of the mechanical properties at the meso-level provides a powerful means for the understanding of the physical processes underlying the macroscopic strength and failure behaviour of the composite materials under various loading conditions.

This thesis endeavours to develop effective and efficient mesoscale models for cement-based composites, especially concrete, with a focus on dynamic analysis applications and in a three-dimensional stress-strain environment. These models are subsequently applied to investigate the intrinsic microscopic mechanisms governing the behaviour of such material under complex and high rate loadings, such as those due to shock, impact and blast.

To cater to the needs of dynamic analysis under complex stress conditions, a general 2-dimensinal (2D) mesoscale modelling framework is further developed with the incorporation of the 3-D effect. This framework integrates the capabilities of MATLAB programming for the generation of the mesoscale geometric structure, ANSYS-CAE for finite element mesh generation, and the hydrocode LS-DYNA for solving the dynamic response of the model. The 3D effect is incorporated via a novel pseudo-3D modelling scheme such that the crucial lateral confinement effect during the transient dynamic response can be realistically represented.

With the above mesoscale model a comprehensive investigation is conducted on the dynamic increase factor (DIF) in the concrete strength under compression, with particular focus on the variation trend at different strain rate regimes, and the key influencing factors. The wave propagation effect under high strain rate is scrutinised from a strip-by-strip perspective, and the correlation between the externally measured stress-strain quantities and the actual processes within the specimen is

examined. The contribution of the material heterogeneity, as well as the structural effect (inertia), in the dynamic strength enhancement is evaluated.

The classical Brazilian (splitting) test for the dynamic tensile behaviour of concrete is also investigated with the aid of the mesoscale model. Of particular interest here is the validity of such an indirect setup in reproducing the tensile behaviour of the specimen under high strain rates, as well as the effect of the heterogeneity in the dynamic tensile strength. Complications are found to arise as the loading rate increases. The change of the damage patterns with increase of the loading rate and the implications on the interpretation of the results are discussed.

As an ideal solution to modelling of the 3-D effects, a methodology for the creation of a complex real 3-dimensional mesoscale model is put forward in the last part of the thesis. A geometric concept, called convex hull, is adopted for the representation of aggregates, and this makes it possible to utilize the relevant algorithms in computational geometry for the present purpose of generation of random 3-D aggregates. A take-and-place procedure is employed to facilitate the generation of the complete 3-D meso-structure. Associated techniques are developed for fast detection of particle inclusion-intersection. An example 3D mesoscale model is presented and representative numerical simulations are carried out to demonstrate the performance of the 3-D mesoscale modelling scheme.

Acknowledgements

There are too many people I owe my gratitude to when this thesis finally reaches its completion. Particularly, utmost thanks to my supervisor Prof. Yong Lu. It is utterly impossible to finish this thesis without his skilful supervision: his in-depth insight to the field and broad range of knowledge ensured that my research always goes in the correct direction and that any problems encountered are solved in an appropriate way. His logical way of thinking and a global perspective in problem-solving have been a great value for me.

I would like to thank Dr Zhenguo Tu, Dr Lei Mao and Dr Xiaoqin Li for their invaluable suggestions and constructive discussions during my study. I would also like to thank Prof. Michael Rotter, my second supervisor, and the friends and colleagues at the University of Edinburgh for their help and support.

I owe my loving thanks to my wife Sherlly Li and my son Ruoshui Song. They have sacrificed a lot due to my research abroad. A special gratitude is due to my parents and parents-in-law for their loving support.

The financial support of the University of Edinburgh is gratefully acknowledged.

Table of Contents

Chapter 1: Introduction

1.1 Background

The effects of strain rate on the strength of concrete-like materials have been recognized and investigated for many years. Experimental studies tend to suggest that the apparent compressive strength of concrete increases more gradually up to a transitional strain rate of about $30s^{-1}$. Beyond this strain rate, much steeper increase occurs, and this effectively divides the relationship between the so-called dynamic increase factor (DIF) and the strain rate into two distinctive regimes. The apparent tensile strength of concrete also exhibits a similar increase trend with the strain rate although the magnitude of the strength enhancement and the transitional strain rate are different from those in compression.

The above described apparent strain rate effects have generally been adopted in the design of concrete structures subject to high strain rate loadings such as impact and blast. However, debate has been continuing over decades with regard to the mechanisms underlying such an apparent strain rate enhancement on concrete-like quasi brittle materials, and the extent to which the rate effects may be considered as material properties or may indeed be attributable to the dynamic structural effect at the test sample size scale.

Historically the strain rate behaviour of concrete was firstly deemed to be a material property based on experimental data, typically using the Split Hopkinson Pressure Bar (SHPB) apparatus. However, due to the limited instrumentation in such tests, the experimental data have been subjected to considerable limitation. For instance, the stress state in a specimen cannot be fully evaluated. To complement the physical tests, more recent investigations tend to resort increasingly to numerical methods. Using advanced computational techniques, the latest researches tend to consistently demonstrate that the compressive strain rate effect is by large caused by the lateral inertia confinement within the specimen rather than a material property. The dynamic tensile strength enhancement, on the other hand, appears to have very little to do with a specimen level structural dynamic effect.

It has to be pointed out, however, that the numerical simulation output under the complex condition of high strain rate loading could be rather susceptible to the model assumptions, chiefly the material constitutive descriptions, the boundary and loading conditions, and whether or not a realistic 3-dimensional environment is represented. Moreover, as the strain rate increases the transient stress wave effect becomes more significant and this in turn brings about a presumably more significant effect from the material heterogeneity. These factors have not been comprehensively addressed in many numerical simulation based high strain rate studies.

Another important issue to note is that dynamic tensile testing of brittle materials is usually difficult to perform due to the difficulties in imposing the desired boundary and tensile loading conditions. Among the tensile testing methods, the splitting tensile test (also called Brazilian test) has been used rather commonly as this method makes it relatively easier to acquire more accurate measurements. However, the formulation that links the applied splitting force and the developed tensile stress is originally derived from a static loading condition. In dynamic testing the validity of this relationship would become conditional; however, a thorough examination of this has been lacked.

To address those unresolved issues in high strain rate effect using a numerical approach, a comprehensive modelling framework is required. Given the anticipated increase in the stress wave effect, the requirement on the scale of observations, and hence the level of modelling, becomes a critical consideration. Three scale levels are generally recognized in the analysis of the mechanical behaviour of composites, namely, macroscale, mesoscale, and nano- or atomistic scale. In the classical numerical models, materials are presented as a continuum and its behaviour is considered using a macro, homogenised description. Modelling of the mechanical properties at the mesoscale provides a powerful means for the understanding of the physical processes underlying the macroscopic strength and failure behaviour of the composite materials under various loading conditions. Being a mixture formed of cement, aggregate, sand, water and other additives, concrete shows typical multi-scale properties. At the nano-scale (10^{-9}-10^{-6}m), cement grains such as Calcium silicate hydrate (C-S-H) and Calcium hydroxide (C-H) can be observed. Zooming the

observations to mesoscale (10^{-3}m), coarse aggregates, sand and large pores can be distinguished. In a multi-level modelling approach, it is generally acknowledged that the material behaviour at a certain scale level could be explained by the structure at a lower level (van Mier, 1996). Insight into the mesoscale behaviour, such as interaction between aggregate and mortar matrix, and the comparison with macroscopic behaviour is deemed to be a viable means to study the dynamic behaviour of concrete-like materials.

1.2 Objectives and scope

This research aims to develop effective and efficient mesoscale models for cement-based composites, especially concrete. These models are subsequently applied to investigate the intrinsic mesoscopic mechanisms governing the behaviour of this type of composite materials under complex and high rate loadings, such as those due to shock, impact and blast.

To cater to the needs of dynamic analysis under complex stress conditions, a general mesoscale modelling framework developed earlier in this research group is extended. The general framework integrates the capabilities of MATLAB programming for the generation of the mesoscale geometric structure, ANSYS-CAE for finite element mesh generation, and the hydrocode LS-DYNA for solving the dynamic response of the model. With a successful implementation of the above mesoscale modelling framework for 2-dimensional analysis of concrete material, the present study extends the 2D model to a novel pseudo-3D setting so that the crucial lateral confinement effect during the transient dynamic response can be realistically represented.

The pseudo-3D mesoscale model is applied to study the dynamic behaviour of concrete under high strain rate loading. To allow for a direct comparison with the dynamic experimental data, which are usually obtained from the SHPB tests, applying appropriate boundary conditions in the numerical model is also carefully examined. A strip-wise investigation is conducted on the spatial distribution of the dynamic response in a sample specimen, with a particular focus on the variation trend at different strain rate regimes, and the key influencing factors. The

contribution of the material heterogeneity in the dynamic strength enhancement is evaluated.

Besides the dynamic behaviour under compression, the tensile behaviour of concrete is also investigated, with a particular focus on the performance and validity of the Brazilian splitting set-up for testing the tensile strength under high strain rates.

For more realistic simulation of concrete using a mesoscale model, a real 3-dimensional mesoscale modelling methodology is developed. In this approach, the 3D random aggregate particles are represented as 3D convex hulls, and this converts the 3D meso-structure generation to a computational geometry problem. Special strategies are recommended to increase the computational efficiency, and preliminary simulations using the real 3D mesoscale model are carried out to demonstrate the performance of this complex modelling scheme.

1.3 Organization of the thesis

After a general introduction of the research (Chapter 1), Chapter 2 presents a review study of the literature with an aim to identify key issues in the understanding and analysis of the high strain rate effects of concrete where further research is required. The review of more specific techniques concerning each topical area is incorporated in the respective individual chapter.

In Chapter 3, the development of a pseudo 3D mesoscale modelling framework is presented. The necessity of ensuring a 3D stress environment in the high strain rate simulations and the pseudo-3D treatment are described in detail. Specific considerations on the key issues in the mesoscale modelling, such as the meso-structural geometry, material models, and the modelling of fracture, are discussed. The model is validated against general experimental observations. A parametric study is given at the last part of this chapter.

Chapter 4 is dedicated to an investigation into the progressive failure phenomenon under compression in the higher strain rate regime and the implications on the interpretation of the test data. A strip-wise examination of the response throughout a sample specimen is performed. A verification study of simulating the SHPB test

condition by applying a velocity boundary in the numerical simulation is also included. Three strain rate levels are chosen for examining the transient response in the mesoscale model, namely, 50 s^{-1} , 100 s^{-1} and 200 s^{-1} to represent "critical strain rate" and two levels of “excessive” strain rates. The classical theory of the SHPB test is discussed in light of the simulation results. In the last part of this chapter, the contribution to the dynamic strength enhancement from the stronger aggregates is evaluated.

Chapter 5 deals with the dynamic tensile behaviour in a splitting test configuration. It begins with a review of split testing methodologies. Different numerical splitting models are then set up to simulate the loading condition for dynamic tension. Results at selected strain rates are compared to examine the change of the tensile stress distributions with increase of the nominal tensile strain rate. An upper strain rate limit for dynamic splitting tension test of concrete-like materials is emphasised.

Chapter 6 presents the development of a real 3D mesoscale model and some preliminary simulation results using such a model. A geometric concept, called convex hull, is adopted for the representation of geometry of the aggregates, and this makes it possible to utilize the relevant theorems and algorithms in the field of computational geometry. A take-and-place procedure is employed to facilitate the generation of the complete meso-structure. Associated techniques are developed for fast detection of particle inclusion-intersection. Meshing of the whole 3D meso-structure and identification of the ITZ elements from the generated mesoscale model mesh is also briefly discussed. Finally an example of simulation using the 3D mesoscale model is provided.

Chapter 7 summarizes the main conclusions and recommendations of further research.

Chapter 2: Literature review

For brittle and quasi-brittle materials like concrete subjected to high strain-rate loading, the apparent strength has been observed to increase dramatically with the strain rate. This high rate effect has drawn wide interests in the shock and impact engineering community. A dynamic increase factor (DIF), i.e. the ratio of dynamic strength to static strength, is commonly used to gauge the nominal strength enhancement for engineering applications, particularly the design and analysis of protective structures. The material high strain-rate effect is typically described by a DIF versus strain rate relationship.

The intention of this chapter is not to present an exhaustive review of research on the concrete behaviour under high strain rates; instead it will focus on a few major topics which define the scope of this thesis. The review of more specific technical literature will be incorporated in the individual chapters.

This literature review commences with experimental studies of high rate effects and empirical formulations based on experimental observations. This is followed by a review of more recent studies on the possible mechanisms affecting the DIF, using primarily a numerical simulation approach. Typical modelling methods used for such analyses will be summarised. In the last section, different types of microscopic modelling methods are compared and discussed, with an emphasis on the continuum-based modelling techniques and the relevant issues such as geometry generation and fracture modelling.

2.1 Experimental studies of high strain rate effects

Laboratory experimentation of dynamic response of concrete was developed at first to serve the purpose of analysis of military structures. The fundamental requirements on the experimental equipment must reflect the following aspects in a realistic manner: 1) structural confinement; 2) load magnitude; and 3) duration of stress change (Tedesco and Landis, 1989). The test of dynamic strength may be conducted using various test devices and procedures. For compressive response, the dynamic

plate impact test can be used to obtain response in relative low stain rate (John et al., 1992). The Split Hopkinson Pressure Bar (SHPB) equipment, which was firstly developed to test dynamic response of metallic materials (Davis and Hunter, 1963; ASM Handbook, 2000), is perhaps the most commonly used technique for testing concrete-like materials at high strain rates. More choices exist for testing the dynamic tensile properties of such materials as it requires a relatively low loading rate for the material to develop high strain-rate tensile response. Apart from the direct tensile test, spalling test is also used by researchers, where the pressure bars are configured such that a tensile wave is developed after reflection at the end of the specimen (Brara et al., 2001). Another widely used approach is splitting test (Brazilian test), which is originally used for testing static tensile strength of brittle materials.

One of the earliest investigations of concrete dynamic strength was conducted by Mellinger and Birkimer (1966). In their research, the tensile strength of plain concrete cylinder (10 inches long and 2 inches in diameter) was measured from reflected tensile wave. The tensile DIF was found between 4.5 and 8.1 at a strain rate of $23s^{-1}$.

Ross et al. (1991; 1995; 1996) carried out several tests both on compressive and tensile responses. The dimensions of the concrete cylinders used in the tests were 1.75 ~ 2 inches long and 0.75 ~ 2 inches in diameter. A bilinear DIF curve on a DIF vs. logarithm of strain rate plot was constructed both in compression and in tension based on the experimental results. The DIF increases significantly when the strain rate is beyond a turning point. The transitional strain rate between the two segments of the DIF curve occurs at $10s^{-1}$ for compression and $1s^{-1}$ for tension. Similar bilinear DIF curves were also identified in other researches (e.g. Weerheijm and Reinhardt 1989; John et al., 1991).

Based on the regression of experimental results, empirical formulas were developed as a simple way to quantify the dynamic strength increase. Among these formulas, the most widely referenced ones include the CEB model (CEB, 1990), which has the background of Reinhardt's data (Reinhardt, 1985), and the models proposed by Ross (1991) and John et al. (1991). All these models share the common

two-segmental trend in the compressive DIF curve. The transitional strain rate in the tensile DIF however is different in the CEB model (same as compression, i.e. $30s^{-1}$) from the Ross's or John's models (order of $1s^{-1}$). Full details of the empirical formulas will be given in Chapter 4.

Despite a similar overall trend, high variance exists in the test conditions and the test data from different researches. In an earlier review of high strain rate tests by Bischoff and Perry (1991), some experimental data were questioned and it was argued that these data might have been wrongly interpreted. It was also argued that the sharp increase in the compressive DIF curve might be due to a change in the specimen stress state rather than a real material stress-strain effect. In a later review of experimental data collected by Malvar and Crawford (1998), it was highlighted that there exists a significant gap between the upper bound and the lower bound of the test data and this gap becomes more evident when strain rate goes higher. For instance, at a strain rate of around $50s^{-1}$, the compressive DIF varies in a large range of 2~7.

One uncertainty in the test data arises from the validity of SHPB types of tests and the interpretation of test measurements. In the classic theory of SHPB test, one-dimensional wave propagation is assumed and test sample is expected to be in a uniform stress state before reaching failure (Davis and Hunter, 1963; ASM Handbook, 2000; Li and Meng, 2003). For high dynamic tests, this would translate to a limit on the dimension of the test specimens for a particular level of target strain rates. On the other hand, however, to represent concrete materials which contain large heterogeneity (aggregates), the dimension of the sample specimens cannot be reduced freely to just satisfy the high strain rate requirement. The smallest diameter seen in the literature is 0.5 inch (John et al., 1991), and the typical length varies from 2 inches to 10 inches. The thickness of concrete disk used in John's splitting test was 0.25 inch. In the smaller range of above mentioned sizes, concrete is hardly to preserve its property as a mixture of aggregates and mortar; furthermore, even at the smallest end of the above size range, the strain rate that may be achieved in a "valid" manner is still limited and well below the highest strain rates reported in the experimental literature. Therefore, this relationship between the strain rate limit and

the size of the sample specimen needs to be carefully examined, and appropriate interpretation should be put in place on the test results that may be deemed as not strictly satisfying the size-rate limitation.

2.2 Recent numerical investigations to DIF

As mentioned above, the dynamic tests for high strain rate effect of concrete materials have shown an increasing trend in the DIF curve; however, questions remain on the validity of the test conditions and the achieved stress state within the specimen, especially for the test data in the higher strain rate range. Furthermore, the need on explaining the mechanisms underlying the experimentally observed apparent high rate effect also needs to be addressed.

More recent theories incline to attribute the dynamic compressive strength enhancement to the dynamic response of test samples, especially the lateral inertia induced confinement. This theory can be traced back to Brace and Jones (1971) and has been supported by several analytical and numerical studies. For example, in a recent finite element analysis of dynamic compression test of concrete specimens in a SHPB setting (Li and Meng, 2003), it was concluded that the DIF obtained from such tests could be almost entirely attributed to the lateral inertia confinement, especially for strain rate above $100s^{-1}$. In contrast to compressive DIF, it is generally understood that the tensile strength enhancement has more to do with the micromechanical processes, i.e., at the composite material property level rather than a sample-wide structural effect.

Numerical modelling presents a potentially powerful tool for the analysis of problems that remain unclear from the experimental front. Yet modelling of the mechanical behaviour of concrete has been a classical challenge. For dynamic loading, modelling of concrete is further complicated due to the transient stress wave effect. In most engineering applications concrete is modelled as homogeneous continuum having the macroscopic material properties as derived from standard concrete samples. When it comes to modelling of complex phenomena involving micro-meso scale processes, the use of a homogenised model will be insufficient. Thus, more recently a lot of effort has been spent on developing enhanced

approaches to take the micro/mesoscopic structure of the materials into account, in particular the mesoscale models. An overview of different types of the mesoscale models will be given in Section 2.3. In this section, focus is given to a review of numerical investigations into the high strain rate effect using various modelling approaches.

Georgin et al. (1998) simulated the dynamic compression behaviour of concrete with a cylindrical specimen on which velocity boundaries were imposed. Both hydrostatic stress independent and dependent constitutive models were used in the simulation. The results showed that confinement can be developed in a hydrostatic-stress dependent model, leading to an apparent strength increase in the specimen.

Donze et al. (1999) presented a 3D discrete element method (DEM) based numerical model to analyze the concrete rate dependency behaviour under compressive loading. The simulation of a SHPB test showed a good agreement between experimental and numerical data without considering any viscosity effect (a rate dependent feature) in the material description, indicating that the experimental observation of strength increase could be attained simply by the dynamic effect within the sample structure.

In the study of Park et al. (2001), the response of concrete and mortar under high strain-rate impact loading were analyzed using dynamic finite element simulations. A mesoscale model accounting for two phases, i.e. aggregate and mortar was constructed in the simulation of a plate impact test. The two constituent phases were characterized with an extended Drucke Prager model considering rate-sensitivity. The computed results showed that the dynamic strength increases with the aggregate volume fraction, and an increase of approximately 30% over that of mortar was observed in the case of an aggregate volume fraction of 42%.

Li and Meng (2003) conducted a 3D numerical simulation of SHPB apparatus. They showed that the presence of the lateral inertia confinement plays a dominant role in causing an apparent increase of DIF under compression. It was indicated that the effect of the inertia-confinement induced DIF becomes significant when the nominal strain rate exceeds around $100s^{-1}$.

A numerical study carried out by Cotsovos and Pavlovic (2007) through a 3D FEM model of prismatic concrete specimen suggested that the loading rate sensitivity is attributable primarily to the effect of both lateral and axial inertia. The study also argued that concrete sample specimens should be viewed as a "structure" as they do not constitutes a uniform material unit under dynamic loading.

Regarding the dynamic tensile strength, Hughes et al. (1993) performed a numerical study on the splitting tensile experiments. A SHPB splitting set-up (including both incident and transmitter bars) was simulated by a 2D FEM model using ADINA. The concrete constitutive model has a provision for incorporation of a DIF by raising the tension cut-off value. The study found that varying the tension cut-off greatly affects the cracking pattern and the mode of failure, and raising the tensile cut-off does enable the simulated results to resemble more closely the measured dynamic response.

Ruiz et al. (2000) investigated the tensile damage using the cohesive theory of fracture. The dynamic behaviour was simulated from a numerical splitting test in a SHPB set-up. The cohesive properties were to be rate dependent. It was found that the simulation could capture closely the experimentally observed rate sensitivity in the simulated case with a strain rate at about $30s^{-1}$.

Brara et al. (2001) presented a study of the dynamic tensile strength using both experimental and numerical approaches. In the comparative numerical simulation a 2D DEM method was employed. The experiment was performed by means of a pressure bar apparatus. The dynamic strength was found to be about 10 times of the quasi-static value at a strain rate of $120s^{-1}$. It was also demonstrated that the rate sensitivity can be captured by a cumulative fracture criterion in the DEM model.

The rate dependent tensile behaviour was also investigated by Dong et al. (2006) using a smooth particle hydrodynamic (SPH) based meshfree method In a recent research by Zhou and Hao (2008), a simplified mesoscale model was adopted to perform the analysis of dynamic behaviour under splitting tensile loading condition. The crack pattern and the tensile strength were found to be dependent upon the properties of the interface transition zone (ITZ) and the positions of the idealised

aggregates. It was also found that including the DIF into the material description highly affects the numerical results.

In summary, with the assistance of numerical simulation studies, it appeared to be generally established that the mechanisms underlying the experimentally observed DIF in compression for concrete-like materials are largely attributable to the sample-wide structural effect, particularly the inertia confinement. On the contrary, the rate dependency of the dynamic tensile strength appears to have very little to do with such structural dynamic effect and therefore may only be associated with micromechanical processes including the visco-elasticity and micro fracture growth within the composite structure.

The heterogeneous property of concrete microstructure increases the complexity of the dynamic behaviour of concrete-like materials. Studies considering the non-homogeneity in concrete (Park et al., 2001; Zhou and Hao, 2008) suggested that the presence of aggregates tends to play a part in the increase of the dynamic strength.

2.3 Mesoscopic numerical modelling

Most of the models containing meso-level features of concrete in the literature focus their attention on the study of fracture patterns and stress-strain relationship under static loading. A few of them extended the discussion into the analysis of high strain rate behaviour (e.g. Donze et al. 1999; Wriggers and Moftah. 2006; Zhou and Hao, 2009).

In general, the meso-level models may be broadly divided into the following three groups: lattice-based models, particle models (DEM), and continuum FEM models.

Lattice models are characterized by representing the continuum with a lattice of beam elements, generally connected in triangular shapes (Schlangen and van Mier, 1992; Lilliu and van Mier, 2003; van Mier and van Vliet, 2003). These elements range from simple truss to comprehensive beam type with the ability to transfer moments, axial and shear forces. In order to describe different phases in concrete, the geometry of aggregates and mortar matrix may be overlaid on top of the structure of

beam elements, thus allowing for the assignment of different mechanical properties for beams falling into the aggregate, mortar matrix or ITZ domains.

More advanced lattice models have been achieved, e.g. in the works of Bolander et al. (1999, 2000) and Cusatis et al. (2006). Bolander formulated an irregular random lattice model with shear transfer between particles, in which the lattice geometry is obtained by means of Voronoi tessellation. Their work is remarkable for the simulation of cracking of entire structures. Cusatis adopted the Delaunay triangulation of the aggregate centres to obtain the lattice structure, and the aggregate centres are generated randomly according to a specified volumetric distribution of aggregates.

The use of the so called particle models was first introduced for concrete by Bazant and his co-workers in their Microplane series models (Zubelewicz and Bazant, 1987), based on some ideas of the Distinct Element Method (DEM). From the viewpoint of the numerical analysis, the nature is similar to the lattice models described in the previous section, in the sense that in both cases the resulting system is a complex beam structure. The main advantage of these particle models is that they are computationally more efficient and, despite a greatly reduced number of unknowns, can still capture the essential aspects of material heterogeneity.

The third category of mesostructural model is the continuum mechanics based approach. Most of the early mesoscale studies of concrete ("numerical concrete") belong to this group (Roelfstra et al., 1985; Vonk, 1992; Wang et al., 1999) and this approach is also the basis of the current research. Recent advances of mesoscale studies focus particularly on the improvement of the meso-structure of concrete (Wang et al., 1999; Wriggers and Moftah, 2006; Hafner et al., 2006). An overall improvement in the model performance has been obtained through more realistic component geometry and the material descriptions, as well as modelling of interface transition zone (ITZ) between matrix and aggregates.

One major advantage of these mesoscale models is that they allow the individual constituent materials in the composite to be represented in a more realistic fashion. In the development of a mesoscale model, the geometry generation is a crucial task,

since it determines the capability to capture the heterogeneous nature of the composite material. At the same time, high irregularity and sharp transitions in the geometry of the meso-structure must also be controlled so as to avoid ill-conditioned problem due to irregular mesh shape.

One popular method for generating the distribution of aggregates is the take-and-place method, which has been adopted and improved in previous studies (Wang et al., 1999; Hafner et al., 2003; Wrigger and Moftah, 2006). In this method, the generation of geometry for an individual aggregate particle and its layout in a concrete volume are performed separately. In the take-procedure, a polygon with randomly generated vertexes is generated to represent the aggregate particle. The size distribution of aggregate shape follows a pre-defined grading curve. The polygon is then randomly placed to the concrete space in the place-procedure. An alternative method is the Voronoi/Delaunay tessellations (Carol et al., 2000; Caballero et al., 2006). In this approach, a random distribution of points is generated in the space to represent "centres" of aggregate particles. Voronoi/Delaunay tessellations are then applied to partition the space. All polyhedrons so created are then shrunk by a factor to form individual aggregate particles and the rest of the space is filled up with mortar.

In the mesoscale modelling studies reported in the literature, various shapes have been considered to represent the aggregates, from simple spherical or ellipsoidal shapes to sophisticated polygons. Improved geometric features may be obtained by for instance adding sinus functions to an ellipsoid (Hafner et al., 2003). Mesoscale models with polygon aggregates created using the take-and-place procedure have been generally limited to 2D analysis (e.g. Wang et al., 1999). This approach allows for a prescribed aggregate size distribution to fit, e.g., a Fuller-type curve. However, extension of this approach of generating the polygons to 3D is not a simple task and it involves challenging computational complexities. Using the Voronoi/Delaunay tessellations approach, on the other hand, polygons may be generated in a natural process and in shapes closer to natural aggregates (Caballero et al., 2006), but it is difficult to control the size distribution with the Voronoi polygons. Thus, generating

3D mesoscale model with realistic polygon aggregates in a well controlled manner becomes one of the tasks in the present study.

Chapter 3: Development of pseudo 3D mesoscale model for dynamic compressive response analysis

Remember that all models are wrong; the practical question is how wrong do they have to be to not be useful.

(Empirical model-building and response surfaces, P74)

--George E. P. Box (Statistician, 1919-)

3.1 Introduction

The mechanical behaviour of cement-based materials like concrete is complicated by a combination of brittleness, micro-fracture, heterogeneity, among other factors. As seen from Chapter 2, in general applications concrete is usually described as a homogeneous material with homogenized material properties derived from standard concrete sample tests. For dynamic loading, a dynamic increase factor (DIF) (e.g. CEB-FIP, 1993; Malvar and Crawford, 1998) is usually incorporated to account for the bulk strength enhancement in the high strain rate regime as observed experimentally from high strain rate tests such as using the Split Hopkinson Pressure Bar (SHPB) apparatus (Bischoff and Perry, 1991) .

On the strain rate dependency of concrete, there seems to be little doubt about the increase of the engineering or nominal strength as measured from SHPB sample tests in the high strain rate regime; however, questions remain with regards to the underlying mechanisms, as to whether such an increase should be considered as a material character, or indeed it is due to the dynamic effect within a test sample (Li and Meng, 2003; Dong et al., 2006; Cotsovos and Pavlovic, 2008). The theory of lateral inertia confinement, starting from Brace and Jones (1971), portrays a tendency of change of the stress state from a uniaxial stress towards a uniaxial strain condition with the increase of the strain rate. As the concrete compressive strength is known to increase with the lateral confinement, an increase of the dynamic compressive

strength in the presence of a lateral inertia confinement then naturally occurs, even without any rate sensitivity in the constituent material properties.

More recent numerical studies (e.g. Li and Meng, 2003) have provided comprehensive information in support of the above explanation of the dynamic strength enhancement due to lateral inertia confinement. However, the reliability of a quantification of such a contribution in the total observed DIF using a numerical approach will obviously depend upon the soundness of the computational model and the constitutive laws for the materials used in the analysis. In this respect, several modelling factors come into play.

Among other modelling considerations, the heterogeneity of concrete is an obvious but difficult factor in the high strain rate modelling applications. The potential effect of the material heterogeneity can be envisaged from the fact that the response of structural materials under high rate loading involves transient stress waves with drastic time and spatial variations, and the stress wave band can be comparable to the size of the mesoscopic heterogeneity of the concrete material, i.e. the nominal aggregate size. As such, it may be anticipated that the multi-phase character of the concrete composite is a sensible factor influencing the initiation and the propagation path of damage in the composite under high rate loading.

Research on the mesoscale modelling of concrete in the quasi-static literature has been going on for many years, and a number of studies have been reported using the mesoscale model to explore the damage evolution in concrete under static loading (Eckardt et al., 2004; Wriggers and Moftah, 2006). However, these mesoscale studies do not involve the transient dynamic effects, and the analysis is usually carried out using numerical solvers which are suited for relatively simple material description and loading conditions. This make the extension of the models to generalized dynamic and complex stress conditions difficult.

To facilitate a comprehensive mesoscale analysis of concrete-like materials for high dynamic and complex stress applications, a versatile mesoscale modelling framework is being developed. The basic framework encompasses a module for the generation of the mesoscale geometric structure (mesoscale coordinate database),

implemented using Matlab; a procedure for the finite element meshing (including the interfacial transition zone ITZ); and the subsequent dynamic analysis using a general-purpose transient dynamic analysis solver. Two alternative schemes of representing the ITZ between the aggregates and the mortar matrix are possible, one using the classical cohesive interface elements, and another using an equivalent layer of solid elements. The current mesoscale model allows for 2D analysis under any arbitrary loading conditions (Tu and Lu, 2011), and continued development is being undertaken towards incorporating the 3D effect via a pseudo- or a true 3D mesoscale model.

In what follows, an overview of the existing 2D mesoscale modelling framework will be given first. The localisation problem in the strain softening modelling is then discussed and recommendations of a proper parameter setting are provided for compression and tension modelling. The investigation then focuses on the potential discrepancies arising from a 2D mesoscale description of the actual 3D response under high strain rate loading, especially concerning the lateral inertia confinement effect. To rectify such discrepancies, a pseudo-3D model in a sandwich layout is proposed in lieu of a true 3D mesoscale model. The pseudo-3D model is then employed in the analysis of the compressive behaviour of concrete under high strain rate loading, and the results are discussed in the context of the dynamic increase factor (DIF).

3.2 Overview of 2D mesoscale modelling framework

3.2.1 Generation of the mesoscale geometry and FE meshing

In the current mesoscale model, the mesoscale structure of concrete is represented by 2D mesoscale geometry with a stochastic distribution of aggregates embedded in the mortar matrix. The aggregates are represented by random polygon particles, and the nominal size of the individual aggregates obeys a given grading curve. The generation of the mesoscale geometry follows a commonly adopted take-and-place procedure (Wittmann et al., 1984; Wang et al., 1999), satisfying non-overlapping and

minimum gap requirements. The procedure is programmed using Matlab. Fig. 3-1 illustrates two mesoscale geometry samples generated using the above procedure. The density of the aggregates can be controlled by specifying a volumetric ratio.

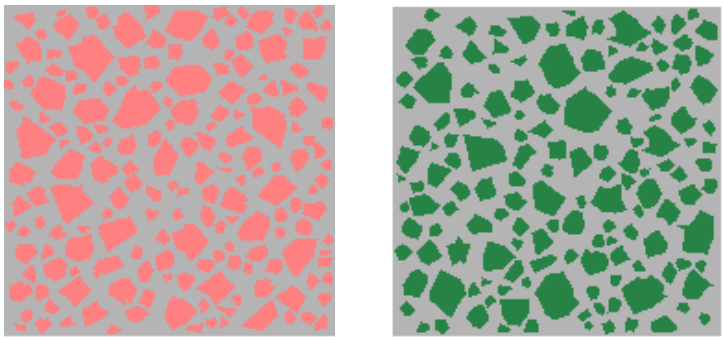

Figure 3-1: Sample mesoscale geometry generated using the take-and-place procedure

After the generation of the mesoscale structure, the geometric data can be fed into a finite element meshing processor. In the present study, ANSYS pre-processor is used, to perform the FE meshing. Fig. 3-2 shows an example of the mesoscale mesh for concrete. The mesh data is then exported to Matlab to finish with the completion of the model input data as required by the chosen FE analysis solver. In the present study, the transient dynamic analysis code LS-DYNA is employed to perform the nonlinear dynamic analysis using an explicit time integration procedure.

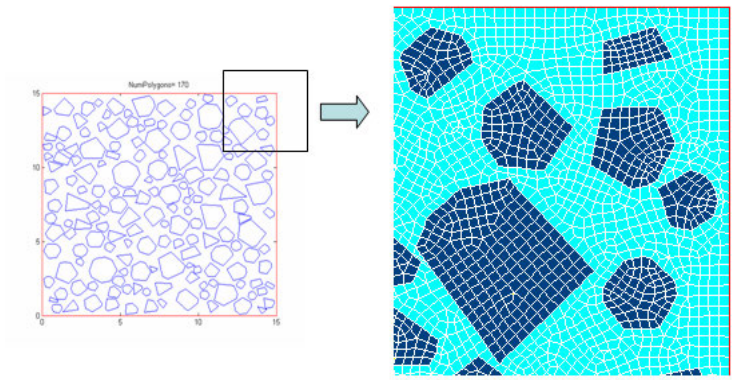

Figure 3-2: FE meshes for aggregate and mortar elements

In the generation of the mesoscale geometry, only the coarse aggregates are considered to form the discrete aggregate phase. For normal concrete, the coarse aggregates include those with a minimum nominal size of 4.75mm (Wriggers and

Moftah, 2006). Smaller aggregates are lumped into the mortar phase. The volumetric ratio (or area ratio in 2D) of the coarse aggregates is typically in a range of 0.4-0.5 for normal concrete, but this may be adjusted where necessary.

The interface transition zone (ITZ) between aggregates and mortar matrix is considered to be an important factor affecting the damage initiation and growth in the concrete material (Garboczi and Bentz, 1997). Therefore, in the present mesoscale model the ITZ is explicitly modelled as a separate (third) phase in the composite. Two alternative methods may be considered for the modelling of the interfacial transition zone (ITZ), one using the classical zero-thickness cohesive interface elements, and the other using an equivalent layer of solid elements. Previous analysis (Tu and Lu 2011) has shown that, comparing to the cohesive element model as available in LS-DYNA, the equivalent ITZ layer method tends to yield a more consistent and stable result. The equivalent ITZ approach is adopted in the present study, as depicted in Fig. 3-3.

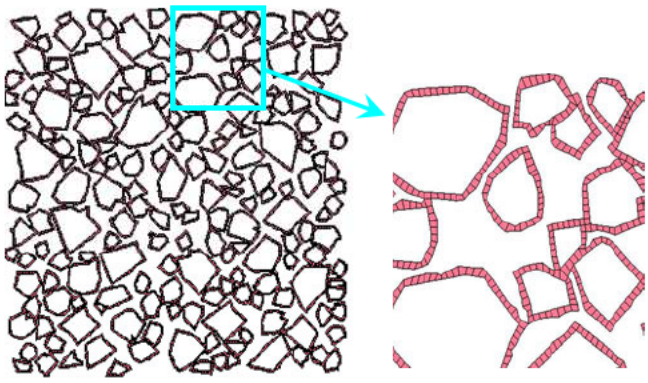

Figure 3-3: Representation of ITZ with a layer of solid elements

Another important aspect to note is that the 2D mesoscale FE model in the present study is configured in a thin plate form with a single layer in the out-of-plane direction. This model setting is partly to accommodate the use of the chosen concrete material model (material #72) in LS-DYNA, which is available only for 3D analysis. Furthermore, with such a single layer model, a plane stress or plane strain condition may be simulated by restraining the out-of-place movement on either one or both faces of the specimen. As a matter of fact, when the strain rate becomes high and the lateral inertia becomes significant, neither the plane stress nor the plane strain condition can realistically describe the lateral inertia effect in the third direction. A

2D axis-symmetric model can replicate a 3D homogenous cylinder sample; however it cannot be extended to the mesoscale description because a 2D axis-symmetrical model implies ring-shaped aggregate components in a cylinder, and this obviously deviates from the real aggregate effect. An illustrative example of using an axis-symmetrical mesoscale model will be given in Section 3.5 to highlight the discrepancy in the computed results.

3.2.2 Model Setting and boundary condition

Different material properties are used for the three individual phases, i.e., aggregates, mortar matrix, and the ITZ. Considering that the aggregates are much stronger than mortar, it may be modelled as a linear elastic material. Trial analysis indicates that this simplification may be acceptable when the strain rate is within a certain limit. For very high strain rate regime (i.e. on the order of $100s^{-1}$ and above), the modelling of aggregates using a linear or non-linear model will tend to influence more sensibly the simulation results. In the present study, the aggregates are modelled as nonlinear with compressive failure strength of 200MPa, which represents typical crushed rock aggregates.

As the primary source of the nonlinear behaviour, the mortar matrix and the equivalent ITZ are modelled using a damage-plasticity model. In the present study, the Concrete Damage Model (Material #72 in LS-DYNA) is employed. This material model is capable of describing the material failure due to tension, shear, as well as compression under various stress conditions (Malvar et al., 1997), and it also incorporates pressure hardening and strain softening. The strain rate enhancement to the material strength may be considered by defining a dynamic increase factor (DIF) if desired. Numerical evaluation (Tu and Lu, 2009) has demonstrated that the model can reliably reproduce the tension and compression behaviour of concrete-like materials under uniaxial as well as multi-axial stress conditions. For the equivalent ITZ elements, considering that the strength of the real ITZ is about half of the mortar strength, and that the equivalent ITZ layer involves partly the mortar material adjacent to the real ITZ, it is deemed reasonable to assign a nominal strength of around 75% of the mortar strength for the equivalent ITZ layer.

Table 3-1 shows a typical set of material parameters for normal concrete of 30-MPa grade.

Table 3-1: A typical selection of material parameters for 30-MPa concrete

Mortar material	
Young's module (E)	20 GPa
Poisson's ratio	0.2
Density	2300 kg/m^3
Compressive strength	35 MPa
Aggregate material	
Young's module (E)	50 GPa
Poisson's ratio	0.2
Density	2600 kg/m^3
Compressive strength	200 MPa

For the simulation of concrete samples under high rate axial loading, a device-dependent model configuration, incorporating the loading apparatus such as the SHPB (Li and Meng, 2003), may be considered. For simplicity, in the present study the intended loading scheme is realised by applying a velocity (and hence displacement) history as a boundary condition to the loading face. Preliminary analysis indicates that a smooth velocity history helps to suppress the unwanted

oscillation in the resulting stress-strain response, hence this loading scheme is adopted in the analyses. The loading rate can be controlled by varying the velocity rise time and the maximum velocity value, as schematically illustrated in Fig. 3-4.

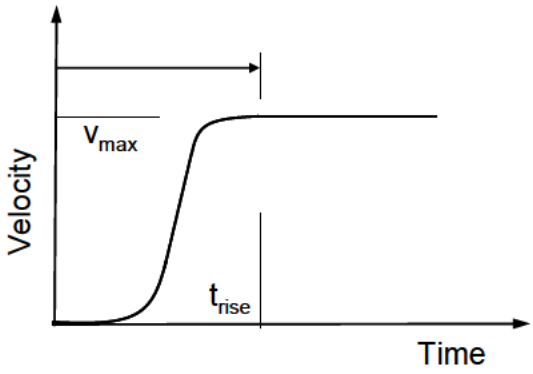

Figure 3-4: Schematic of the velocity history for applying external axial load

3.2.3 Concrete Material model

The soundness of the concrete material constitutive model is essential in a numerical analysis of the behaviour of concrete under a passive confinement by reinforcement cages. Important considerations include the pressure dependency and the lode angle dependency of the strength surfaces, and rate dependency for dynamic analysis, among others. In the transient dynamic analysis realm, Tu and Lu (2009) reviewed a range of possible concrete material models, including several sophisticated models with comprehensive capabilities.

One of such comprehensive concrete material models is the so-called Concrete Damage Model (or K&C model) developed by Malvar et al. (1997). This material model evolved from the early version used in DYNA3D finite element program. The latest version of the model (release III) is available in LS-DYNA as material #72R3. The model uncouples the total stress into an isotropic and a deviatoric part. The isotropic behaviour is controlled by a compaction curve relating the current pressure to the current and previous compressive volumetric strain, and the deviatoric stress is defined as a linear combination of failure surfaces based on a three-invariant formulation. Fig. 3-5 depicts the compaction curve, and the three strength surfaces, namely an initial yield surface, a maximum failure surface and a residual surface. The general strength criterion is given by a uniform expression as:

$$\Delta\sigma = \sqrt{3J_2} = f(p, J_2, J_3) \tag{3.1}$$

where $\Delta\sigma$ and p denote the principal stress difference and pressure, respectively. I_1, J_2 and J_3 are the stress invariants. In principal stress space, the compressive meridian is governed by $f(p, J_2, J_3) = \Delta\sigma^c \times r'$, where $\Delta\sigma^c$ represents the compressive meridian and r' is a function of the Lode angle. The compressive meridians of the three strength surfaces are defined as:

$$\Delta\sigma_m = a_0 + \frac{p}{a_1 + a_2 p} \quad \text{(Maximum failure surface)} \tag{3.2}$$

$$\Delta\sigma_y = a_{0y} + \frac{p}{a_{1y} + a_{2y} p} \quad \text{(Yield failure surface)} \tag{3.3}$$

$$\Delta\sigma_r = \frac{p}{a_{1f} + a_{2f} p} \quad \text{(Residual failure surface)} \tag{3.4}$$

where a_0, a_1 and a_2 are free parameters determined by experimental data. For the failure surface, $a_0 = 0$.

The current failure surface is linearly interpolated from maximum failure surface and either yield or residual failure surface:

$$\Delta\sigma = \eta(\Delta\sigma_m - \Delta\sigma_{\min}) + \Delta\sigma_{\min} \tag{3.5}$$

Here, η is a function of λ, the effective plastic strain, which is defined according to formula 3.6 and 3.7. This function is somehow called “damage function”.

$$\lambda = \int_0^{\bar{\varepsilon}^p} \frac{d\bar{\varepsilon}^p}{r_f (1 + p / r_f f_t)^{b_1}} \qquad (p >= 0) \tag{3.6}$$

$$\lambda = \int_0^{\bar{\varepsilon}^p} \frac{d\bar{\varepsilon}^p}{r_f (1 + p / r_f f_t)^{b_2}} \qquad (p < 0) \tag{3.7}$$

where $d\bar{\varepsilon}^p = \sqrt{2/3 d\varepsilon_{ij}^p d\varepsilon_{ij}^p}$ is the effective plastic strain increment, f_t is quasi-static tensile strength, r_f is rate enhancement factor, b_1 and b_2 are parameters to control the slope of damaging accumulation.

The output damage is a scaled factor is defined to measure the damage:

$$DF = \frac{2\lambda}{\lambda + \lambda_m} \tag{3.8}$$

When η =1(current failure surface = maximum failure surface), $\lambda = \lambda_m$, we have,

$$DF = \frac{2\lambda}{\lambda + \lambda_m} = 1 \tag{3.9}$$

and when $\lambda \to +\infty$, i.e. concrete is completely damaged,

$$DF = \frac{2\lambda}{\lambda + \lambda_m} = 2 \tag{3.10}$$

In the case of DF<1, there is no damage in the concrete; while 1<DF<2, damage starts to accumulate and concrete is deemed to be completely damaged when DF=2. In the following chapters of this thesis, this damaging factor will be used extensively to illustrate the damage pattern.

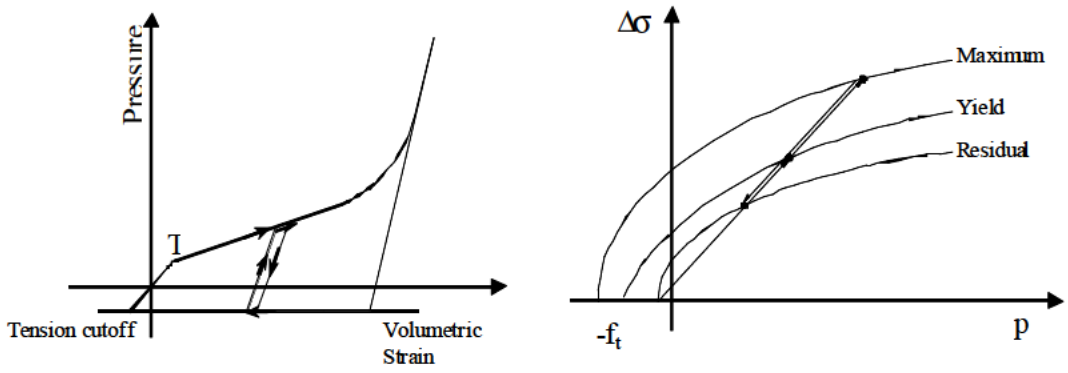

Figure 3-5: Compaction curve (left) and three strength surfaces (right) of the Concrete Damage Model

In order to verify the pressure dependency of the above concrete material model in reproducing the anticipated increase of the strength and ductility under a triaxial compression condition, the single element approach is used, in which a single finite element is subjected to axial compression with different levels of actively imposed lateral confining stresses. Fig. 3-6 shows the achieved axial compressive stress-strain curves for 30-MPa concrete under four different levels of the confining stresses, namely 1, 2, 5 and 10MPa, respectively. It can be observed that the achieved compressive strength and the ductility increase with the increase of the lateral confining stress. The trend is consistent with general experimental observations. More detailed comparison with experimental data will be provided later in the simulation of the passive confinement by transverse reinforcement.

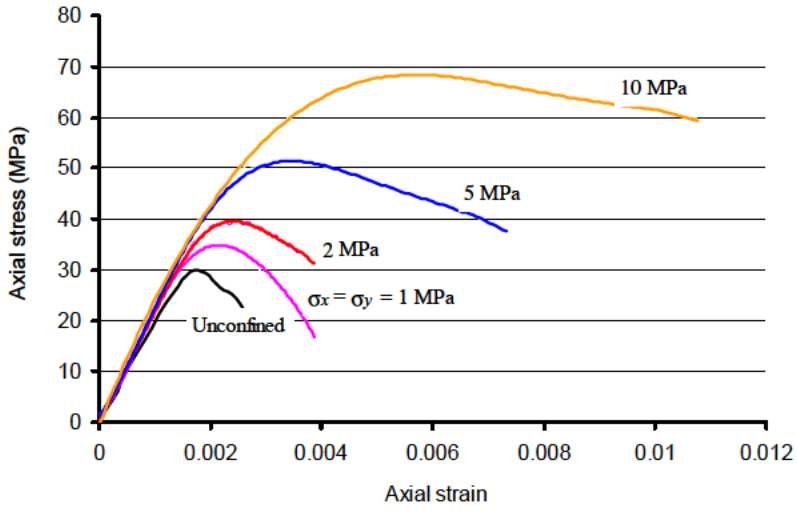

Figure 3-6: Single-element analysis of the axial compressive stress-strain relationship under different levels of active confining stresses

3.2.4 Further investigation of simulation of confinement effect in concrete

A further validation of the capability for K&C model to capture the confinement effect in a realistic concrete structure is also performed. A high fidelity simulation using LS-DYNA (v971) in conjunction with the concrete model is conducted to investigate the passive confining effects of transverse reinforcement by stirrups in representative axially loaded reinforced concrete columns. The model is shown to be

capable of reproducing the behaviour of the confined concrete realistically, paving a way for systematic parametric studies and investigation into complicated confinement, load combination, and dynamic loading situations. However herein we shall focus only on observing the performance of the concrete material model in capturing the confinement effect.

Rectangular (including square) and circular sections are two typical section shapes used in structural design for axially loaded members (columns). In this study, one square section and one circular section are selected for the modelling of confined concrete in a short column setting. Fig. 3-7 shows the schematic of the cross-sections and the reinforcement arrangements. To enable a direct comparison of the numerical results with available experimental data, the section of the square specimen is chosen to be 200 $\times$ 200 mm, and the length is 600 mm. The diameter of the circular specimen is also 200 mm, with the same length as the square specimens. The concrete cover is set to be 15 mm in all specimens. The spacing between the stirrups is initially set to 80 mm. Considering the symmetry of the specimens, only one-eighth of each short-column specimen needs to be modelled.

For simplicity, the steel bars are modelled to have a square section with approximately the same section area as the actual round bars, and the interface between the rebar surface and the concrete is assumed to be perfectly bonded. These simplifications are deemed to be reasonable for the current problem concerning the confinement effect on the concrete, which is mainly derived from the pressure for which the steel-rebar interface behaviour is expected to play a minimal role. For a comparison purpose, the same volumetric ratio is maintained in the square and the circular column specimens. The steel bar is modelled as elasto-plasticity material. The longitudinal steel rebar has yield strength 460 MPa, and the transverse reinforcement has yield strength 250 MPa. They both have a Young's modulus 210GPa.

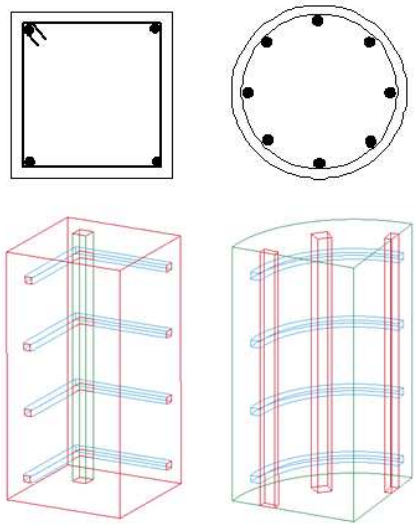

Figure 3-7: Schematic of cross-section and reinforcement arrangements in the numerical simulation of short RC columns

In processing the simulation results the concrete core is taken as the region inside the hoops (exclusive of the hoop space) and the remaining concrete is considered as cover. Fig. 3-8 shows the axial stress-strain curves in the two RC column models. The thick lines are the axial stress-strain curves for the concrete within the confined core, thus may be regarded as representing the confinement effect in the two cases. The remaining curves include the total stress-strain curves (including the contribution of the longitudinal reinforcement), the average stresses within the overall concrete area (including concrete core and cover), and the stresses within the concrete cover, respectively.

As can be observed from the graphs, the total stress and the stress in the confined concrete core reach the peak stress (strength) almost at the same time as the transverse reinforcement reaches its yield strength. This may be explained by the fact that, up to this stage the confining stress increases continuously, while the accumulation of damage, which evolves independently from the confinement as the strain increases, remains to be relatively small. Beyond the first peak stress, the stress-strain curves in the confined concrete core show an apparently increased ductility (or reduced softening rate) in all the specimens, whereas the stress in the concrete cover drops abruptly.

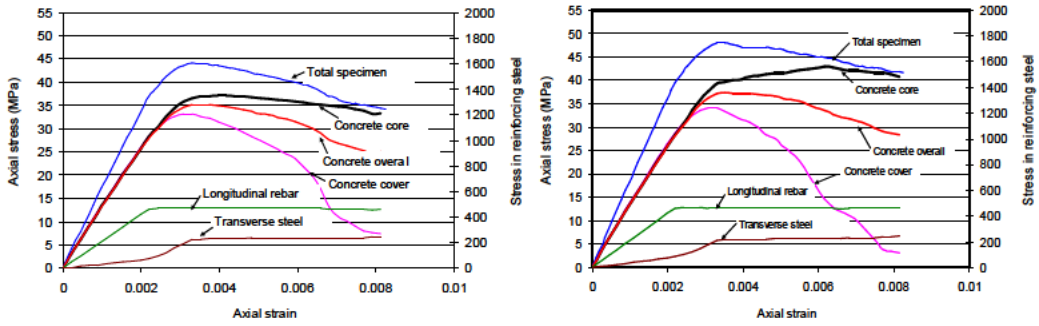

a) Square column **b) Circular column**

Figure 3-8: Axial stress-strain curves for three specimens

In essence, the confining effect on concrete is realised through the pressure arising from whatever confining mechanism that is put in place. In the case of passive confinement by the transverse reinforcement, the effectiveness of the confinement can be more clearly understood by looking at how the lateral confining pressure evolves during the course of the response to the axial loading. In order for a quantitative evaluation, the lateral pressure is calculated as the average lateral stress in all elements within the confined area, i.e.,

$$\sigma_{conf} = \frac{\sigma_x + \sigma_y}{2} \tag{3.11}$$

Fig. 3-9 shows the relationship between the average lateral confining stress and the axial (z-direction) strain for all the three specimens.

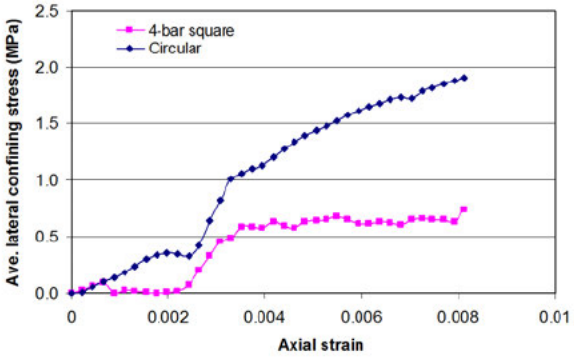

Figure 3-9: Development of (passive) confining stress with increase of axial deformation

The overall confining stress appears to continue increasing when the axial strain reaches 0.003 (peak stress from Fig. 3-8) especially in the circular column. The continued increase, which may be attributed to the hardening of the transverse reinforcement and re-distribution of the stresses within the confined area, eventually leads to an increase in the pressure for elements in the confined area.

The numerical results show that the development of the confining stresses in case of passive confinement can be well captured by the numerical model. In addition, the numerical model has been constructed using a general purpose transient dynamic analysis code (LS-DYNA), and therefore it allows for a straightforward extension to low and high dynamic loading conditions, as well as analysis for complex loading combinations such as eccentric axial loading and bending. The potential influence of the material heterogeneity may be explored using a similar finite element framework but with a mesoscale setting.

3.3 Modelling of softening behaviour and mesh-objective treatment

3.3.1 Mesh dependency in Smeared Crack Band model

The continuum method to model fracture (generally softening) assumes that material fracture can be represented by macroscopic crack. The idea was first proposed by Dugdale (1960), and later developed by Hillerborg et al. (1976) as the Fictitious Crack model. In FCM model, the crack zone is concentrated in a fictitious zone, which could be reduced to zero-thickness. The initiation and growth of crack zone follow a fracture mechanics principle, i.e. a strain energy criterion.

Bazant (1983) developed a smeared crack band model in which a finite width of crack band is assumed in cracking. The crack "localises" in this band, whose width is usually associated with a characteristic length l_c. For numerical modelling of concrete, this width is generally taken as three times of the maximum aggregate size (Bazant, 1983). In his model, the material softening behaviour was characterized by three parameters: the Mode I (opening crack mode) fracture energy G_f^{I}, the tensile

strength f_t, and the width of the smeared crack band l_c. In the case where the element size h_c is larger than l_c, the strain softening modulus is a function of these parameters:

$$E_t = \left(\frac{1}{E} - 2\frac{G_f^I}{f_t l_c}\right)^{-1} \tag{3.12}$$

When the element size is smaller than l_c, the crack strain concentrates on one element. To compensate the fracture energy which is presumably dissipated over a greater width, it requires that:

$$G^I{}_f = h_c \int_{\sigma=ft} \sigma d\varepsilon \tag{3.13}$$

The integral in the formula indicates that on the "localized" element, the softening branch of the stress and strain curve should be adjusted as the crack band width is uniformly distributed within one element.

3.3.2 Parameter set-up in K&C concrete model

The characteristic width l_c is specified by a localization width in K&C model Release III. In the default setting within Ls-DYNA, the value of the localization width is 1 inch (25.4mm), presuming a nominal aggregate size of 1/3 inch as is often used in protective structures. However, this setting is only adequate for modelling large scale concrete structure with element size being greater than this default value. For an analysis where tension failure may prevail while the element size is smaller than the default value, the actual localisation in the numerical model will be restricted to one element width, and as such the localization width in the material model should be set equal to the element width so as to be consistent. In such a case the l_c in the model then has no real physical meaning but merely for the purpose to ensure the preservation of the fracture energy while the tension failure localises within a single element row, and hence facilitates relative mesh convergence.

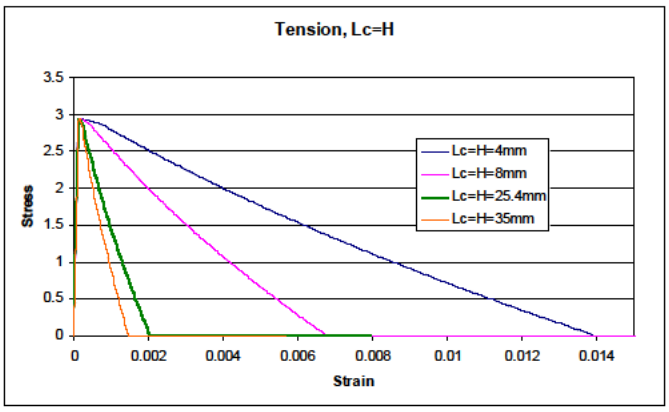

Figure 3-10: Influence of L_c by one element test under uniaxial tension

Fig. 3-10 shows the trend of the softening branch in the stress-strain curve as l_c varies in a single element tension test. It can be observed that as l_c reduces the area underneath the softening branch increases, effectively making Eq. 3.13 constant, and hence ensuring the "fracture" energy absorbed by a single element row to converge to the specified fracture energy, regardless the variation of the mesh size.

It should be noted that the current K&C model moderate the compressive and tensile softening behaviour at the same time. This is potentially problematic if a specimen under compression does not tend to develop softening localisation in a similar fashion as in tension. A rigorous resolution of this potential problem at the material model level is beyond the scope of the present study. Instead an empirical approach is exercised by examining the resulting response and damage patterns to ensure a consistent outcome is achieved. It has been found through representative case studies that for the mesoscale analysis under compression, setting the localisation width to 2~2.5 times of the element size is generally appropriate. In the subsequent numerical simulation studies hereinafter, if it is not mentioned specifically, the localisation width l_c is set equal to two times of the element size for all compression analysis, while it is set to be equal to the element size in the tension analysis.

3.4 Validation Studies on the 2D mesoscale model

The mesoscale model is validated with representative quasi-static and dynamic compression tests.

Fig. 3-11 shows an overall view of a 2D mesoscale model setting for a uniaxial compression. The volumetric ratio of coarse aggregates is assumed to be 0.45. The target concrete is 30 MPa class (compressive strength 30 MPa). As mentioned in Section 3.2.2, for this class of concrete, the strength of mortar is assumed to be 35 MPa, and the strength of the ITZ is approximately 27 MPa.

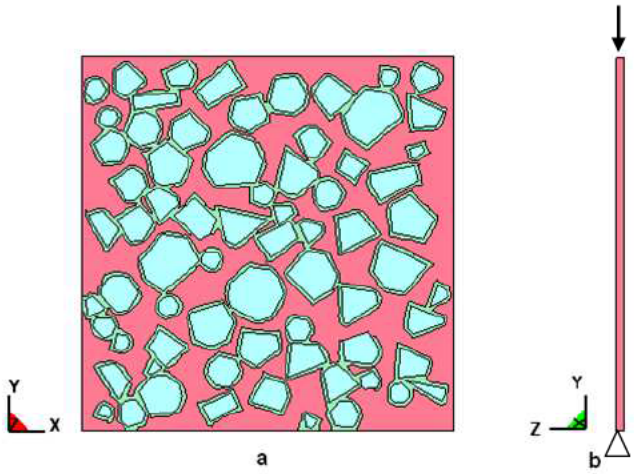

Figure 3-11: Example of 2D mesoscale model in a thin plate configuration with the out-of-plane movement being restrained on one side ("plane stress") or both sides ("plane strain")

3.4.1 Normal concrete under quasi-static compression

A standard normal concrete cube under compression is simulated. The specimen has a side length of 150 mm, and the size of coarse aggregates is in a range of 4.75-25mm. The nominal mesh size is 1mm. In the plate-like FE model, the thickness has one single layer and the thickness is assigned to be 1mm to be consistent with the element size within the main plane. Load is applied by a slow velocity boundary on the top side of the model, while the bottom side is constrained in the longitudinal direction as shown in Fig. 3-11.

Two loading and support face friction conditions are simulated; one is friction free (lower bound scenario), and another with a complete lateral constraint on the top and bottom faces (upper bound scenario). A typical laboratory test with a standard steel loading piston should fall in-between the above two extreme situations.

Fig. 3-12 (a) and (b) shows the simulation results. As can be seen, the crack patterns resemble well the general experimental observations, i.e., inclined cracks occur under low friction loading, whereas a double-cone failure mode appears when a high frictional constraint is involved. The simulated nominal (or engineering) compressive stress-strain curves also agree favourably with typical experimental observations depicted in Fig. 3-12 (c). It is noted that the nominal (engineering) stress is evaluated here by dividing the total (nodal) force on the loading face by the cross-section area, while the nominal strain is defined as the total axial displacement divided by the initial length of the specimen.

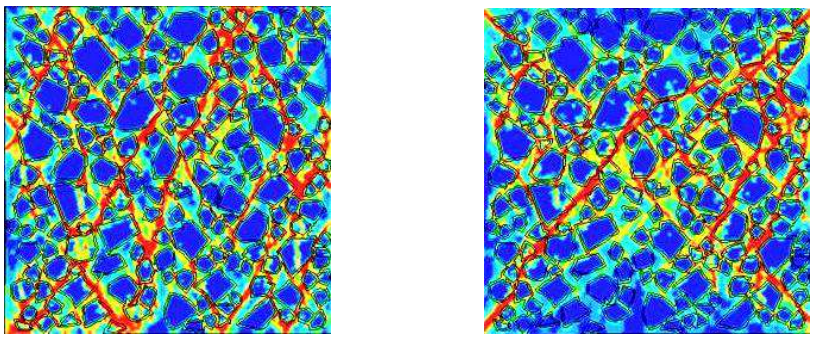

(a) Two representative failure modes (left = no friction; right = upper bound friction)

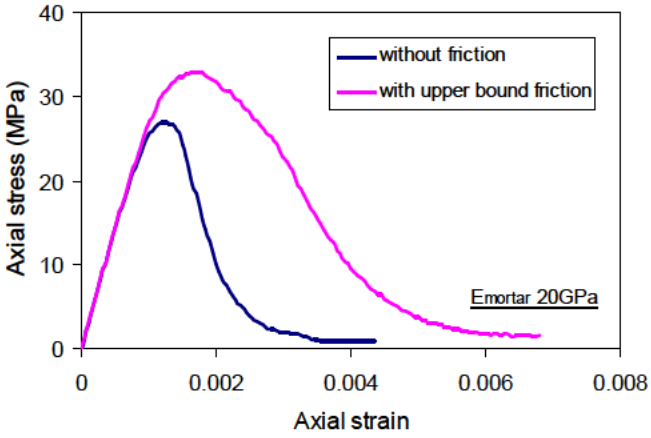

(b) Simulated nominal stress-strain curves

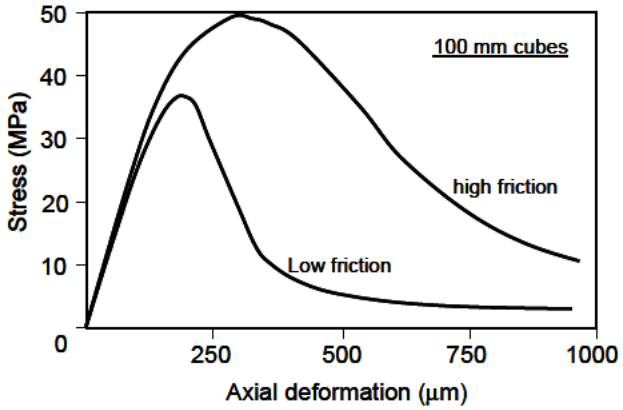

(c) Typical experimental results (adapted from van Vliet, 1996)

Figure 3-12: Mesoscale simulation results under quasi-static compression and comparison with typical experimental observations

3.4.2 Example results under high-rate compression

For high strain rate compression, the size of the concrete sample is chosen to be 50 mm, as commonly used in the SHPB tests of concrete material (cube or cylinder). Accordingly, the coarse aggregate size is reduced to a range of 2~8 mm. To reduce additional uncertainties, the loading and support faces are assumed to be friction free. This assumption is deemed to be reasonable considering the fact that the friction would be of a less significant factor under high strain rate loading, owning to the already limited expansion due to lateral inertia confinement.

Fig. 3-13 shows the development of damage under two different loading rates, namely $10s^{-1}$ and $100s^{-1}$. Note that for all high rate loading simulations (Fig. 3-13 onwards) the load is applied horizontally from the left side of the specimens. The damage patterns exhibit a clear characteristic pertaining to the geometric feature of the aggregates. Comparing to the static loading shown in Fig. 3-11, no concentrated major crack lines occur. Furthermore, the comparison between the two different strain rate scenarios indicate that, under a relatively low strain rate loading (the $10s^{-1}$ case herein) an fairly uniform distribution of damage is achieved, whereas under a high strain rate ($100s^{-1}$ herein) failure tends to develop from the loading side towards the support end in a progressive manner. This observation confirms that an upper strain rate limit exists for a given size of specimens, as is considered in the classical SHPB theory (Tedesco and Ross, 1998), if a relatively uniform stress field is to be achieved before failure.

For a general comparison, Fig. 3-14 illustrates the simulated progress of damage when a homogenized model is employed for a strain rate of $100s^{-1}$. It becomes immediately clear that under such a high strain rate condition, modelling of concrete using a homogenized model cannot represent realistically the underlying damage evolution. Consequently, the entire simulation outcome can be questionable.

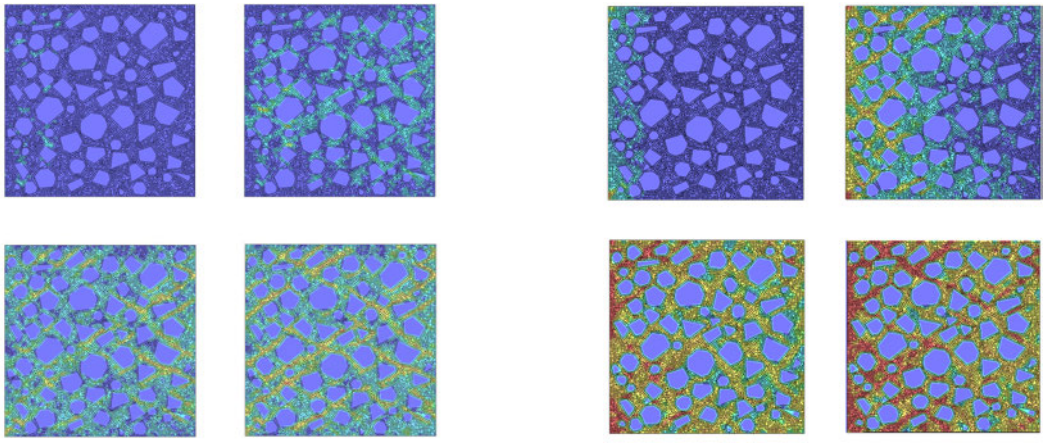

(a) Rate=10.0 s^{-1} **(b) Rate=100.0s^{-1}**

Figure 3-13: Examples of damage development under dynamic compression (load is applied horizontally from the left side; the same is true for all other figures hereinafter. Damage Stages: upper left-start of loading, upper right-half of peak strength, lower left-peak strength, lower right-failure)

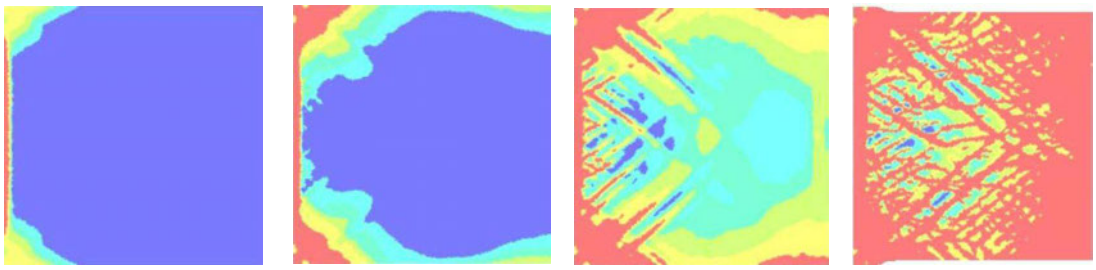

Figure 3-14: Simulated damage pattern using a homogeneous model, strain rate = 100s^{-1}

3.5 Investigation of discrepancies in a 2D model under high rate loading

As mentioned in Introduction, the lateral inertia confinement is deemed to be a significant factor influencing the dynamic behaviour of concrete, especially under compression. As such, certain discrepancies are inevitable in a 2D model as compared to the actual 3D behaviour of a concrete specimen under high strain rate loading. It can be anticipated that a 2D plane stress model will underestimate the lateral inertia confinement, whereas a 2D plane strain model will tend to overestimate the inertia confinement. In this section we shall use the 2D plane stress representation to illustrate the potential issues.

3.5.1 General comparison of 2D and 3D model responses

For a general comparison, a set of 2D and 3D homogeneous FE models are analysed first. The 2D model is similar to that described in Section 3.4, except that a homogeneous material is considered. The 3D models include both a cylinder and a cube.

Fig. 3-15 shows a comparison of the development of damage within the 2D and 3D homogeneous models under a loading rate about 50s^{-1}. To expose the damage in the 3D model, a section passing through the longitudinal centerline is taken. The four pictures for each model cover the initiation of inelastic response to post-peak softening stages of the analysis.

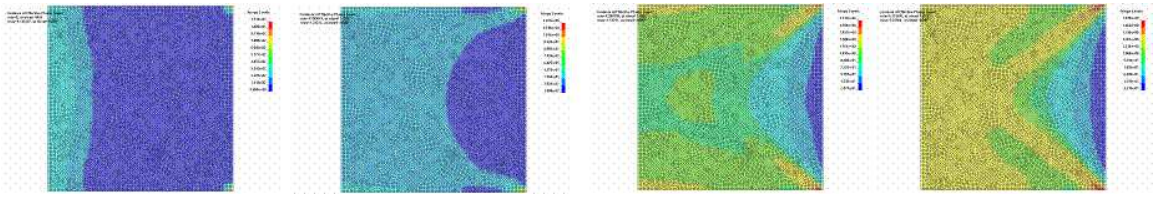

(a) 2D plane stress

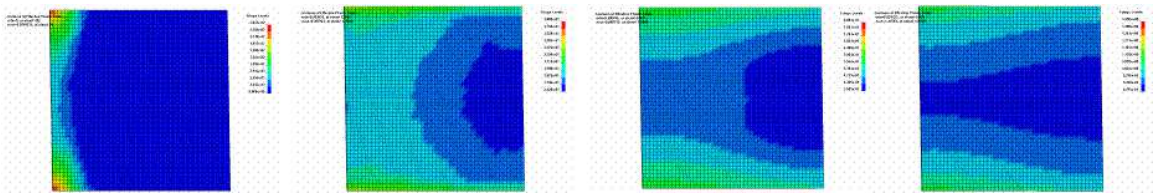

(b) 3D cubic

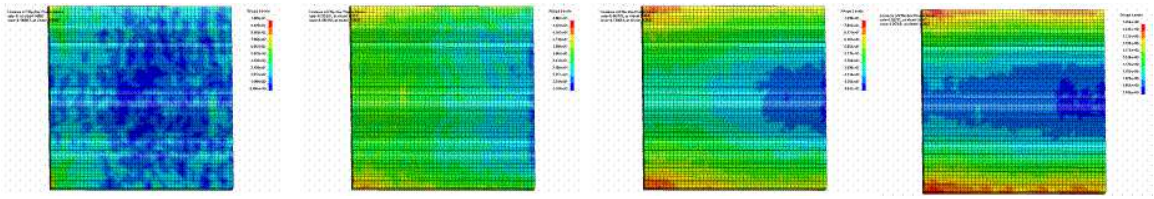

(c) 3D cylinder

Figure 3-15: Comparison of damage patterns in 2D vs 3D homogenous models, strain rate 50s^{-1}

As can be observed, the general development of damage shows a similar path among different models. However, the 2D model develops an apparent diagonal failure pattern extending from the corners at the supporting face. Moreover, the confinement effect in the central area of the 2D model is apparently less well developed as compared to the 3D cube and the 3D cylinder models. As a result, the maximum average strength achieved in the 2D plane stress model is noticeably less than the 3D models (not shown here), and this difference tends to increase as the loading rate increases.

Similar analysis is performed on the 2D mesoscale model. The damage patterns are shown in Fig. 3-16. It can be seen that the diagonal damage becomes less noticeable, due apparently to the presence of the aggregates, but the overall damage distribution is similar to that in the 2D homogeneous model and there is not a clearly developed confined zone in the central area of the specimen.

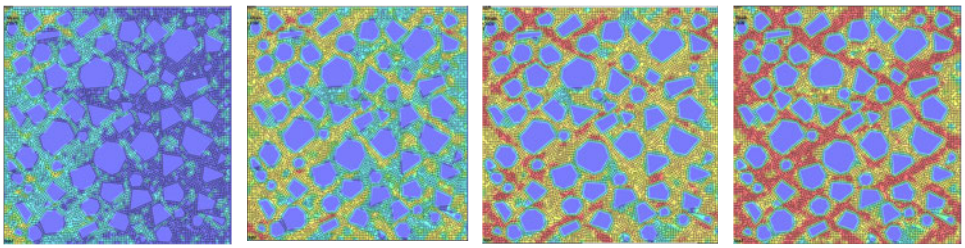

Figure 3-16: Damage development in 2D mesoscale model, strain rate 50 s^{-1}

3.5.2 Thickness effect in 2D plane-stress model

To further examine whether the 2D model (for plane stress) is sensitive to the choice of the thickness, the 2D mesoscale model and the 2D homogeneous model are analyzed with different thickness varying in a range of 0.2-2.5 mm (i.e., 0.4~5 times of the nominal element size within the plane). Fig. 3-17 shows the variation of the nominal strength with the thickness for both the 2D mesoscale and the homogeneous models.

As expected, the stress response of the 2D homogeneous model is not sensitive to the variation of the thickness, confirming that the achieved stress condition in the 2D homogeneous model using a thin plate configuration resembles well a plane stress condition. This also indicates that the small amount of the lateral inertia activated by the single-layer elements in the thickness direction is negligible.

On the contrary, the strength of the 2D mesoscale model exhibits a noticeable sensitivity to the thickness, and no convergence trend is observed as the thickness decreases. Since the lateral inertia in the thickness direction is similar to that in the 2D homogeneous model, and this effect has been shown to introduce little effect on the stress response, the variation of strength in the 2D mesoscale model can only be attributed to the interaction between the aggregates and the mortar elements in the thickness direction.

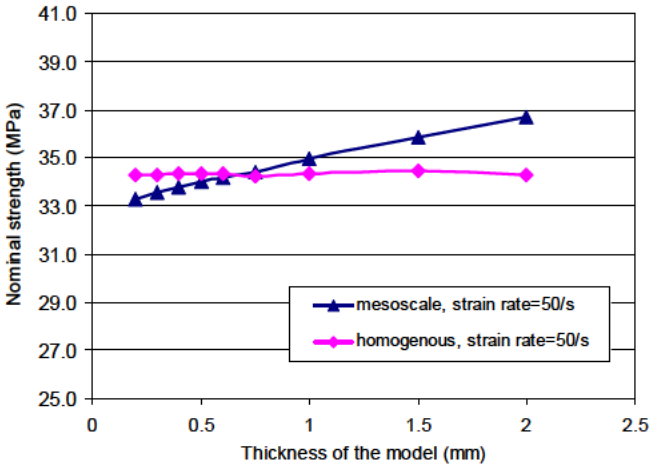

Figure 3-17: Sensitivity of the simulated strength in a 2D model to the thickness

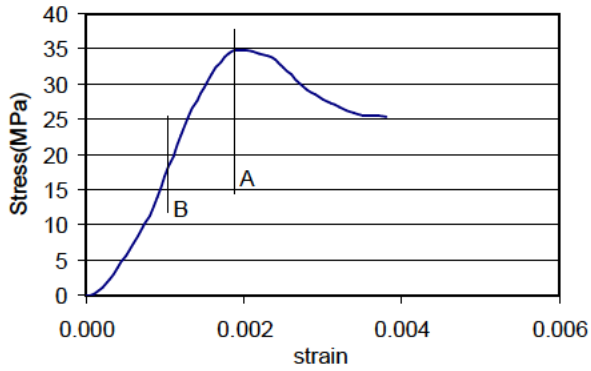

(a) Nominal axial stress - strain curve

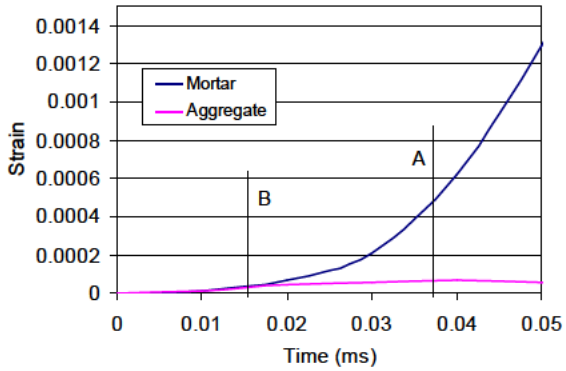

(b) Strain in the thickness direction

Figure 3-18: Influence of aggregate confinement on mortar and the overall strength in plane stress mesoscale model

Fig. 3-18 depicts the nominal stress-strain curve in the 2D mesoscale model with a thickness of 1mm, and the average strain developed in the aggregate and mortar elements along the thickness direction.

It can be clearly observed that the aggregate and mortar elements develop a considerable difference in the strain along the thickness direction when the specimen responds into the inelastic regime. This effectively results in an unexpected confinement from the stronger aggregates on the weaker mortar elements in the out-of-plane direction. Such a phenomenon would only introduce complication in a 2D mesoscale model analysis using a thin plate configuration, thus increasing the uncertainty in the simulation results.

3.5.3 Brief discussion on the issues with an axis-symmetric model

From a global perspective a concrete cylinder under axial loading may be treated as an axis-symmetric problem, and thus may be modelled using a 2D axis-symmetric model. However, this treatment cannot be extended to the case of mesoscale modelling, since with an axis-symmetric model, the aggregates effectively become continuous circular hoops, which obviously do not represent the true effect of the discrete aggregates.

To highlight the discrepancy a 2D axis-symmetric model may result, Fig. 3-19 illustrates a typical damage pattern simulated under an axis-symmetric mesoscale configuration. The false “hoop effect” from the aggregates is clearly visible, and this gives rise to an unrealistic radial confining stress on the weaker mortar material, even under a quasi-static condition.

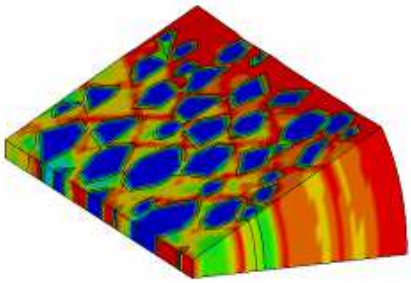

Figure 3-19: Illustration of the false hoop effect in an axis-symmetric mesoscale model

3.6 Development of a pseudo-3D mesoscale model

To resolve the above mentioned issues with a 2D mesoscale model in the absence of a true 3D mesoscale model, a pseudo 3D mesoscale model is proposed herein. The key purpose of such a pseudo 3D model is to facilitate the development of a realistic lateral inertia confinement as in a real 3D environment, while allow the full mesoscale features to evolve within the primary 2D plane.

A sandwich layout can be well suited to achieve the above objectives. Such a configuration is composed of a layer of the plane mesoscale model and a body of the homogeneous concrete material, thus forming a complete 3D specimen shape. The mesoscale layer is sandwiched in the homogeneous concrete, and a sliding interface is enabled between the mesoscale layer and the homogeneous part of the model. In this way, the mesoscale layer will deform independently within its own plane, as in the case of a 2D mesoscale model, while in the direction normal to the plane it will be subjected to the confining stress from the homogeneous body of concrete. Provided the properties of the homogeneous portion of the model resemble the bulk properties of concrete, the lateral inertia effect on the sandwiched mesoscale layer in the normal direction should be similar to that in a true 3D mesoscale model. Consequently, the behaviour of the mesoscale portion within its plane should resemble well what happens in a true 3D mesoscale model. The effectiveness of such a pseudo-3D model configuration will be illustrated in the following sections.

Depending on whether a cylinder or a cube sample is to be modelled and considering the symmetry, one may choose a half-cylinder or half-cube model, with the mesoscale layer being attached to the symmetrical face of the model.

3.6.1 Cubic sandwich model

For a cubic test specimen, a pseudo 3D mesoscale model can be set up by sandwich the mesoscale model (plate) into the middle of a homogeneous cube, as shown in Fig. 3-20(a). Considering the symmetry, only half of the cube is required in the analysis. For a 50mm cubic specimen, the halved model will consist of a 50 x 50 x 24 mm

homogeneous portion, and a 50 x 50 x 1 mm mesoscale portion. The symmetrical condition is imposed on the outer face of the mesoscale portion.

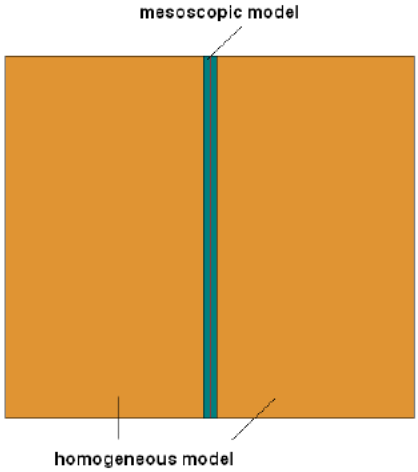

(a) Geometry of the sandwich model

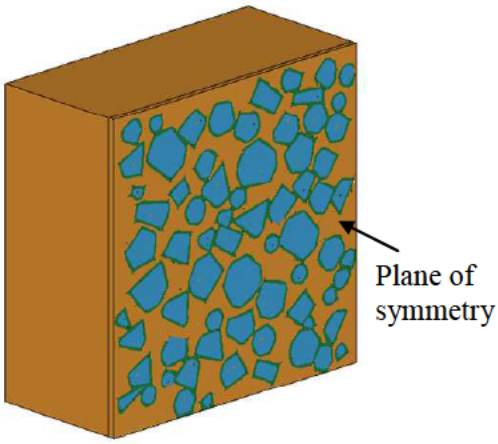

(b) Halved model with symmetry

Figure 3-20: Configuration of a pseudo-3D mesoscale model for a cubic specimen

Fig. 3-21 shows the development of damage in the mesoscale portion of the above sandwich model as well as in the whole specimen. The following general observations may be made, 1) the overall contour shows a clear resemblance of the 3D effect, 2) the mesoscale portion exhibits a damage pattern that agrees favourably with that from the 3D homogeneous model, with the inner area showing much reduced damage due to the confining effect, and 3) the damage within the mesoscale

portion retains the essential mesoscale features. These observations indicate that the sandwich configuration is capable of reproducing the mesoscale effect in a realistic 3D stress condition.

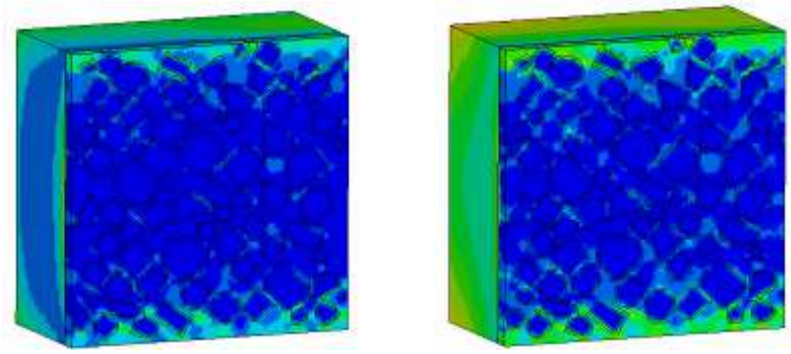

Figure 3-21: Damage patterns in a pseudo 3D (sandwich) mesoscale model for cube specimen

More detailed description of the pseudo 3D mesoscale modelling results will be given in association with a cylindrical sandwich model in the section that follows.

3.6.2 Cylindrical sandwich model

For the modelling of a cylinder specimen using the concept of the pseudo 3D mesoscale model, a cylinder shaped sandwich configuration is appropriate. With the consideration of symmetry, a half cylinder model with a layer of mesoscale model attached to the cut face will suffice, as shown in Fig. 3-22. To save the computational cost, without affecting the accuracy, the mesh size in the homogeneous portion may be increased to a certain extent. For the mesh shown in Fig. 16, the total number of elements is around 40,000 which is just about four times of the number in the 2D mesoscopic model.

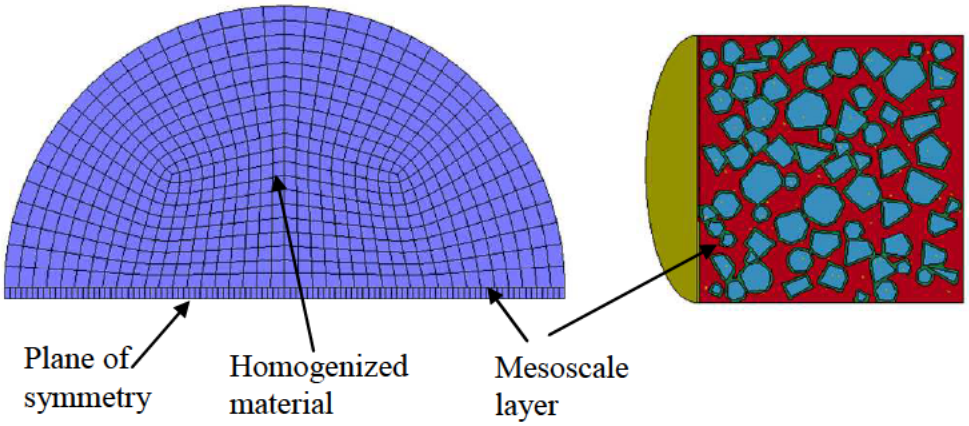

Figure 3-22: Sandwich model (cylinder)

The effectiveness of the above sandwich model for cylinder specimens is verified by first comparing the general development of damage from such a model with the 3D homogenous modelling results, and then an evaluation of the sensitivity of the nominal strength in the mesoscale portion to the thickness of the mesoscale layer. Fig. 3-23 shows a comparison of the damage from the sandwich mesoscale model and the 3D homogeneous model.

It can be observed that the overall damage patterns agree well between the two models. Damage is initiated from the loading side and propagates towards the support end. The central zone of the specimen exhibits considerably less damage than the outer region, indicating a significant confining effect. Besides, damage in the mesoscale model shows a clear effect of the aggregates, with the damage in the ITZ region occurring first on the loading side and then developing around the aggregates.

Regarding the influence of the mesoscale layer thickness on the simulated strength in the mesoscale portion of the model, three different thicknesses were analyzed, namely 0.5, 1.0 and 2.0 mm. Results indicate the variation of the strength is well within 2% for the thickness varying in the above range. Recall that in the 2D mesoscale model, the variation of the strength between models of 0.5mm thick and 2mm thick was about 10%. This indicates that the complication involving the thickness of the mesoscale layer is virtually eliminated in the pseudo 3D mesoscale model.

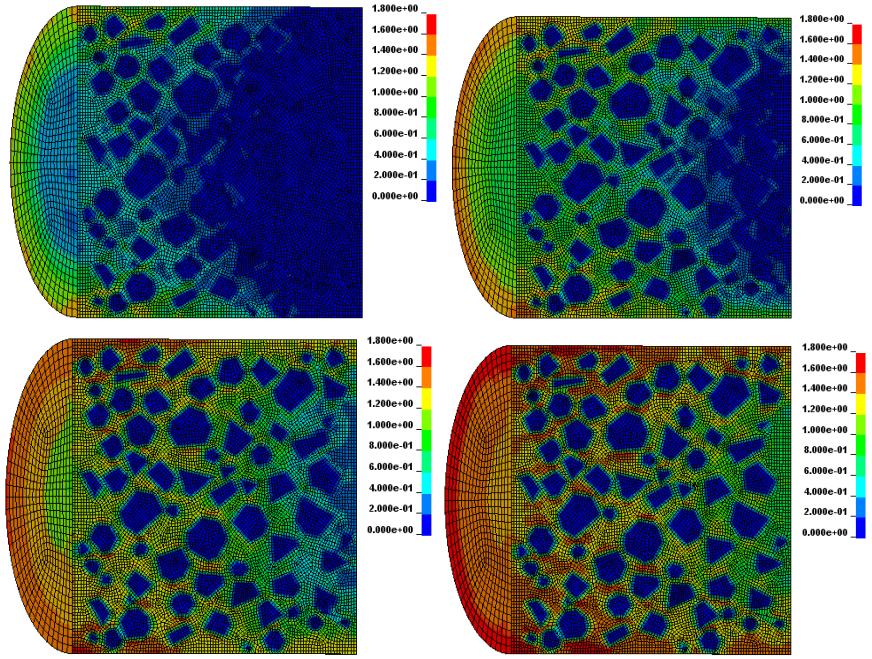

(a) Pseudo 3D mesoscale model

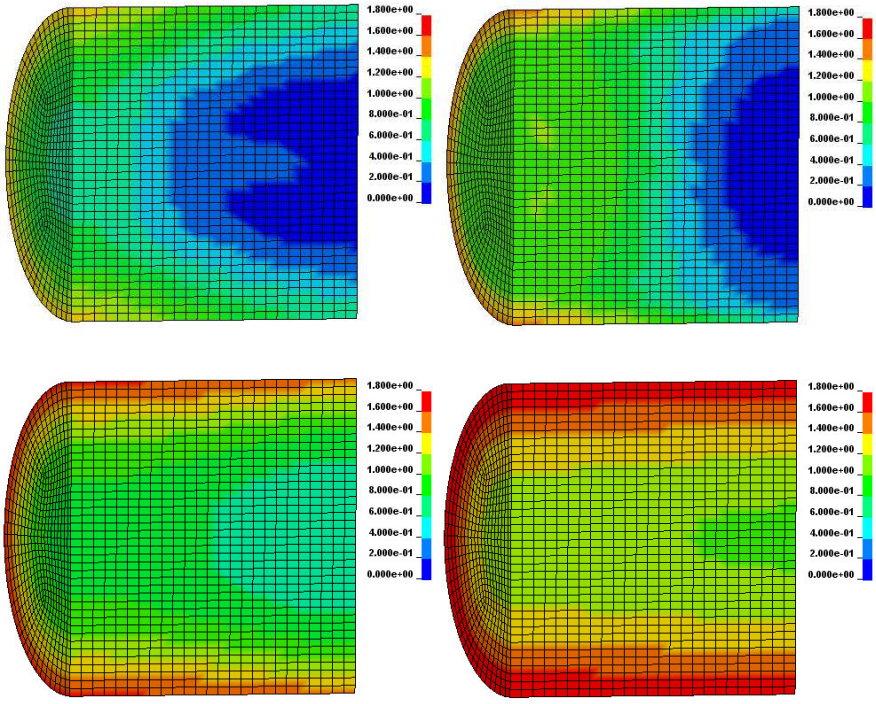

(b) 3D homogeneous model

Figure 3-23: comparison of damage patterns in the pseudo 3D mesoscale model and 3D homogeneous model, strain rate 50 s^{-1}

3.7 Comparison of simulated DIF using different modelling schemes

With the availability of the pseudo 3D mesoscale for an improved simulation of the lateral inertia confining effect, a series of calculations were carried out to examine the variation of the apparent compressive strength of concrete with the increase of the strain rate. For a comparison, a 2D mesoscale model, a 2D homogeneous model and a 3D homogeneous model are also analyzed for the same variation range of the strain rate.

It should be noted that in all these models, no embedded strain rate enhancement factor is considered in the properties of the constituent materials; therefore, any increase in the nominal strength of the simulated test specimen is attributable only to the dynamic effect, as well as the material heterogeneity in the case of a mesoscale model. The DIF is calculated as the ratio between the nominal strength corresponding to a certain strain rate and the nominal strength when the specimen is subjected to a quasi-static loading.

Fig. 3-24 shows the variation of the DIF with the strain rate, as obtained from the various models. Shown in the figure are also four empirical curves, namely,

a) CEB-FIP DIF model (CEB, 1993)

$$DIF = \begin{cases} (\dot{\varepsilon} / \dot{\varepsilon}_s)^{1.026\alpha_s} & \text{for } \dot{\varepsilon} \le 30\,\text{s}^{-1} \\ \gamma_s (\dot{\varepsilon} / \dot{\varepsilon}_s)^{1/3} & \text{for } \dot{\varepsilon} > 30\,\text{s}^{-1} \end{cases} \tag{3.14}$$

where $\dot{\varepsilon}_s$ = 30 × 10-6 s^{-1} (static strain rate), $\log\gamma = 6.156\alpha_s - 2$, $\alpha_s = 1/(5 + 9 f_{cs} / f_{c0})$, f_{cs} is static compressive strength , and $f_{c0} = 10\,\text{MPa}$.

b) Empirical model proposed by Tedesco and Ross (1998):

$$DIF = \begin{cases} 0.00965\log\dot{\varepsilon} + 1.058 \ge 1.0 & \text{for } \dot{\varepsilon} \le 63.1\,\text{s}^{-1} \\ 0.758\log\dot{\varepsilon} - 0.289 \le 2.5 & \text{for } \dot{\varepsilon} > 63.1\,\text{s}^{-1} \end{cases} \tag{3.15}$$

c) Empirical model proposed by Grote et al. (2001):

$$DIF = \begin{cases} 0.0235 \log \dot{\varepsilon} + 1.07 & \text{for } \dot{\varepsilon} \le 266.0\,\text{s}^{-1} \\ 0.882(\log \dot{\varepsilon})^3 - 4.40(\log \dot{\varepsilon})^2 + 7.22 \log \dot{\varepsilon} - 2.64 & \text{for } \dot{\varepsilon} > 266.0\,\text{s}^{-1} \end{cases} \tag{3.16}$$

d) Semi-empirical data available in Lu and Xu (2004), which may be expressed by the following regression relationship:

$$DIF = \begin{cases} 1 + 0.15\dot{\varepsilon}^{0.2} + 0.0013\dot{\varepsilon}^{1.1} & \text{for compression} \\ 1 + 1.505\dot{\varepsilon}^{0.295} & \text{for tension} \end{cases} \tag{3.17}$$

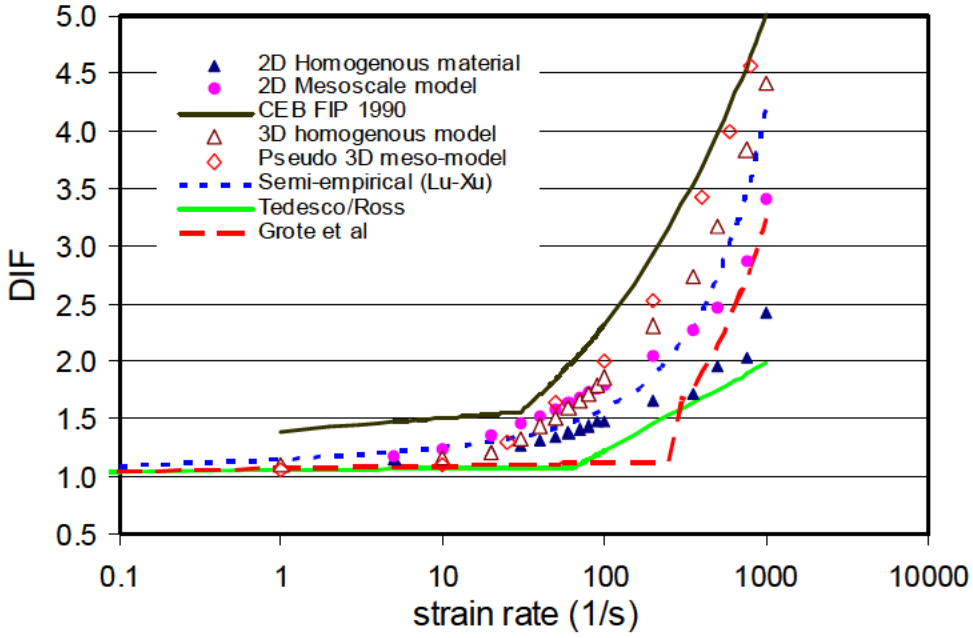

Figure 3-24: "DIF" results from the mesoscale analysis comparing to empirical formulas

It should be noted that the dimension of the concrete specimen (50mm) in the numerical experiment is adequate for strain rates up to about $100s^{-1}$. The DIF in the higher strain rate range does not satisfy the stress equilibrium requirement for the size of the specimen, therefore the DIF results in this range may be considered for a reference purpose only.

The results shown in Fig. 3-24 permit the following observations to be made:

1) All the models exhibit a significant increase in the nominal compressive strength as the strain rate increases, despite that no strain rate enhancement has been considered at the material constitutive property level. All the simulated DIF curves resemble the general trend as given by the empirical formulas.

2) The lateral inertia confinement effect, as demonstrated from the results using the homogeneous models, is shown to be a major contributor to the observed DIF. Due to a lack of representation of the lateral inertia-induced confining effect in the third (hoop) direction, the 2D homogeneous model markedly underestimates the DIF in the specimen. The contribution of heterogeneity on the DIF will be further examined in Chapter 4.

3) The mesoscale heterogeneity proves to also play a sensible role in the total DIF, especially in the high strain rate regime. The results from the pseudo 3D mesoscale model appear to be consistent with the results from the 2D and 3D homogeneous model, with however a further increase in the DIF. However, the results from the 2D mesoscale model exhibits certain irregularity and this may be attributed to the complication in the 2D mesoscale model as discussed in Section 3.

3.8 Concluding remarks

This chapter presents the development of a mesoscale model with consideration of the 3D effects for the simulation of concrete under complex and dynamic loading conditions. The limitation with a 2D mesoscale model for concrete under high strain rate compression is investigated. Due to the significance of lateral inertia-induced confining effects and its variation under different loading rates, neither a 2D plane stress nor a 2D plane strain model can replicate realistically the lateral inertia confining effects in an actual 3D specimen. A mesoscale model involving a thin layer of elements in the thickness direction is shown to exhibit an abnormal sensitivity to the thickness, and this is attributable to the complication arising from the unexpected interaction between the aggregates and the mortar elements in the thickness direction.

To eliminate the above complication in a 2D mesoscale model and to achieve a more realistic 3D inertia confining effects, a novel pseudo 3D mesoscale model with a sandwich layout is devised. This model configuration allows the development of the mesoscale features within the 2D plane in the sandwiched mesoscale layer, and at the same time preserves the inertia confining effect. For the modelling of a concrete cube sample, a half-cube sandwich model may be employed. For a cylinder specimen, a half-cylinder sandwich model is appropriate.

The simulation results demonstrate that the pseudo 3D mesoscale models behave satisfactorily in describing the mesoscale character of the response and withholding a realistic 3D inertia confining effect. The pseudo 3D model also exhibits a stable performance which is generally independent from the mesoscale layer thickness.

The simulated DIF curves using the mesoscale and homogeneous models demonstrate that, apart from the dynamic effect, the mesoscale heterogeneity also plays a sensible role in the observed DIF in the apparent dynamic compressive strength of concrete. The effect of the mesoscale heterogeneity on the DIF can be attributable to the alteration of the fracture path in the mortar matrix due to the presence of the aggregates. To a varying degree it may also be attributable to the direct contribution of the stronger aggregates to the bulk strength of the concrete composite.

Chapter 4: Mesoscopic analysis of concrete under excessive high strain-rate compression

The distinction between the past, present and future is only a stubbornly persistent illusion.

-Albert Einstein (Scientist, 1879-1955)

4.1 Introduction

The bulk compressive behaviour of concrete-like materials is experimentally observed to be strain-rate dependent (e.g. Gary, 1990; Ross et al., 1995; Grote et al., 2001; Zhang et al., 2009). In Chapter 3, a novel pseudo 3D mesoscale model with a sandwich layout has been presented, and numerical analysis results using the model have demonstrated that the lateral inertia confinement effect is indeed a major contributor to the experimentally observed apparent DIF.

One important consideration in evaluating and interpreting the dynamic response of a material specimen under high strain rate compression is how stress and strain distribute within the sample specimen. As a general guide, reasonable stress uniformity should be achieved before the specimen reaches failure so that the externally measured (or inferred) strength and deformation data at failure may be considered as representative of the bulk material behaviour. In conventional SHPB testing of metallic materials, a common approach for achieving uniform stress state is to restrict the sample length within a specific limit for a target strain-rate range, so that a uniform stress state can be built up in the course of stress wave reflections (Davis and Hunter, 1963; ASM Handbook, 2000). The diameter of the specimen is governed by a proper aspect ratio (length to diameter). To minimize the influence of radial and longitudinal inertia as well as friction effects, an optimum aspect ratio for

the specimen is recommended (Davis and Hunter, 1963). For a cylinder metallic specimen, ASM Handbook recommends the ratio to be 0.5~1.

For metallic materials, it is not difficult to satisfy the stress uniformity requirement in a conventional SHPB test since metal samples can be made sufficiently small. However, this is not the case for non-metallic, non-homogeneous materials such as concrete and rocks, for which large size specimens are required to cater to the heterogeneity, and consequently the need of using large diameter pressure bars.

One issue that needs to be considered when a large diameter bar is used is the wave dispersion effect, which may influence the accuracy of the test due to the change of pulse shape in propagation. Zhao and Gary (1996) reported that strong wave dispersion was observed in large diameter pressure bars, and consequently correction for the wave dispersion effect is necessary for small strain measurement. Since then, a number of investigations have been undertaken to develop appropriate correction techniques (e.g. Gong et al., 1990; Zhao and Gary, 1996; Zhao and Gary, 1997; Bacon, 1999).

Whereas the aspect ratio requirement is easier to satisfy in large-diameter SHPB tests and the dispersion effect may be rectified to a certain extent, one can face a dilemma when comes to choosing a suitable specimen size for testing concrete-like materials in the high strain rate regime. On one hand, a reasonable representation of the bulk composite behaviour requires a specimen size to be at least a few (typically 4~5) times of the largest grain (aggregate) in the composite. On the other hand, the need to accommodate tests into high strain rate regime, for instance above 100 s^{-1} , dictates that the specimen length should be kept well within a few centimetres. The commonly adopted practice of using scaled concrete, typically mortar, is an obvious attempt to balance between the above two conflicting requirements. However, to better preserve the characteristics of the concrete material the choice of larger size specimens becomes inevitable, and in such cases it is hardly possible to satisfy the size limit for the higher end of strain rates of interest. In fact, a variety of specimen sizes have been used both in experimental tests and numerical SHPB simulations, ranging from 10 mm mortar cubes to as large as 300 mm concrete cylinders (e.g.

Bischoff and Perry, 1991; Ross et al., 1995; Grote et al., 2001; Li and Meng, 2003; Zhou and Hao, 2008). The employment of larger specimens without observing the requirement of stress uniformity could lead to incorrect interpretation of the strain rate effect. Unfortunately such an important factor has not always been examined rigorously in the existing studies in this area.

Dioh et al. (1995) argued that the presence of large plastic wave front in the specimen during a test would render the classical SHPB test method erroneous. Meng and Li (2003b) evaluated qualitatively the axial and radial stress uniformity using a FE model. However, little effort has been paid to provide a rigorous assessment regarding the effect of stress non-uniformity on the behaviour of the test specimen and how the actual response within the specimen would correlate with the externally measured data. As a matter of fact, such correlation could provide vital guidance for the correct interpretation of the measured data from SHPB type of tests, especially in cases where the specimen size or strain rate limit is not strictly satisfied.

This chapter will aim to address the following two main questions: 1) What is the stress and stain state of a specimen if the stress uniformity is not satisfied, and how does the material actually behave within the specimen in such cases? 2) How do the externally measured strength and strain data correlate with the actual dynamic behaviour of the material?

Furthermore, the general inertia effect on the dynamic behaviour of concrete will be further examined, especially in the higher end of the strain rate spectrum, and the contribution of the material heterogeneity (i.e. aggregates) towards the bulk dynamic behaviour of the material will be scrutinised with quantification.

4.2 Theoretical background and implications

Strictly speaking, two basic assumptions should be satisfied in order for a SHPB test to be valid, namely,

a) One dimensional elastic wave propagation is ensured within the pressure bars and the specimen, and

b) Stress state within the specimen is uniaxial and uniform.

To meet the second requirement, several reflections of the stress wave are needed for a uniform stress state to build up. Thus, the time required for the stress to reach equilibrium may be written as *n* number of wave travel time within the specimen, i.e.,

$$t > n\frac{l_s}{c_0} \tag{4.1}$$

where l_s is the length of specimen, c_0 is the sound wave speed in the specimen. The integer n is recommend to be 3~4 based on experimental observations (e.g. Davis and Hunter, 1963; Follansbee, 1985; Pankow et al., 2009).

Accordingly, an upper limit of strain rate that can be accommodated in a specimen satisfying the above requirement will be:

$$\dot{\varepsilon} = \frac{\varepsilon_f}{t} < \frac{\varepsilon_f c_0}{n l_s} \tag{4.2}$$

where ε_f denotes the failure strain.

This equation indicates that for a given specimen length, a limiting strain rate exists for a reliable SHPB test. Conversely, if one intends to test the material strength up to a specific strain rate level, the length of the specimen should be smaller than a critical value. Take grade 30MPa concrete for example, assuming a failure strain of 0.002, mass density of 2300Kg/m^3, and Young's modulus of 20GPa, a standard specimen of 50mm in length can only accommodate a strain rate limit of approximately 50s^{-1}. For this class of concrete, the relationship between the specimen length and the strain rate limit can be depicted by a graph shown in Fig. 4-1.

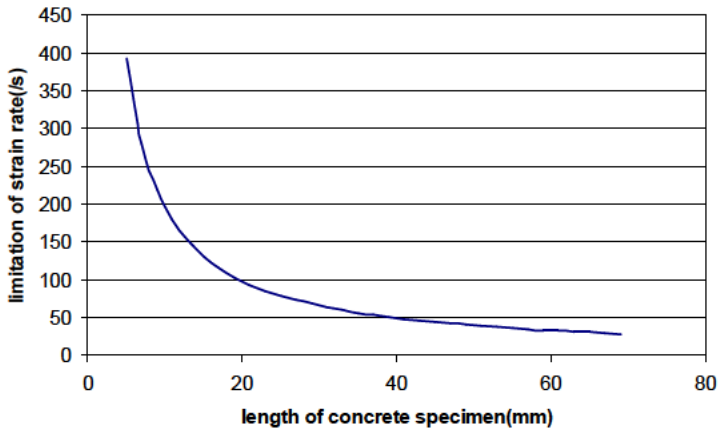

Figure 4-1: Relationship between specimen length and strain rate limit for 30-MPa concrete

Examining the experimental data available in the literature for concrete-like materials under dynamic compression, for example those presented in Bischoff and Perry (1991), Ross et al. (1995), Grote et al. (2001), numerous data points towards the high strain rate end appear to fall beyond the upper strain rate limits for the respective specimens. For example, In Ross et al. (1995) concrete specimens of length 51mm were used; theoretically this would restrict the valid strain rate range to be below 40~50s^{-1} . However, the actual tests extended to a strain rate as high as 1000s^{-1}. Bischoff and Perry (1991) acknowledged that in the higher strain rate regime, "strain rate measurements are sometimes quite erratic".

A special specimen configuration worth mentioning is that employed in an impact experiment by Riedel et al. (2009) for strain rates up to 10^5~10^6s^{-1} . The specimen was assembled by multiple blocks, such that stress gauges could be attached to the interface of the concrete blocks, which were then glued together with epoxy. As the damage of specimen under impact loading is highly localized within a narrow region, this physically separated "layered" specimen configuration helped address the measurement of shock wave propagation at high strain rates. However, this technique does not resolve the problem for testing concrete-like material with large heterogeneity that requires a specimen of sufficiently large size in all directions.

4.3 Model set-up for high rate compression simulation

4.3.1 Fictitious strips for evaluating wave propagation effects

A cylinder specimen of 50 mm (diameter) × 50 mm (length), as commonly used in SHPB tests of concrete, is considered. The maximum aggregate has a nominal size of 8mm, which is about one sixth of the sample dimension. A pseudo 3D mesoscale model, as described in Chapter, is developed to model such a specimen. Mesh convergence trials yielded a final FE mesh with a gird size of around 0.5 mm for the sandwiched mesoscale slice. Totally around 11,700 elements are used in the mesoscale slice (with a single element thickness), while around 30,000 elements are used to model the half-cylinder homogeneous part. Considering symmetry, only half of the cylinder is modelled, with a symmetrical condition being imposed on the front face of the mesoscale slice (see Fig. 3-22).

Examination of the responses is focused within the mesoscale part of the model. To facilitate the evaluation of the stress-strain distribution while the stress wave propagates and reflects between the two end faces, the mesoscale region is fictitiously divided into five equal strips along the loading (axial) direction, with a width of 10mm for each strip, as depicted in Fig. 4-2.

The nominal strain rate in each strip is evaluated from the average nodal velocities over the two dividing lines bounding the strip. The strip-wise axial stress and strain are calculated as the average axial stress and strain among all the elements within the strip. With these data, a correlation between the achieved stress-strain behaviour at different parts of the specimen and their global “engineering” counterparts, which are evaluated using stresses and velocities measured on the loading (incident) and support (transmission) faces, can be examined in detail.

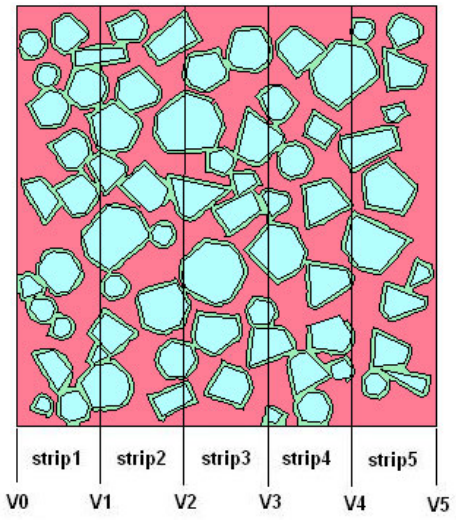

Figure 4-2: Specimen being divided into 5 strips for evaluation of stress and strain distributions

4.3.2 Investigation of simplified loading schemes for resembling SHPB tests

There are two obvious options in the computational model set-up for simulating a high rate compression test using a SHPB apparatus. One is to include the incident and transmitter pressure bars explicitly in the model and apply actions on the input end of the incident bar, as adopted in some previous studies (e.g., Li and Meng, 2003; Lu and Tu, 2008). The other is to apply actions directly on the specimen via prescribed time varying boundary conditions at the two end faces (e.g., Donze et al., 1999; Riedel et al., 2008; Riedel et al., 2009). The formal approach would simulate more realistically the loading environment as in a physical SHPB test, but computational cost would increase; and moreover, describing the exact loading condition applied on the test sample would become less straightforward. Using the second approach is computationally more efficient, and when the boundary histories are carefully specified it is possible to capture the main loading and response characteristics as in an actual SHPB environment. For these reasons, and considering that an “exact” reproduction of a SHPB test condition is not of critical importance for the current investigation, the second option is considered as rational and this approach is adopted in the present study.

As a matter of fact, if actual boundary (usually velocity) histories as measured from a SHPB test are specified in the numerical sample, the result would be equivalent to the inclusion of the pressure bars. Herein only an idealized velocity history is imposed on the loading face, while the end face is simplified as fully restrained in the axial direction. Analogous to the typical measured velocity histories at the incident bar-specimen interface, the idealised velocity history (Fig. 3-4) consists of a gradual rise phase, followed by a constant velocity v_{max}.

In the traditional SHPB test on metallic specimens, the incident wave is generated from the impact of a striker and incident bar. Direct planer test generally produces rectangular shaped pulse, thus a uniform strain rate can be achieved throughout the loading time. However, brittle materials such as concrete can undergo relative small elastic strain. To give enough time for the specimen to develop global deformation, pulse shaping techniques are sometimes used to increase the rise time of incident wave. Because the constant strain rate can be not attained during loading time, the measurement of strength on a specific strain rate is then questionable. When the specific strain rate is achieved and whether it's uniform throughout the specimen are all critical in the interpretation of such measurements. In this research, we will impose constant nominal strain rate on the specimen by the idealised velocity history. To avoid the non-uniformity caused by the steep rise of impulse, the gradual rise phase are chosen to be 0.02ms for $50s^{-1}$ and $100s^{-1}$ test, 0.01 ms for $200s^{-1}$ test. The choice is made based on experimental observation from Gorham (1997), Tedesco and Ross (1998) and Meng and Li (2003).

For verification on the sensitivity of the simulation results to the simplification in the velocity boundary condition, a comparative analysis was carried out with different velocity boundary settings, including one that was adapted from the measured velocity histories in an actual SHPB test, as presented in Meng and Li (2003a). Three velocity boundary scenarios are considered, as shown in Fig. 4-3, namely, a) idealized incident velocity only (with the transmitter end fixed), b) idealized incident velocity with "measured" transmitter velocity, and c) "measured" incident and "measured" transmitter velocities. The maximum incident velocity is

about 7.5 ms^{-1} to result in a nominal strain rate around $150s^{-1}$ in the present 50-mm specimen.

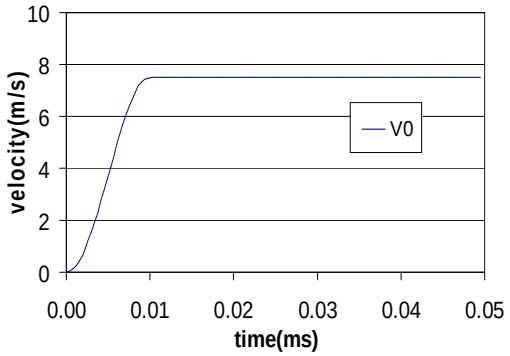

(a) v_0 = idealised; v_5 = 0

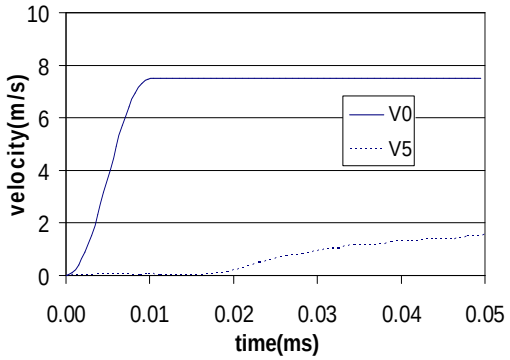

(b) v_0 = idealised; v_5 = measured

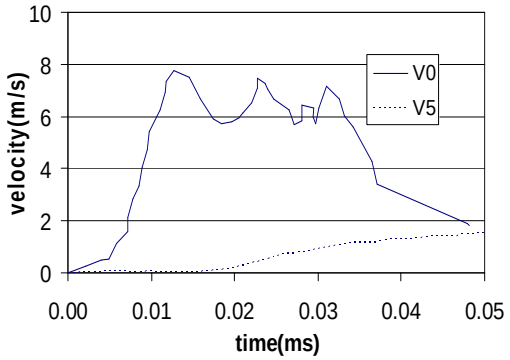

(c) v_0 & v_5 = measured

Figure 4-3: Three velocity boundary schemes

Representative results from the analysis under the above three velocity boundary scenarios are compared in Fig. 4-4 and Fig 4-5. The achieved overall forces on the loading (incident) face (F_1) and transmitter face (F_2), shown in Fig. 4-4 (a), are similar among the three loading schemes. Small fluctuations in F_1 of scheme (c) could be caused by the fluctuations in loading velocity. Damages at the peak strength of F_2 are shown in Fig. 4-5. In scheme "a" and "b", development of damage agrees well with each other, while in scheme "c" elements close to the transmitter boundary are shown to have slightly less damage. Further examination into the detailed stress and strain responses in each strip, Fig. 4-4 (b)-(c), indicates that under a more realistic loading condition (scheme (c)), peak strength in the first strip is developed slower than scheme (a), this is mostly because lack of an exact match between idealised and realistic loading curves. Further, strips close to the end (transmitter) face tend to exhibit slightly lower peak strength compared to the idealised loading scheme. However, the stress and strain closer to the incident face are similar among all three loading schemes. The achieved strain rates (slope in strain-time curves) are close to $150s^{-1}$ in all three scenarios.

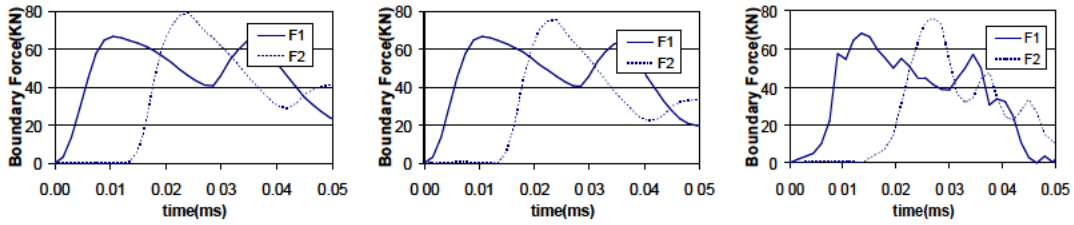

a) Incident (front) and transmitter (back) force histories

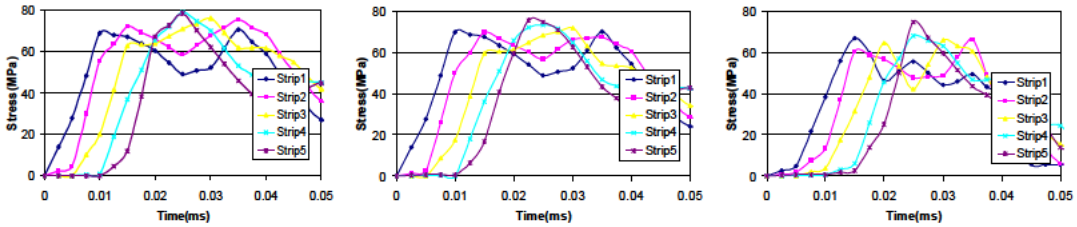

c) Strip-wise stress histories

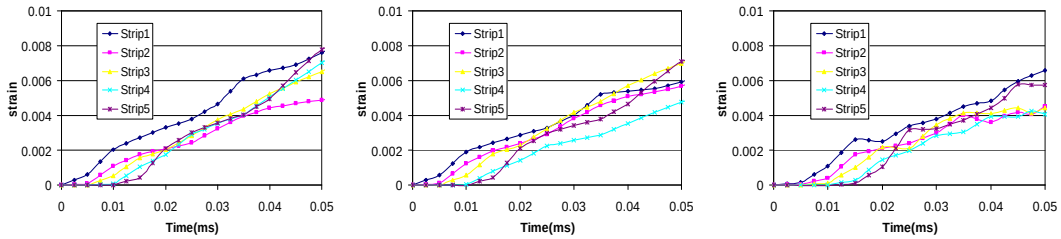

d) Strip-wise strain histories

Figure 4-4: Comparison of responses corresponding to the three different velocity boundary conditions shown in Fig. 4-3

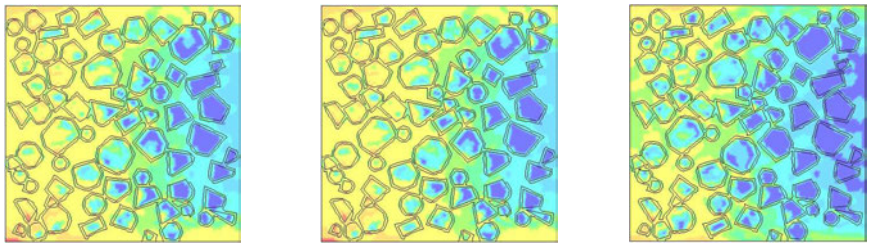

Figure 4-5: Comparison of damage contours corresponding to the three different velocity boundary conditions shown in Fig. 4-3

It appears that with the idealised loading (scheme a) some degree of over-representation of the stress tends to occur near the transmission end due to the exclusion of transmission effect. However, the magnitude of stress and strain in the first few strips resembles well the actual condition. Moreover, for the primary interest of this study which is concerned about the characteristics of the propagating stress wave and the associated effect at the local (strip) and global (specimen) levels under excessive high strain rate, such limited derivation near the transmission end should not cause sensible discrepancy in the main observations.

4.4 Numerical investigation of dynamic compression: stress wave effect

4.4.1 Stress development path and distribution

Three strain rate levels are chosen for examining the response in the mesoscale model, namely, $50s^{-1}$, which represents an upper limit strain-rate for the 50×50 mm

concrete specimen, and $100s^{-1}$ and $200s^{-1}$ to represent two levels of "excessive" strain rate conditions for such a specimen dimension.

Fig. 4-6 shows the development of (average) axial stress in the five strips for the above three strain rates, respectively, along with the corresponding damage patterns.

For the nominal strain rate of $50s^{-1}$, all strips appear to reach the maximum strength more or less at the same time. This tends to confirm that a relatively uniform stress state could indeed be achieved when the applied strain rate is generally within the theoretical upper limit. In fact from the stress histories it can be observed that two complete reverberations have occurred before the maximum strength is reached. The damage patterns also confirm that a relatively uniform stress was indeed established when the maximum strength was reached in the specimen (stage III in the figure).

As the strain rate increases to $100s^{-1}$, which is about twice as much the limit strain rate, individual strips tend to attain maximum strength at different times. Only the front part (first two strips on the incident side) appears to have experienced two reverberations of the stress wave. The non-uniformity of stress and damage along the length of the specimen can also be clearly observed from the damage contours; when the front part (Strips 1 and 2) reaches the maximum stress and fails (stage II in the figure), much of the remaining region is still intact. Failure appears to develop in the specimen in a strip by strip manner.

Under a further increased strain rate of $200s^{-1}$, the stress non-uniformity is further intensified. The stress histories and the damage contours indicate that individual strips enter the maximum strength (and failure) consecutively as the first peak stress propagates from the loading face through to the end face.

The dynamic axial strength in individual strips apparently increases with the increase of the strain rate, which is consistent with the increase of the bulk DIF shown in Fig. 3-24. At the strain rate level of $50s^{-1}$, the maximum strengths achieved in different strips are effectively identical. The maximum strengths achieved in individual strips under the strain rate of $100s^{-1}$ are also almost the same. For the 200 s^{-1} case, the maximum strength tends to show a noticeable decrease towards the

middle of the specimen, with strip 3 showing a maximum strength about 10% lower than that at both ends. It should be noted at this juncture that no lateral friction constraint is incorporated in these numerical experiments; therefore the relatively higher maximum strength near the two ends could only be attributed to a relatively higher strain rate, and hence an increased lateral inertial confinement. This will be elaborated further in the section that follows.

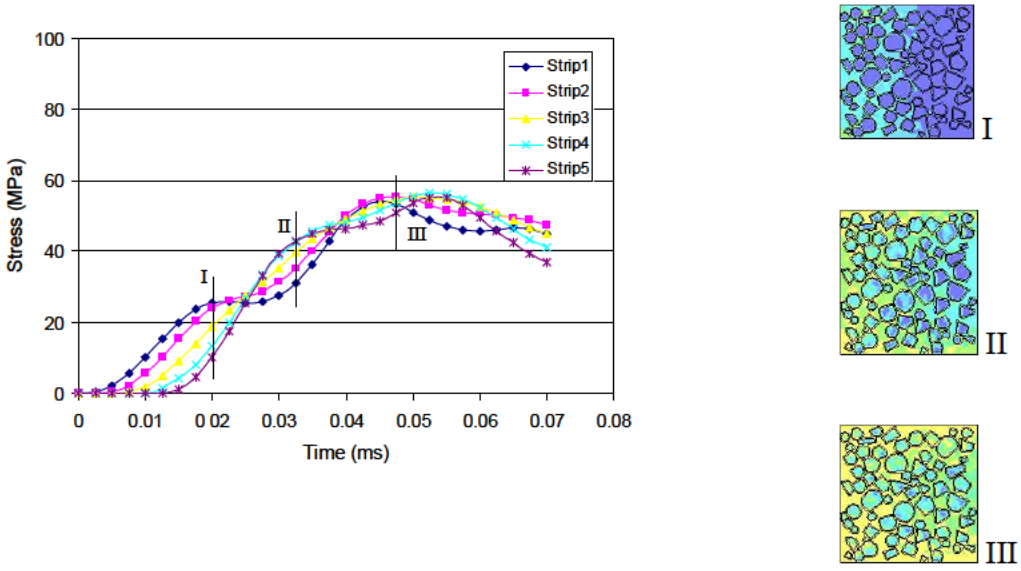

a) Nominal strain rate = $50s^{-1}$

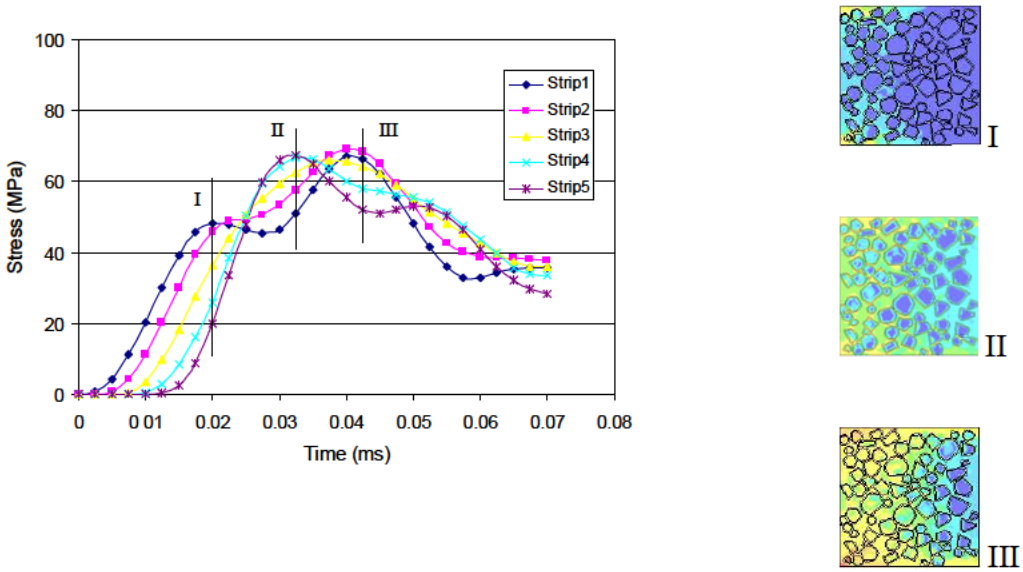

b) Nominal strain rate = $100s^{-1}$

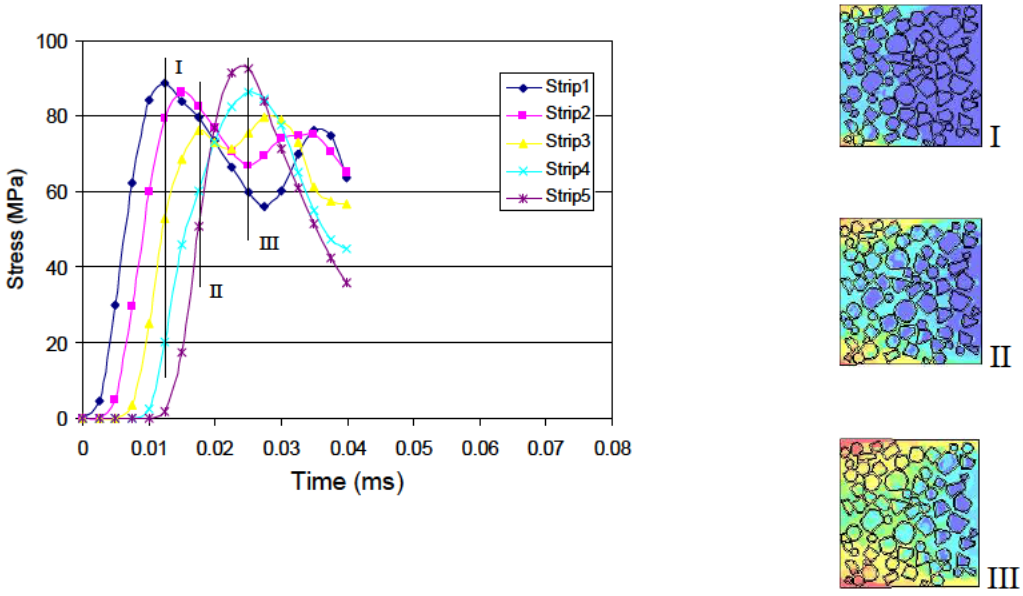

c) Nominal strain rate = 200s^{-1}

Figure 4-6: Stress time histories in individual strips

4.4.2 Strain development path and distribution

Fig. 4-7 shows the strain development history under a global strain rate of 50 and 200s^{-1} respectively. The nominal strain within each strip can be calculated either as the average of axial strain in all elements within the strip or from average nodal velocities on the two bounding lines. The results (not shown) are found to agree well with each other. The latter is shown in the following strain history and stress-strain curve.

For the lower strain rate (50s^{-1}) case, the strain in different strips tend to be comparable after the initial wave build-up stage (Fig. 4-7(a)), similar to the stress development shown in Fig. 4-6 (a) before failure occurs (up to about 0.05 ms). When failure starts to occur the strain rates (slope of the strain time history curves) in individual strips are almost identical, indicating that the global strain-rate as derived from the measurements on the two end faces is representative of the actual strain rate inside the specimen.

In the case with $200s^{-1}$ strain rate, similar to the failure stress development shown in Fig. 4-6 c), individual strips attain the failure strain (around 0.002) in a consecutive manner as the stress wave propagates from the front (incident) end to the support end. Inspection of the slope (i.e. strain rate) when the failure occurs, as marked with the dashed lines, reveals noticeable variation among different strips, and it tends to decrease towards the middle and then increase again as the wave approaches the support end. This appears to explain the variation in the maximum strength attained in different strips, as described in Section 4.5.1.

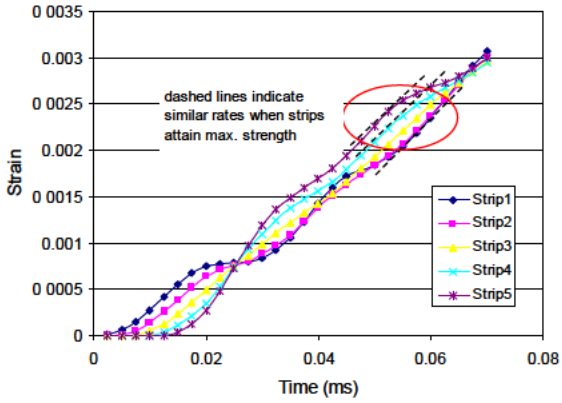

a) Global strain rate = $50s^{-1}$

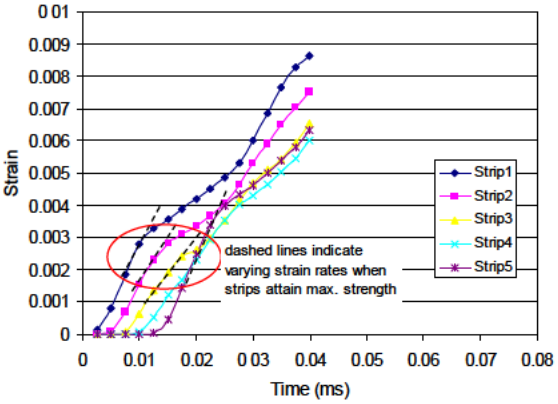

b) Global strain rate = $200s^{-1}$

Figure 4-7: Strain time histories in individual strips

4.4.3 Stress vs. strain relationships

With the stress and strain results as described in Section 4.4.1 and 4.4.2, the stress-strain relationships can be plotted for each individual strip. Fig. 4-8 shows the strip-wise stress-strain curves under two global strain rates of $50s^{-1}$ and $200s^{-1}$, respectively.

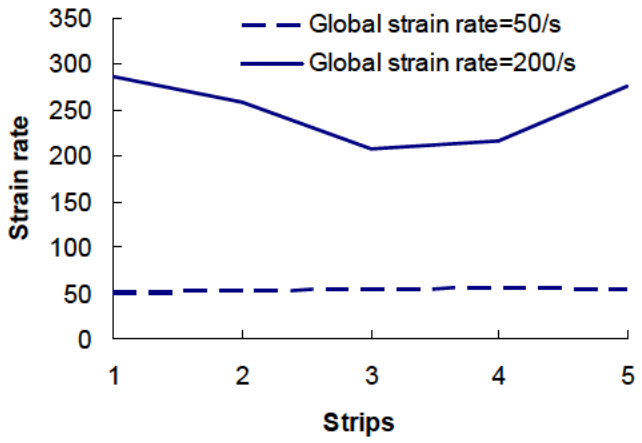

Figure 4-8: Strain rate profile corresponding to attainment of maximum strength in individual strips

The stress-strain curves are observed to be consistent among different strips, even for the $200s^{-1}$ case. The peak strengths in different strips in the 50 s^{-1} case are almost identical, although the strains at the attainment of the peak strength do not coincide exactly. As discussed in Section 5.5.2, in the 200 s^{-1} case the peak strength tends to decrease towards the middle portion of the specimen. Nevertheless, the overall stress-strain characteristics are still similar among individual strips. As can be observed comparing the stress-strain curves across the two different strain rate scenarios, the Young's modulus is almost unaffected by the different strain rates, and stands around 30GPa in both strain rate scenarios. Correspondingly, the strain at the peak strength increases almost proportionately as the peak strength increases with the strain rate. This will be discussed further in Section 5.6 in association with the discussion on the relevant experimental data.

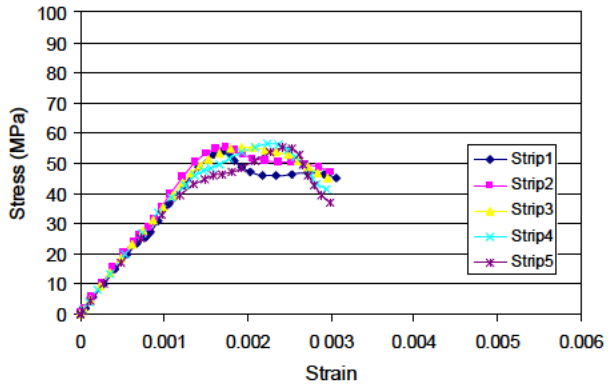

(a) Nominal rate = 50 s^{-1}

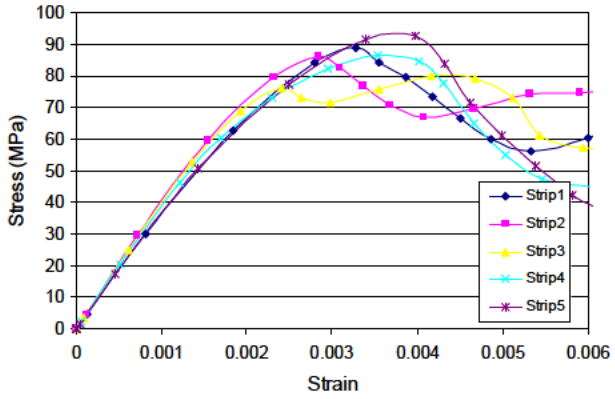

(b) Nominal rate = 200 s^{-1}

Figure 4-9: Stress vs. strain curves in individual strips

4.5 Discussion on the global stress-strain results from SHPB tests

As in typical SHPB tests, the global (sample-wide) nominal stress and strain responses in the mesoscale numerical model can be evaluated by following the classical 1-wave, 2-wave, and 3-wave methods (ASM Handbook, 2000). In this section, we shall examine the results evaluated using these approaches, which would represent what would be obtained from a classical SHPB experiment. By examining these results against those actually taking place within the sample specimen, as represented by the "strip-wise" results described in Section 5, it will be possible to

understand the soundness and validity of the SHPB measurements in the high strain rate regime.

The 1-wave analysis, or "back stress" analysis, is derived based on the stress equilibrium assumption in the sample, such that the force on the loading (incident) end, F_1, equals the force on the transmitter end, F_2, where

$$F_1 = A_b E(\varepsilon_i + \varepsilon_r),\ F_2 = A_b E\varepsilon_t \tag{4.3}$$

Thus the stress is calculated as

$$\sigma = F_2 / A_s = A_b E\varepsilon_t / A_s \tag{4.4}$$

where A_b and A_s are the cross section area of the pressure bar and the specimen, respectively; E is the Young's modulus of the pressure bar. Subscripts i, r and t indicate the incident, reflected and transmitted pulse, respectively. The global engineering strain rate is:

$$\dot{\varepsilon} = (v_1 - v_2) / l_s = 2c\varepsilon_r / l_s \tag{4.5}$$

where v_1 and v_2 are the velocities at the incident and transmitter ends, respectively, c is the wave speed and l_s is the length of specimen. The above analysis uses only the reflected wave to compute strain and only transmitter wave to compute stress.

The 2-wave method assumes that a momentum balance is achieved after the incident strike on the incident bar-sample interface, and hence

$$\sigma = F_1 / A_s = AE(\varepsilon_i + \varepsilon_r) / A_s \tag{4.6}$$

Finally the 3-wave analysis averages the measurements associated with both the incident and transmitter ends, thus,

$$\sigma = (F_1 + F_2) / 2A_s = (AE / 2A_s)(\varepsilon_i + \varepsilon_r + \varepsilon_t) \tag{4.7}$$

$$\dot{\varepsilon} = (v_1 - v_2) / l_s = (c / l_s)(\varepsilon_i - \varepsilon_r - \varepsilon_t) \tag{4.8}$$

and

$$\varepsilon = (c / l_s)\int (\varepsilon_i - \varepsilon_r - \varepsilon_t)dt \tag{4.9}$$

Fig. 4-10 illustrates the global (engineering) stress-strain curves obtained using the above-mentioned 1-wave, 2-wave and 3-wave analysis, respectively, with the strip-wise results at the background.

For the 50 s^{-1} case, the global stress-strain relationship curves using the three different wave methods may be considered as consistent in terms of the peak stress and strain, and they reasonably resemble the strip-wise results.

For the "excessive strain rate" case of 200s^{-1}, the discrepancy among the stress-strain curves using the three global approaches and their comparison with the "actual" stress-strain results within individual strips becomes severe. In particular, the 1-wave and 2-wave approaches, although reasonably capturing the peak strength, tends to produce a strain response which is essentially uncorrelated with the actual strain within the specimen. Consequently, the Young's modulus is considerably overestimated, while the peak strain is significantly underestimated. Averaging between the incident and transmitter ends, i.e., using the 3-wave approach, appears to improve the overall resemblance of the resulting stress-strain curve to stress-strain response within the specimen. However, because of a significant time lag between the F_2 and F_1 responses, such an averaging process is not physically meaningful.

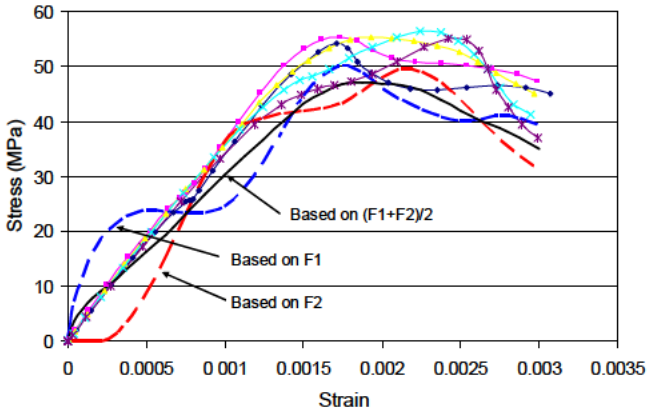

a) Nominal rate = 50 s^{-1}

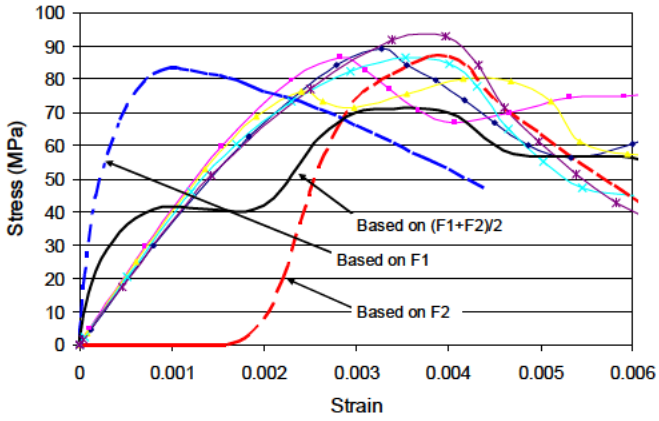

b) Nominal rate = 200 s^{-1}

Figure 4-10: Stress-strain curves inferred from the three different wave approaches

At this juncture, it is useful to call upon some comparable experiment studies on concrete using SHPB tests. In the experimental study by Ross et al. (1995), where specimens of 51 mm in length were tested, the uniform-stress assumption was adopted and consequently the global (engineering) strain, stress and strain rate were calculated following the 1-wave approach. The study by Grote et al. (2001) used exactly the same calculation conventions in processing their experimental results for mortar specimens of length around 10mm. Li and Meng (2003) adopted the 3-wave approach in analyzing their numerical SHPB results.

Fig. 4-11 shows two sets of the compressive stress-strain curves based on the above mentioned two experimental studies. Although the overall shapes of the stress-strain curves are similar, there are considerable discrepancies in the reported strains and the Young's modulus. While the results from Ross et al. (1995) show no apparent increase in the Young's modulus as the strain rate increases (actually an abnormal decrease is seen on the highest strain rate 337 s^{-1} case), results from Grote et al. (2001) exhibit persistent increase in the Young's modulus, along with an increase in the peak strain. It should be noted that the range of the tested strain rates in both experiments exceeded the respective maximum strain rate limit (which would be around 50s^{-1} for the case of Ross et al. (1995) and 300s^{-1} for the case of Grote et al. (2001)). It is not clear as to what exactly caused such discrepancies in the two sets of experimental results, where the same data processing method (1-wave method)

was adopted. However, on the basis of the earlier discussion in association with the numerical results presented in Fig. 4-11, it may be reasonable to suspect that the strain results produced from the above experimental studies were not directly applicable as a representation of the true strains experienced by the materials within the test specimen. Without an appropriate measure of the "strip-wise" strains, it would be difficult to establish the true strains just based on the measurements taken at the incident and transmitter ends (through measurements within the incident and transmitter bars).

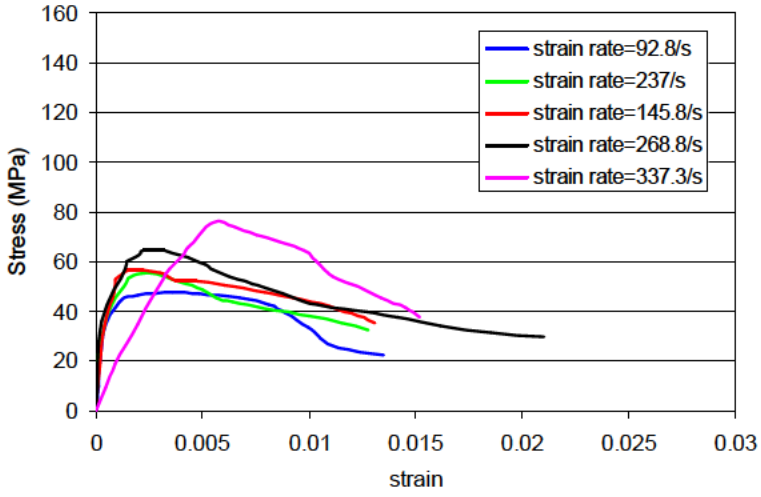

(a) After Ross et al. (1995)

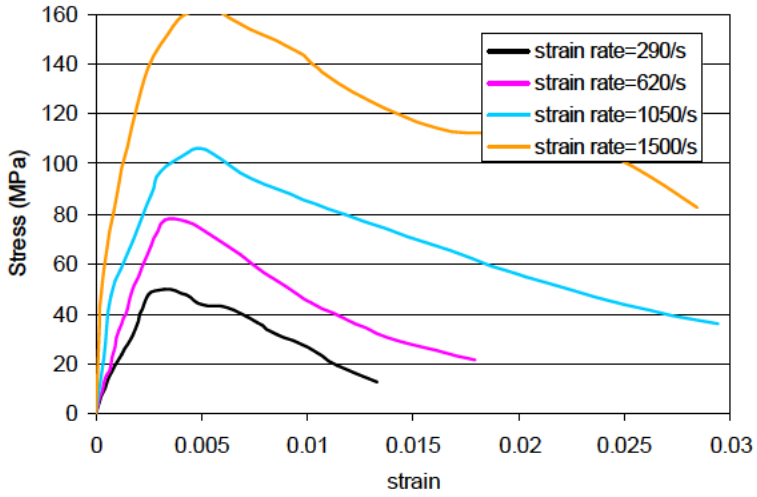

(b) After Grote et al. (2001)

Figure 4-11: Representative experimental stress-strain curves

4.6 Mesoscopic evaluation of DIF under compression

As discussed in Section 4.3 and 4.4, the lateral inertial confinement is deemed to be a dominant factor influencing the bulk dynamic strength increase of concrete-like materials under compression, while the presence of mesoscopic heterogeneity also plays a noticeable role. In this section, we shall take a closer look at how each phase in the meso-structure of concrete behaves in the dynamic response process.

For this purpose, the average axial stresses developed in each individual phase are computed for the two representative strain rates of 50 and 200s^{-1}, respectively. Strip1 and Strip 3 are chosen for an examination within individual strips. For simplicity, the ITZ and mortar are combined as the "mortar" phase to compare with the stresses in the aggregates. The results in a homogeneous model of 30MPa concrete, which does not involve the heterogeneity effect, are also provided as a benchmark for the comparison.

Fig. 4-12 and 4-13 shows the comparison of the development of axial stresses in the mesoscale and homogeneous models. It can be immediately observed that the aggregate phase develops a markedly higher axial stress than the mortar phase, and the difference broadens as the strain rate increases. Comparison with the homogeneous model shows that the stress in the mortar phase in the mesoscale model develops almost the same axial stress as in the homogeneous model for the same strip and under the same strain rate. This further indicates that the extra stress developed in the aggregates in the mesoscale model represents a net gain in the dynamic strength, and thus contributes to the global DIF.

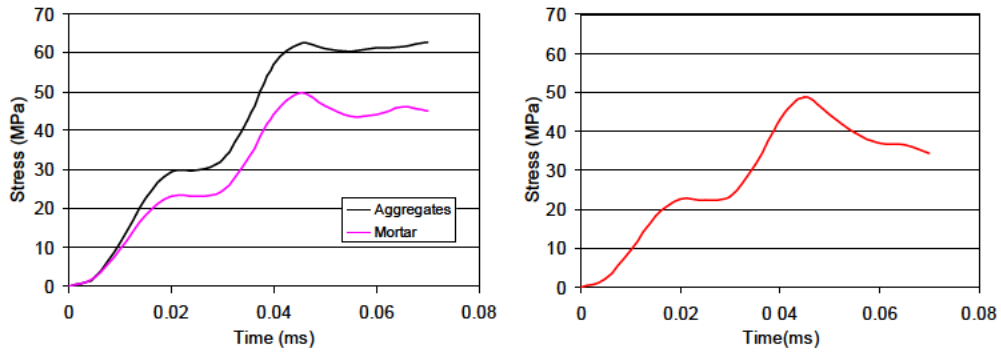

a) Strip 1 of mesoscale model **b) Strip 1 of homogeneous model**

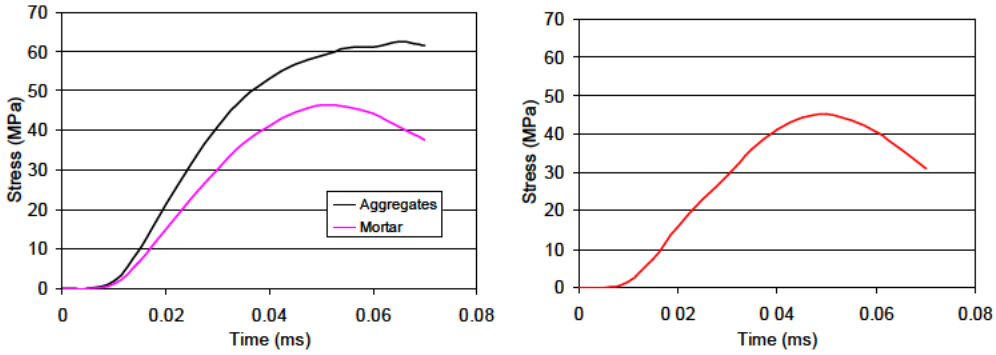

c) Strip 3 of mesoscale model **d) Strip 3 of homogeneous model**

Figure 4-12: Axial stresses in mortar and aggregates, and comparison with stress in the homogeneous model, strain rate = 50s^{-1}

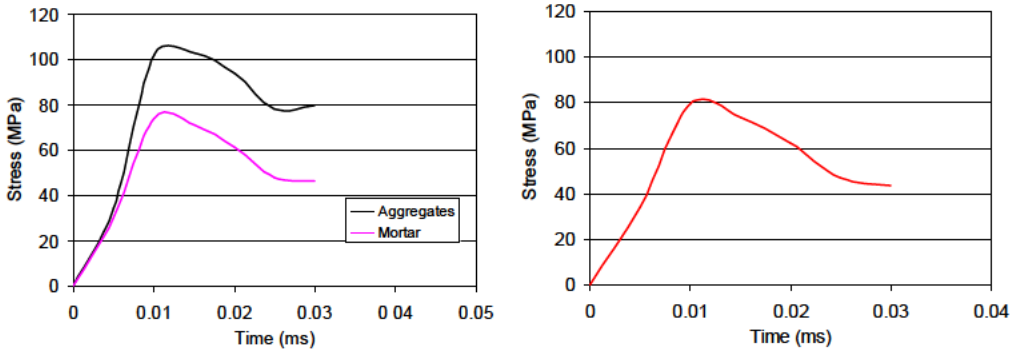

a) Strip 1 of mesoscale model **b) Strip 1 of homogeneous model**

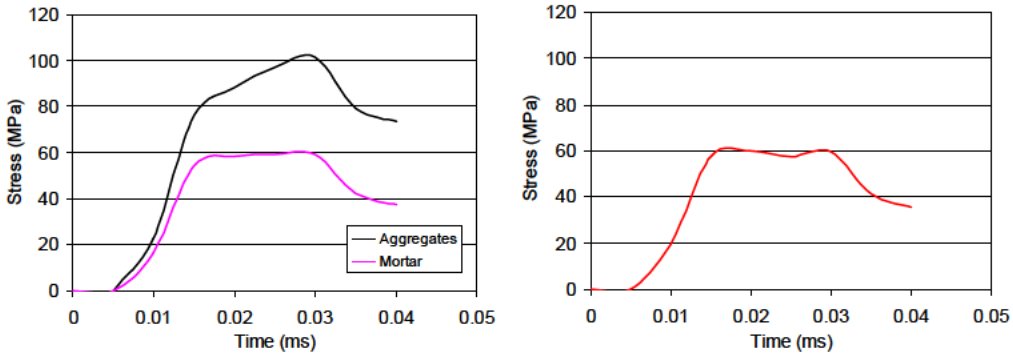

c) Strip 3 of mesoscale model **d) Strip 3 of homogeneous model**

Figure 4-13: Axial stresses in mortar and aggregates, and comparison with stress in the homogeneous model, strain rate = 200s^{-1}

Fig. 4-14 shows the stresses in the mortar and aggregate phases at different strain rates. A lower rate of $10s^{-1}$ is also included. As can be seen, under a low strain rate, the maximum stress in mortar and aggregates are almost identical, which indicates an essentially homogeneous stress state despite the heterogeneity, as is generally the case with quasi-static compression. When the strain rate increases to $50s^{-1}$, the maximum stress in the aggregates is higher than the stress in the mortar by about 20-25%, and the difference further increases to about 50% under the strain rate of $200s^{-1}$. Noting that in a typical concrete specimen, course aggregates generally makes up about 40% in the total volume, thus a significant increase in the stress in the aggregates would immediately manifest as an appreciable increase in the overall dynamic strength, and hence in the DIF. It should be noted that at the strain rate regime currently investigated, the aggregates generally remain in the elastic stage, thus the stress development in the aggregates is rather independent from the lateral inertia confinement condition.

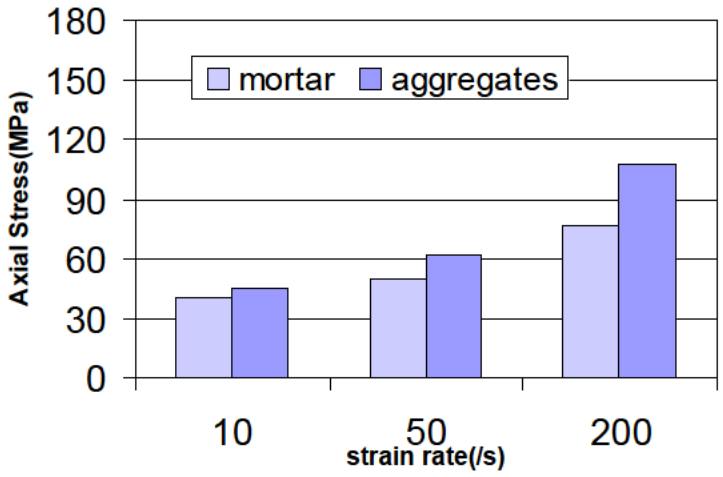

Figure 4-14: Axial peak stress in mortar and aggregates.

As indicated earlier in Section 4.4, it tends to be increasingly accepted that the lateral inertia confinement, coupled with the pressure dependency of the constitutive material behaviour, is a key mechanism causing the experimentally observed dynamic increase of the bulk compressive strength of concrete, and hence the DIF. Numerical studies using refined FE models with homogenised material properties, without involving any strain rate sensitivity in the constitutive model, have been able

to demonstrate that the experimental DIF is overwhelmingly attributable to the inertia confining effect (e.g. Li and Meng, 2003). While the general trend is deemed to be out of question, at this juncture it should be pointed out that the numerical evidences associated with the magnitude of the inertia effects as derived from a homogeneous model depends directly upon the soundness as how the lateral inertia are represented, which in turn depends on the dynamic Poisson's ratio. However, such a crucial parameter is not entirely understood under dynamic loading, and in the analysis it is by default assumed to be indifferent from the static loading.

The contribution of the mesoscale heterogeneity in the DIF in the high strain rate regime, discussed above, suggests that there is at least another mechanism which can play a sensible role in the DIF of concrete-like materials, in addition to the lateral inertia. Moreover, such a contribution is rather independent of the lateral inertial effect, therefore even in a (somewhat unlikely) scenario where little lateral inertia exists due to a small dynamic Poisson's ratio, the heterogeneity effect would still prevail and hence give rise to a certain amount of the bulk DIF. A securitization of this subject is beyond the scope of the present discussion and can be investigated in a further research.

4.7 Conclusions

A mesoscopic investigation into the development and distribution of stresses in standard concrete test specimens under high strain rate compression has been presented. Particular attention has been paid to the stress wave effect and the resulting progressive damage in the specimens, especially in the strain rate regime that exceeds the strain rate limit governing a stress uniformity condition. The contribution of the large heterogeneity in concrete-like materials to the dynamic increase factor (DIF) of the bulk strength is highlighted. More specifically, the following conclusions may be drawn:

1) For strain rates up to the theoretical strain rate limit, in the present case about $50s^{-1}$ for the 50mm sample, a reasonable uniformity of stress can generally be maintained. Consequently, the nominal dynamic strength and strain quantities as obtained from

the end face responses (measured from the pressure bars in the case of SHPB tests) appear to represent well the actual bulk dynamic behaviour of the concrete.

2) With increase of the strain rate beyond the theoretical limit, the stress distribution tend to become increasingly non-uniform as the strain rate increases, and this results in progressive failure in a layer by layer fashion as the stress wave propagates from the front (incident) face towards the end (transmission) face. Consequently, the nominal strength and strain response derived using any of the three different wave methods cannot produce consistent results.

3) Relatively speaking, averaging of the responses between the two ends using the 3-wave method tends to produce better representation of the internal (strip-wise) stress-strain curve. However, because of the significant time delay in the response between the two end faces, such an averaging treatment is merely numerical and has no physical bearing. On the other hand, the 1-wave or 3-wave analysis produces a strength result which is similar to the back and front layer of the sample, as can be expected; but they tend to considerably overestimate the dynamic strain in the material. In lieu of a general guide, a dedicated numerical analysis is recommended to provide necessary correlation for the interpretation and corrections of any test data that exceed the respective strain rate limits.

4) The presence of large heterogeneity in the material, in particular the much stronger aggregates, tends to develop increasingly higher stress than the mortar matrix as the strain rate increases. This gives rise to a non-negligible mechanism that contributes to the measured bulk DIF in the concrete specimens under compressions. It is particularly noteworthy that such a mechanism is relatively independent from the lateral inertia confinement conditions, and therefore is less subject to any uncertainty in the constitutive model parameters governing the inertia effect.

Chapter 5: Numerical investigation of dynamic tension of concrete with Brazilian Splitting test

It is only with the heart that one can see rightly; what is essential is invisible to the eye.

--Antoine de Saint-Exupery (Writer, 1900-1944)

5.1 Introduction

Experimental results tend to show that the tensile strength of concrete increases rapidly with strain rate (e.g. Bischoff and Perry, 1991; Ross et al., 1989; Yu and Li, 2011). However, to conduct a dynamic tension test involves various complexities that could arise from the testing apparatuses, and in some situations the validity of the inferred test results could become questionable.

As mentioned earlier, unlike testing of metals, testing of concrete-like materials is subject to much restrictive requirements as to the shape and (minimum) size of the specimens. Generally speaking, there are three experimental methods that may be used for testing the tensile strength, namely a) direct tensile test, b) spalling test, and c) splitting Brazilian test (see for example review articles by Hughes et al. (1993) and Yu and Li (2011)). Among these three methods, the Brazilian test is deemed capable of producing most accurate and consistent results as compared with the other two methods (Neville, 1995; Hughes et al., 1993), thus this approach has been used widely in experimental studies by many researchers (Hughes et al., 1993; Tedesco and Ross, 1998; Gomez et al., 2001; Dong et al., 2006; Zhou and Hao, 2008). Direct tension test, on the other hand, has practical difficulty with the fixture of specimen in the test set-up, so this approach is less employed in practice; however it has been used often in recent numerical simulation studies (Cotsovos and Pavlovic, 2008; Lu and Li, 2011). The spalling test method, which avoids the fixture problem, is considered to be capable of achieving strain rate $100s^{-1}$ (Yu and Li, 2011). However,

due to the indirect measure to the tensile stress and strain, it tends to give overestimation of the tensile strength compared with the other two approaches (Neville, 1995).

In typical Dynamic Increase Factor (DIF) curves for concrete under high strain-rate tension, results based on above testing methods consistently exhibit a sharp turning point at a certain strain-rate "threshold", although the actual threshold values differ in different proposals of the DIF curves. For example, from Hughes et al. (1993) the threshold strain rate appears approximately at $5s^{-1}$, whereas in CEB DIF recommendations (CEB FIP, 1993) this is chosen to be $30s^{-1}$. There have been different explanations for the existence of such a sharp transition point (Tedesco and Ross, 1998; Lu and Li, 2011), and a more recent argument is to associate the phenomenon with the material dynamic response (Lu and Li, 2011).

In the present study, however, we postulate that this phenomenon has more to do with the splitting test method than any intrinsic tensile behaviour of the material. We shall demonstrate that this particular testing technique would fail to withhold the presumed "splitting tension" state when the loading rate exceeds a certain level, which is found to correspond closely to the above-mentioned strain rate threshold. Thus, the "threshold" strain rate appears to actually mark a transition of the dynamic structural behaviour of the specimen, and consequently the second branch of the DIF curve may not be valid in representing the tensile strength of the material in the higher strain rate regime, at least for the tests data derived from splitting tests.

In this chapter, an overview of the theoretical background of the Brazilian test, both in quasi-static and dynamic regimes, is given first. Two fundamental assumptions that underpin the formulation of the relationship between the externally applied loads and the developed tensile stress are highlighted, namely 1) linear elastic response of material, and 2) attainment of a static equilibrium state. As a matter of fact, when it comes to dynamic splitting test of a concrete specimen, neither of the above conditions can be strictly satisfied, this prompts the need for careful scrutinization of the stress conditions in a splitting test specimen under high rate loading. A numerical model is then presented which allows systematic numerical experiments to be performed to simulate the physical tests in a Brazilian test

configuration. Following a general observation of the variation of the stress conditions with increase of the loading rate on an elastic specimen, nonlinear analyses will be presented and discussed. Results will show that above a certain critical strain rate, significant dynamic structural effect tends to be involved, consequently complication arises in the stress distribution and the tensile strength can no longer be well represented in such a test. Results from the numerical analysis without considering the material DIF tend to show little change in the achieved dynamic tensile strength. The results thus indicate that the experimentally observed large DIF in tension cannot be a "structural effect" as in the case of dynamic compression.

5.2 Theoretical background of dynamic splitting-tensile test

5.2.1 Static Brazilian test

In classical Brazilian tension test, as schematically shown in Fig. 5-1, a circular disk of the material specimen is placed between two platens which are loaded in compression. This produces a nearly uniform tensile stress distribution normal to the loaded (vertical) diametric plane, leading to the failure of the disk by splitting.

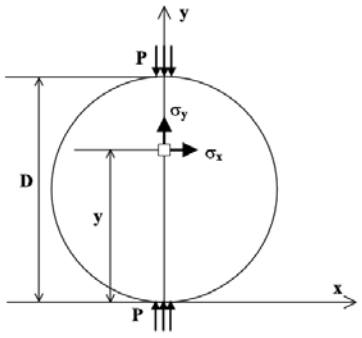

Figure 5-1: Arrangement of quasi-static Brazilian test.

The stress distribution within the specimen can be derived from the elastic theory (Frocht, 1948). Along the vertical diametric plane, the stress in x and y directions can be expressed as:

$$\sigma_x = \frac{2P}{\pi LD}[1-(\frac{2b}{D})^2] \tag{5.1}$$

$$\sigma_y = \frac{2P}{\pi LD}\left[\frac{D^2}{y(D-y)} - 1\right] \tag{5.2}$$

where P is the compression force, L is the thickness (length) of the plate and b is the contact width between specimen and anvils. Along the horizontal diametric plane, tensile stress rapidly decreases from a peak level as a function of distance x from the centre of the disk:

$$\sigma_y = \frac{2P}{\pi LD}\left[\frac{D^2 - 4x^2}{D^2 + 4x^2}\right]^2 \tag{5.3}$$

Thus, Eq. (5.1) is only valid within a narrow strip along the loading direction. However, right under the loading point a high compressive stress could be caused by the load P. In actual test, a pair of bearing strips, such as plywood, is usually placed between the disk specimen and the loading apparatus. The recommended width for the bearing strips is 1-12th of the diameter of the disk (Neville, 1995).

5.2.2 SHPB based dynamic splitting test

Eq. 5.1 can be used to calculate the static splitting strength of concrete. For dynamic loading, the SHPB device as depicted in Fig. 5.2 is commonly used by researchers to test the splitting strength under high strain rate. Unlike in quasi-static tests where the applied loads are directly measured from the loading apparatus, in the SHPB tests the loads on each end of the specimen are inferred from the stresses (strains) measured from the incident and transmitter bars, as:

$$P_1 = AE(\varepsilon_i + \varepsilon_r) \tag{5.4}$$

$$P_2 = AE\varepsilon_t \tag{5.5}$$

where A and E are cross section area and Young's modulus of the pressure bars, ε_i, ε_r and ε_t are incident strain, reflected strain and transmitted strain measured from the strain gauge attached on the pressure bars.

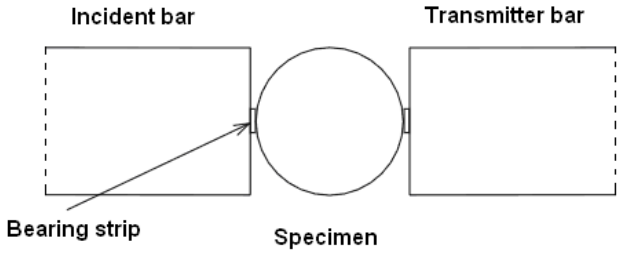

Figure 5-2: Schematic of SHPB splitting Brazilian test (after Hughes et al. (1993))

Once the end forces are determined, their average can be used to compute the dynamic tensile strength using Eq. 5.1. The corresponding dynamic tensile strain rate can be determined indirectly from the tensile stress history. Ross (1998) suggested the following equation to calculate the average strain rate:

$$\dot{\varepsilon}_{td} = \frac{\Delta\sigma_{td}}{E_s(\Delta t)} \tag{5.6}$$

where $\Delta\sigma_t$ is the change of tensile stress, E_s is Young's modulus of the specimen, and Δt is the duration from starting of loading until peak strength.

5.2.3 Validation of stress equilibrium

As mentioned above, the calculation of the dynamic tensile strength from a SHPB splitting test is based on the same formula as established in a static condition and assuming elastic response. However, the validity of extending the static formulation into the dynamic regime is not straightforward.

A number of researches have been conducted in attempt to test the dynamic tensile strength of rock or ceramic materials using the SHPB splitting apparatus. Rodriguez et al. (1994) and Gomez et al. (2001) investigated the time histories of the tensile stress by means of photoelastic measurement. Their results showed that the tensile stress along the loading diameter reaches equilibrium quickly and remains at equilibrium before fracture. The FEM simulation by Rodriguez et al. (1994) supported the above experimental observation. Wang et al. (2009) also conducted numerical simulation to examine the condition of dynamic splitting test, and their results indicate that the stress distributions within the specimen are approximately

symmetrical and a state of stress uniformity can be reached for strain rates up to $26.7s^{-1}$.

Similar tests have been conducted in determining the dynamic strength of concrete, which is also a quasi-brittle material but has rather lower strength. Ross (1998) reported tensile tests of concrete with strain rates in the range of 0.1~100 s^{-1}. The tensile stress is deemed to be constant over approximately 80% of the diameter (Fig. 4). Finite element analysis of concrete tensile splitting tests by Tedesco et al. (1989) and Hughes et al. (1993) verified that a reasonable uniformity can be achieved up to a strain rate about $15s^{-1}$.

More recently numerical simulation by Zhou and Hao (2008) shows that with an incident loading that has a shorter rising time than pulse generated from real experiments, the tensile stress distribution can reach the equilibrium state at relatively low strain rate of $0.4s^{-1}$ and $4s^{-1}$; however, the stress can never reach a equilibrium for a strain rate of order of $40s^{-1}$.

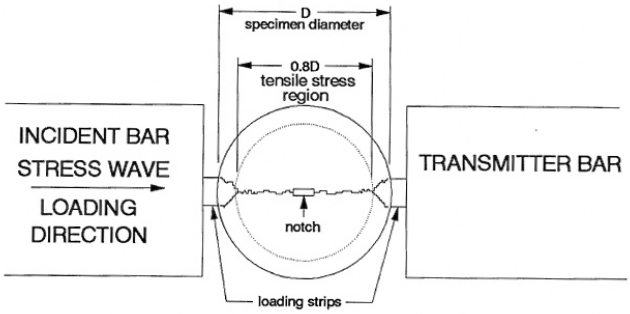

Figure 5-3: Schematic setting of splitting with SHPB (after Ross 1998)

Regarding the computation of tensile stress, different approaches have been suggested for determining P in Eq. 5-1. A common way is to use the transmitted pulse P_2 as P (Tedesco and Ross, 1998; Ruiz et al., 2000). An alternative way is using the average of P_1 and P_2 (Wang et al., 2009). If the stress equilibrium is indeed reached, these two methods would yield identical outcome. However, further investigation by Wang et al. (2009) showed that the stress magnitudes measured from the two ends may be equal but time non-uniformity (delay) cannot be neglected. A time shift method was proposed to rectify this non-uniformity.

5.2.4 Strain rate measurement

A conventional method to determine the strain rate in a splitting experiment is based on Eq. 5-6). However, there is certain ambiguity in the choice of the time interval and the increment in the tensile stress. Ross (1998) suggested using the intermediate segment for the calculation of the tensile strain rate (somewhat a “tangent” strain rate, Fig. 5-4). Ruiz et al. (2000) used the transmitted pulse to calculate the maximum tensile stress and the entire ascending time period to reach the peak stress is considered (somewhat a “secant” strain rate). Since the strain rate in the specimen is not constant during loading, there is a certain degree of uncertainty in the choice of a “representative” strain rate to be associated with a particular measured dynamic tensile strength, and this would contribute in the scatter of the DIF plots from different experimental sources.

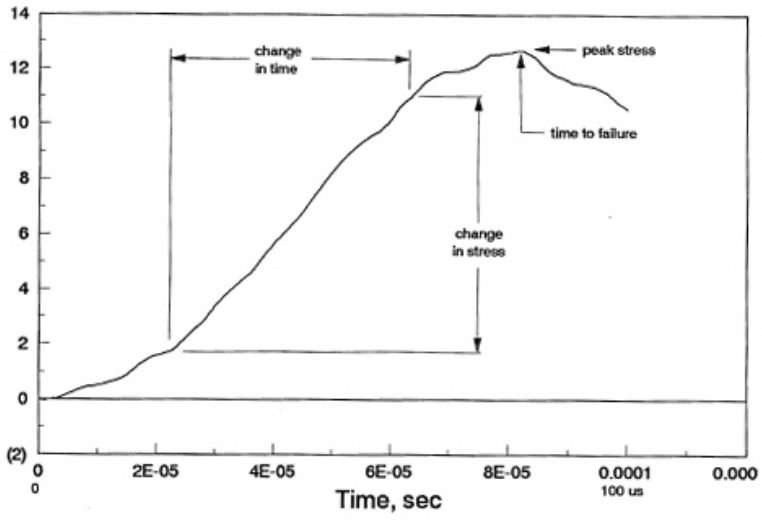

Figure 5-4: Illustration of calculation of strain rate (after Ross, 1998)

Thus far the validation of Brazilian test for high strain rate tension remains inconclusive. Studies tend to show that under a low strain rate, a uniform tensile stress state can be built up; however, quantitative data is lacked with regard to the limit strain rate beyond which the splitting test method will become problematic. In what follows we shall examine the stress state under dynamic splitting loading, starting from an idealised linear elastic situation for which Eq. 5.1 is derived. We shall then move on using a nonlinear specimen model as will be presented in Section 5.4 and 5.5.

5.3 FE model setup for dynamic splitting simulation

5.3.1 FE model and boundary condition

The concrete specimen is modelled as a 3D concrete disk. The FE model and the imposed boundary condition are shown in Fig. 5-5. The bearing strip is chosen to be 1-12th of the diameter of the specimen, as suggested in Hughes et al. (1993).

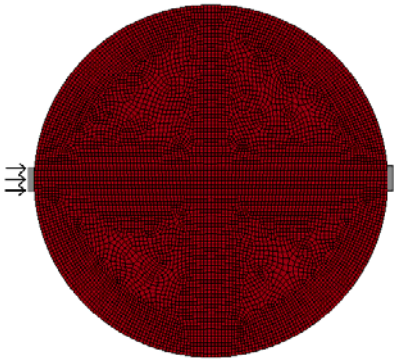

Figure 5-5: General model setting and loading conditions for dynamic splitting test

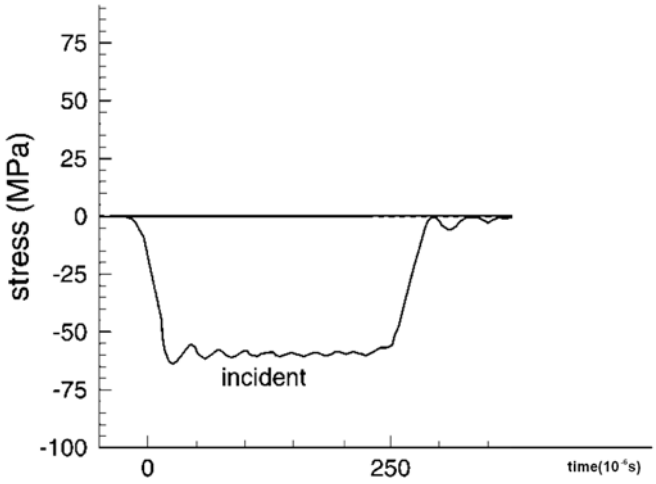

Figure 5-6: Realistic incident stress pulse from Hughes et al. (1993)

A collection of realistic loading data observed from real SHPB based splitting tests was given by Ruiz et al. (2000). A typical shape of the incident pulse is shown in Fig. 5-6. The rising time of the incident pulse is found to be in the range of 48-85 microseconds according to Hughes and Tedesco's experiments. In the modelling of the splitting disk, in order to maintain a constant strain rate during loading (after a gradual rise period), it is convenient to apply a velocity boundary on the incident

surface rather than using a stress input. The velocity can be calculated from the stress by (Nicolas 1990):

$$v = \frac{\sigma_i}{\rho c} \tag{5.7}$$

where ρ is the density and c is the wave speed of the incident bar, σ is the incident stress which can be calculated from strain gauge readings. According to Eq. 5-7, a rectangular stress pulse results in a velocity load with a similar shape. In the numerical simulation herein, a velocity boundary with a gradual rise-time is applied on the loading face, while the end face is fixed. Similar simplified loading conditions have also been used in the numerical model Ruiz et al. (2000) and Zhou and Hao (2008). The impulse rising time is chosen to be 0.05ms. The peak velocity can be adjusted to achieve different strain rate conditions.

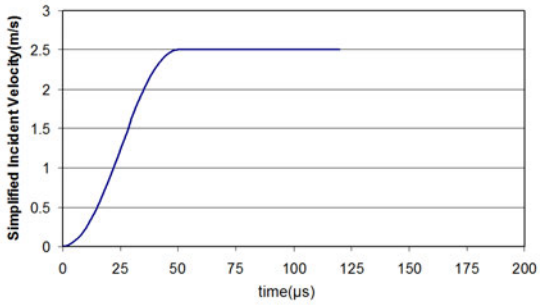

Figure 5-7: Velocity load applied at the incident boundary

It should be noted that although a longer rise time is favourable in terms of facilitating a uniform stress condition, it also limits the capacity to achieve higher strain rates as failure strain could be reached before the target (constant phase) strain rate is attained. On the other hand, attempting to achieve a higher strain rate by reducing artificially the rise time, to the extreme using a step rise, could promote complications in the stress condition and amplified local effect, for example compressive failure in the vicinity of the loading strip. In the numerical investigation of Dong et al. (2006) and Zhou and Hao (2008), a short-rise or a step load was explored; however the failure modes, as shown in Fig. 5-8 and 5-9, deviate significantly from a desirable splitting condition, rendering interpretation of the results from the measured splitting force to the tensile stress to be questionable.

Figure 5-8: Failure process of sample at t=0.015ms, 0.018ms and 0.028ms after Dong et al. (2006).

Figure 5-9: Failure process of sample at t=0.012ms, 0.016ms and 0.03ms after Zhou and Hao (2008a).

Fig. 5-10 and 5-11 further illustrate the influences of varying the loading rise-time on the responses of splitting tension, using the current numerical simulation with the K&C concrete model. The target loading velocity is set at 12.5m/s which is equivalent to approximately a tensile strain rate of $50s^{-1}$. From Fig. 5-10 the differences in the achieved splitting force as the rise-time decreases from 0.05 ms to 0.005ms can be clearly observed. Actually a peak force of 4000 N (not shown) occurs if the target velocity is applied in a step manner (zero rise-time). The damage patterns shown in Fig. 5-11 echo the above observation in the dynamic splitting forces. It can be found that the specimen shows significant local impact damage if the rise-time is less than 0.02ms. When the loading rise-time increases to the level of 0.04ms, a splitting damage pattern can be observed.

Summarising the above on the effects of the loading rise time, it can be understood that an adequate choice of the rise time needs to balance the need to maintain an appropriate splitting condition (favouring a longer rise time) and the need to achieve a target high strain rate (favouring a shorter rise time). This will be looked upon again later in association with the discussion about the strain rate limit in a dynamic splitting test.

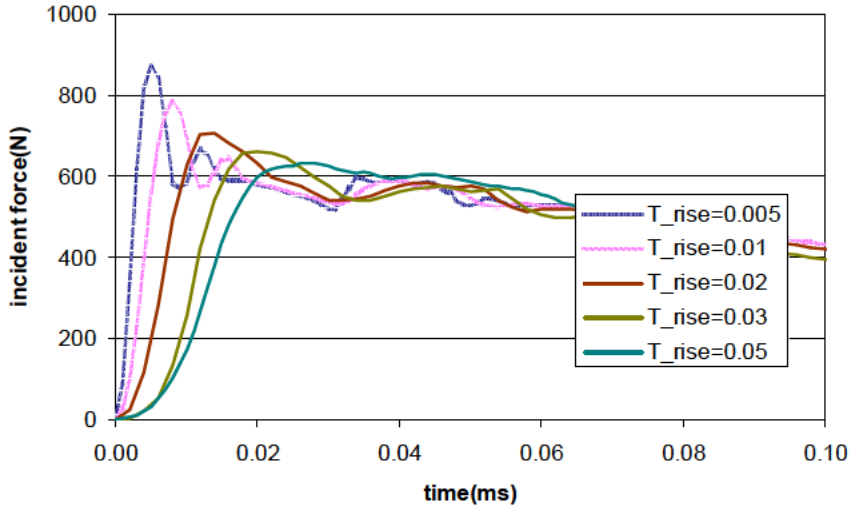

Figure 5-10: Impact of pulse rising time

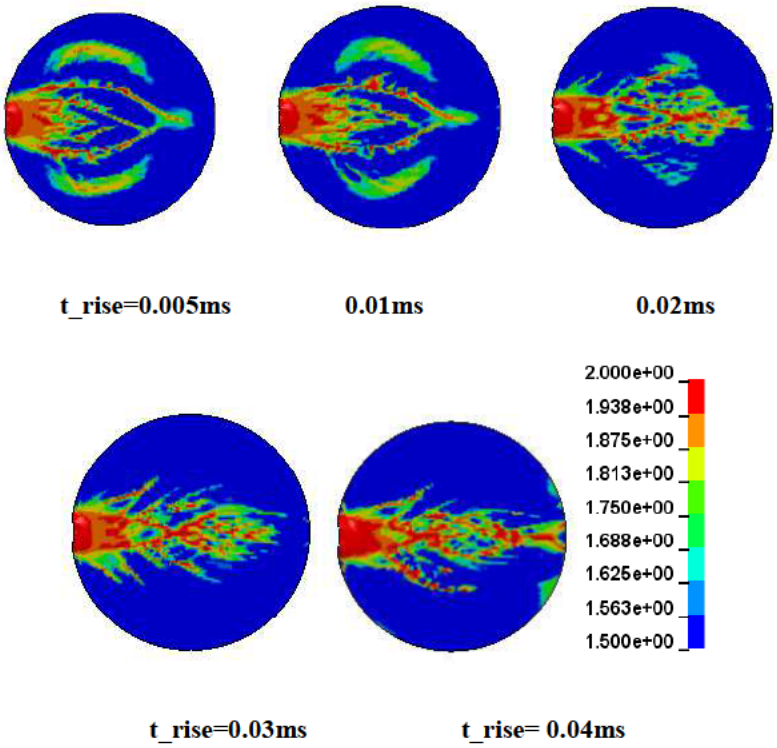

Figure 5-11: Final damage patterns with different load rising times.

5.3.2 Element size convergence test

The nominal mesh size in the numerical model (Fig. 5-5) is 0.5mm. In the nonlinear analysis with the K&C concrete model, the "localization width" is set to 1.5 times of

the element size to reflect the difference of the stress condition in splitting tension from direct tension. As discussed in Chapter 3 Section 3.2.2, the localisation width should generally be the same as the nominal element width in the case of direct tension in order for the mesh-objective treatment of the smeared crack model to achieve its intended mesh regularisation effect. It should also be noted, however, that the localisation width in the model will mainly affect the detailed behaviour in the softening phase of the response, and does not affect sensibly the development leading to the dynamic strength which is the primary interest in the current study.

A mesh convergence study is carried out on a lower strain rate ($1s^{-1}$) case with mesh grid size being 2mm, 1mm, 0.5mm and 0.3mm, respectively. The results of the boundary forces are shown in Fig. 5-14. It can be observed that results with element size of 0.5mm and 0.5mm generally converge for the entire loading history. A comparison of the tensile failure process is shown in Fig. 5-15. The damage patterns with element of 0.5mm and 1mm resemble well.

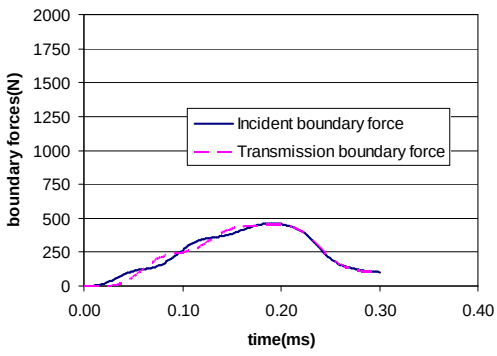

Element size=2mm

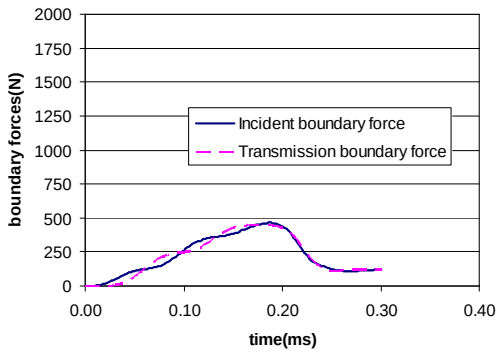

Element size=1mm

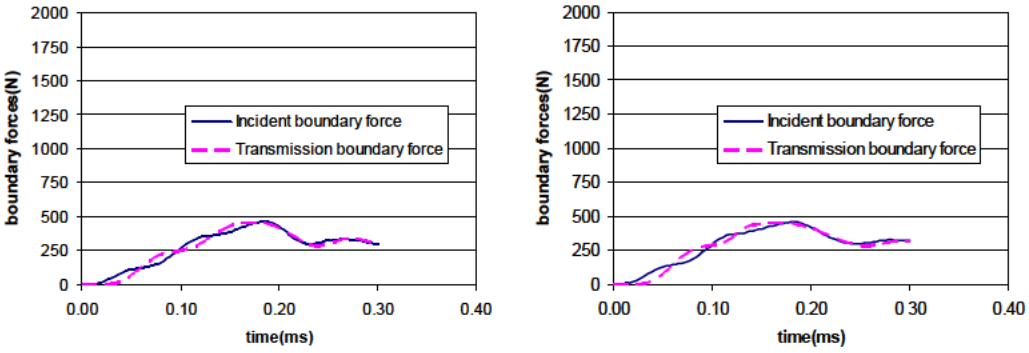

Element size=0.5mm **Element size=0.3mm**

Figure 5-14: Element size convergence test

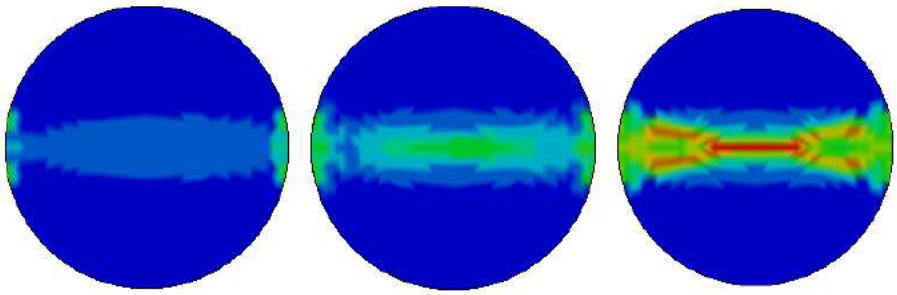

t=0.15ms **t=0.175ms** **t=0.22ms**

a) Mesh size=2mm

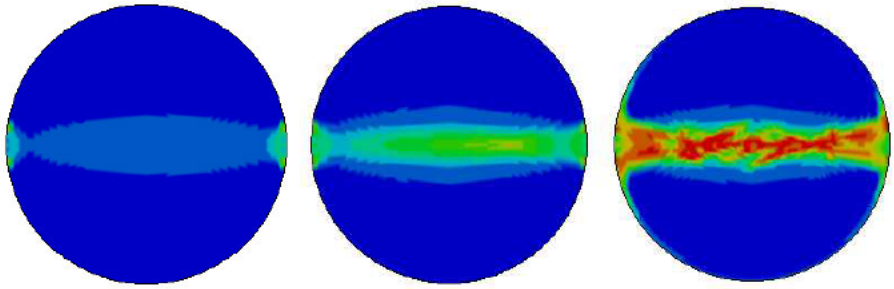

t=0.15ms **t=0.175ms** **t=0.22ms**

b) Mesh size=1mm

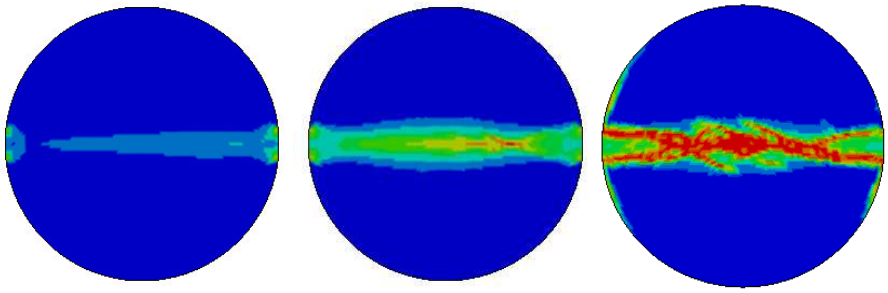

t=0.15ms **t=0.175ms** **t=0.22ms**

c) Mesh size=0.5mm

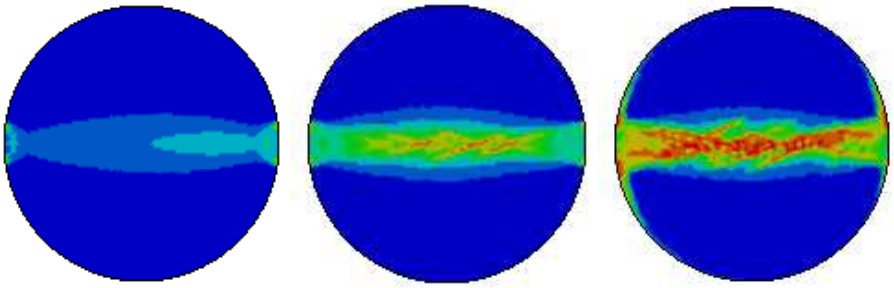

t=0.15ms **t=0.175ms** **t=0.22ms**

d) Mesh size=0.3mm

Figure 5-15: Comparision of tensile damage patterns from different mesh sizes

5.4 Numerical results with elastic model and discussion

An analysis with elastic material is first analyzed as a benchmark to examine the development and distribution of stress in dynamic splitting testing. In the elastic model, the elastic material properties are set to be the same as those of concrete in the elastic phase. The development of a uniform tensile stress distribution before a limit failure strength is reached would be essential for the validity of a splitting tension test, and this may be examined rather conveniently using an elastic model in a dynamic splitting tension configuration.

5.4.1 Lower strain rate ($1s^{-1}$)

The situation with a lower strain rate of $1s^{-1}$ is first analysed. This corresponds to a loading velocity of $0.25m/s^{-1}$ on the incident end in the splitting simulation. The boundary forces are shown in Fig. 5-16. It can be seen that the incident force and transmission force develop almost simultaneously. Small fluctuations in the boundary force history indicate that the stress within the specimen builds up as the stress wave reverberates between the two ends.

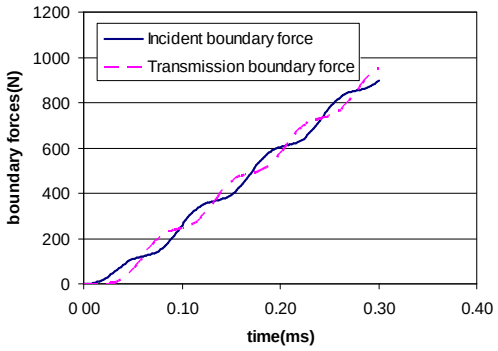

Figure 5-16: Incident and transmission boundary forces, strain rate $1s^{-1}$

To demonstrate the distribution of tensile stress at different locations along the loading diametric direction, six locations are selected to show the Y-stress as shown in Fig. 5-17. From the stress time histories it can be clearly observed that, apart from points 1 and 6, the stresses in the middle part (points 2 to 5) develop almost uniformly. The relative lower Y-stress at point 1 and 6 is deemed to be caused by the complicated stress redistribution near the end area.

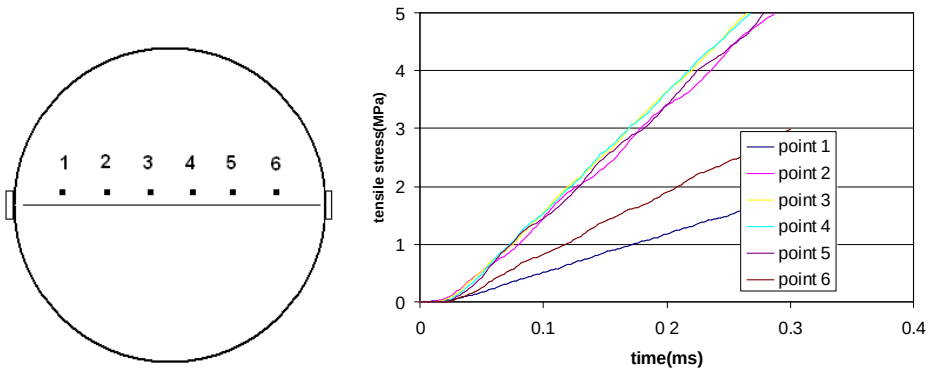

Figure 5-17: Representative locations and tensile stress time histories

Fig. 5-18 shows the distributions of the Y-stress at different loading stages. From Fig. 5-16, we have already observed that the formation of uniform Y-stress is reached via wave reverberations between the two loading ends. The profile of Y-stresses in Fig. 5-18 reaffirms that the uniform Y-stress has been reached from t = 0.1 ms onwards.

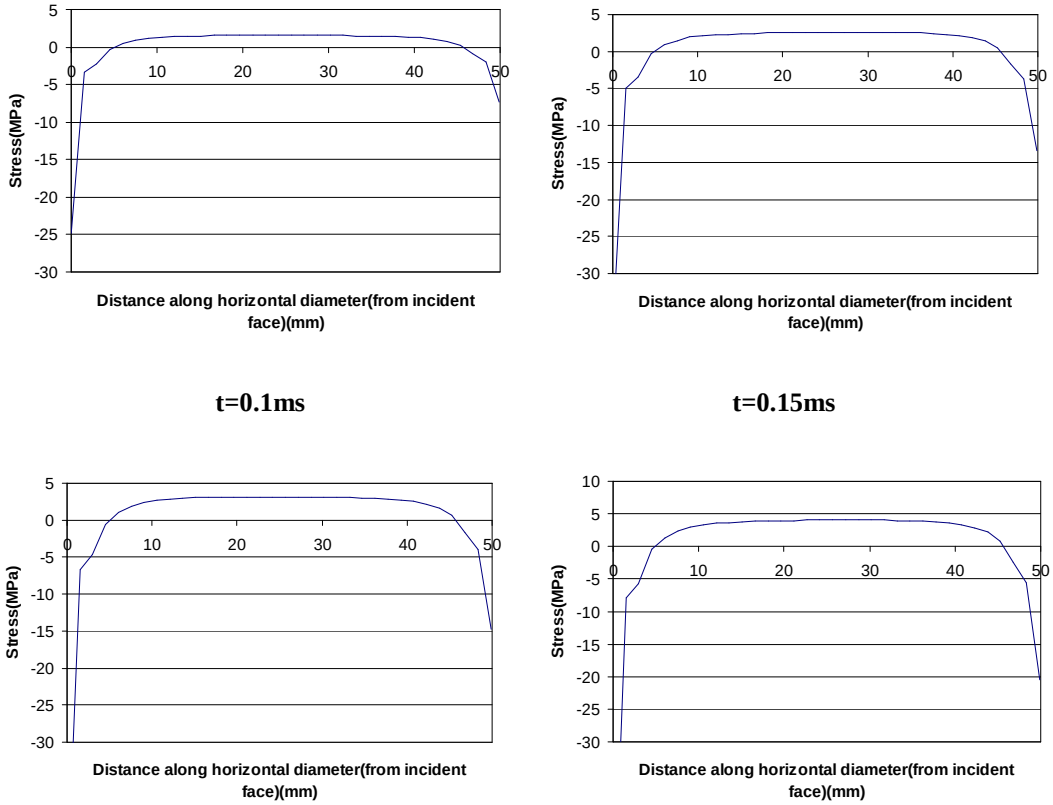

Figure 5-18: Tensile stress profile using elastic material

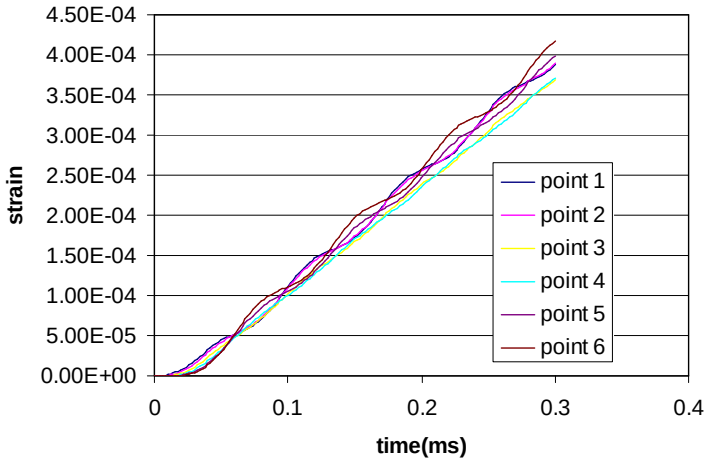

Figure 5-19: Observed tensile strain at different locations

Fig. 5-19 shows the strain history at the selected locations. Strain and strain rate uniformity can be clearly observed for this loading rate. The strain rate calculated from the slope is around $1.2s^{-1}$, which is quite close to the value calculated from the formula 5.6 ($1.05s^{-1}$ based on the data in Fig. 5-17).

Fig. 5-20 shows the contour of tensile Y-stress. The uniformity in the stress distribution is achieved from t = 0.1 ms and the effective tensile region is very close to 0.8D as suggested from Ross (1998).

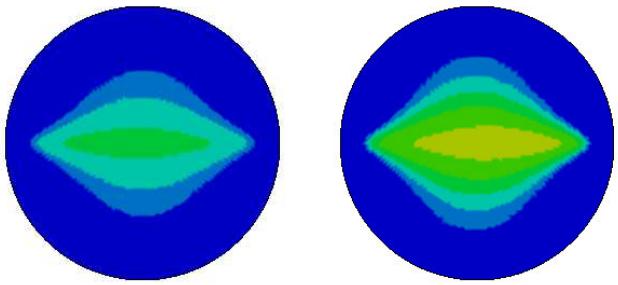

t=0.1ms **t=0.15ms**

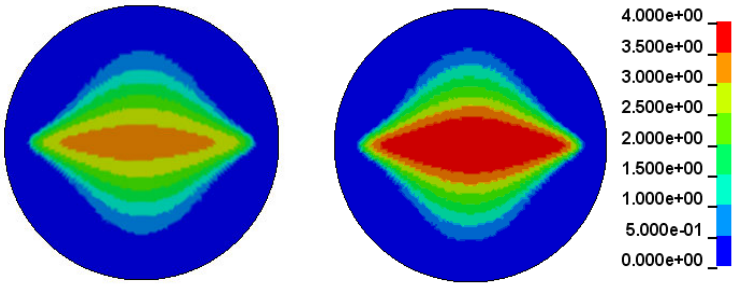

t=0.175ms **t=0.22ms**

Figure 5-20: Tensile stress profile using elastic material

5.4.2 Medium strain rate ($10s^{-1}$)

A medium strain rate of $10s^{-1}$ is simulated with a boundary velocity of 2.5m/s. The boundary force histories in Fig. 5-21 show marked differences in the incident and transmission forces before and after the velocity rise to its constant value at t=0.05ms. The force histories indicate that there is only one wave reflection during the loading time.

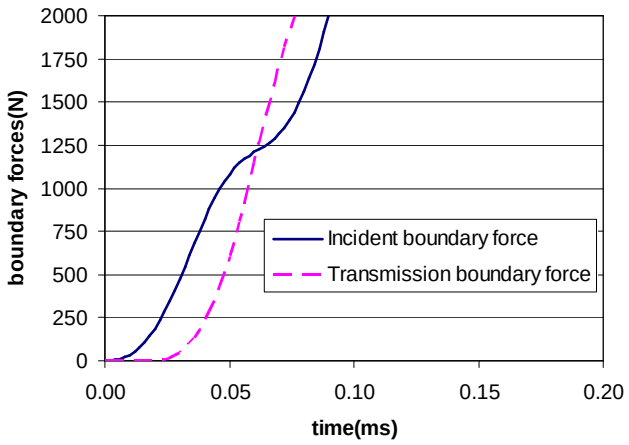

Figure 5-21: Incident and transmission boundary forces

Non-uniformity of tensile stress can be observed from Fig. 5-22 in the loading period. The tensile stress profiles at different times shown in Fig. 5-23 indicate that uniformity can still be achieved eventually, herein from t=0.06ms and the corresponding magnitude of the tensile stress is around 7MPa.

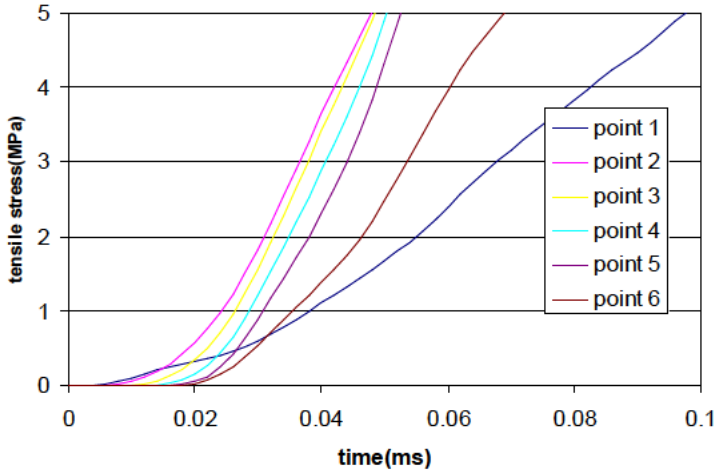

Figure 5-22: Observed tensile stress time histories

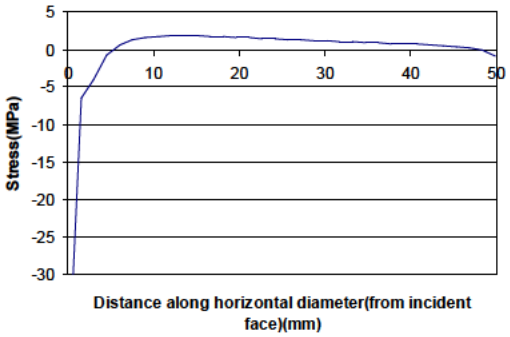

t=0.03ms

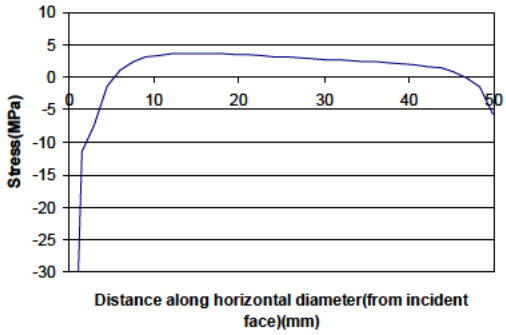

t=0.04ms

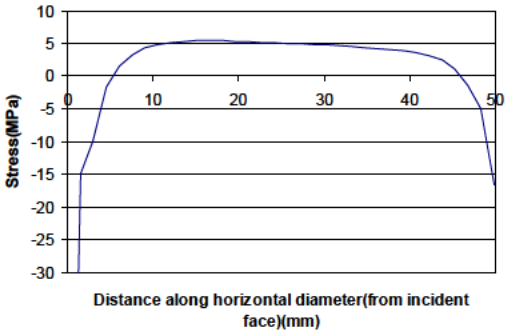

t=0.05ms

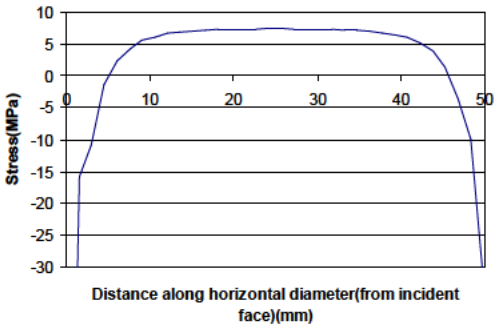

t=0.06ms

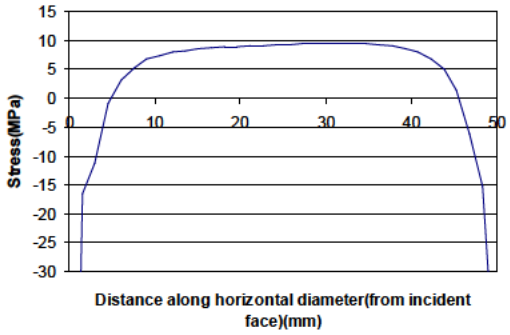

t=0.07ms

Figure 5-23: Tensile stress profile using elastic material

From Fig. 5-27, strain and strain rate uniformity can be clearly observed at this loading rate. Although the strain rates at different locations are slightly different (different slope), a relative uniformity of strain rate is maintained during loading. The average strain rate calculated from the slope is $9.5s^{-1}$, which is close to the target strain rate of $10s^{-1}$.

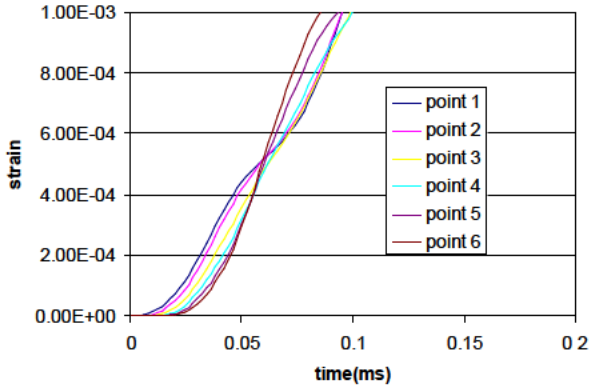

Figure 5-24: Observed tensile strain at different locations

Fig. 5-25 shows the tensile Y-stress contours. These further confirm that a uniform tensile stress distribution is reached from about 0.05 ms.

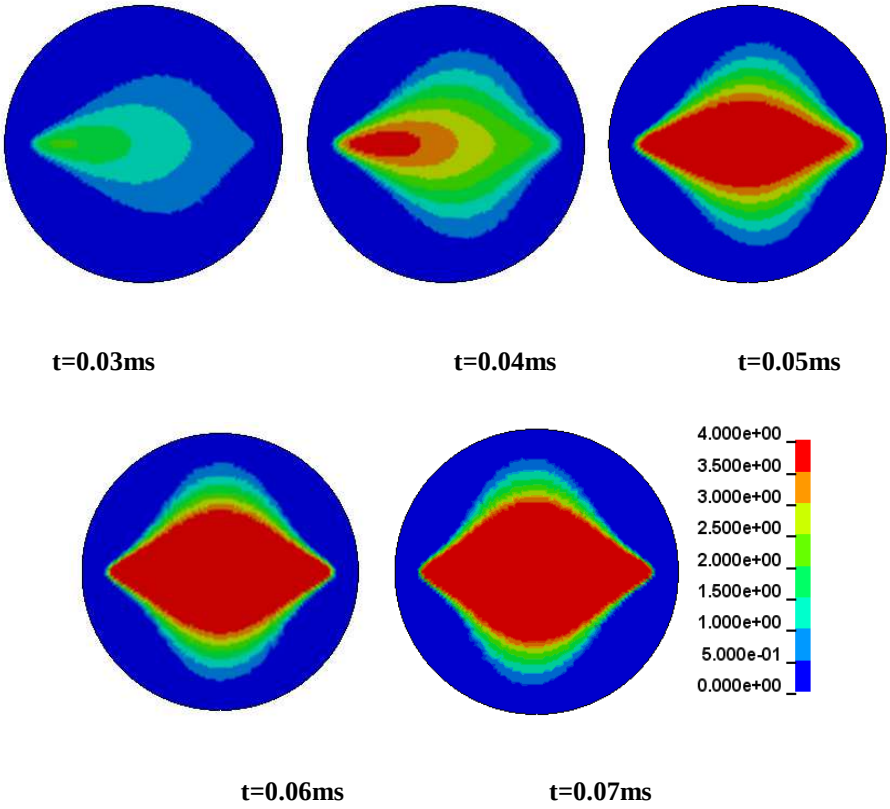

Figure 5-25: Tensile stress profile using elastic material

5.4.3 High strain rate ($50s^{-1}$)

A high strain rate of $50s^{-1}$ is then analysed. Fig. 5-26 shows a clear stress wave propagation phenomenon in the stress build-up period. A significant time delay can be found from the history of the transmission force. The tensile stress histories shown in Fig. 5-27 show significant non-uniformity before t =0.03ms.

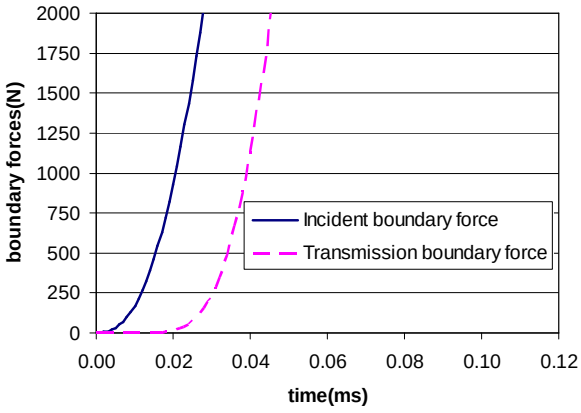

Figure 5-26: Incident and transmission boundary forces

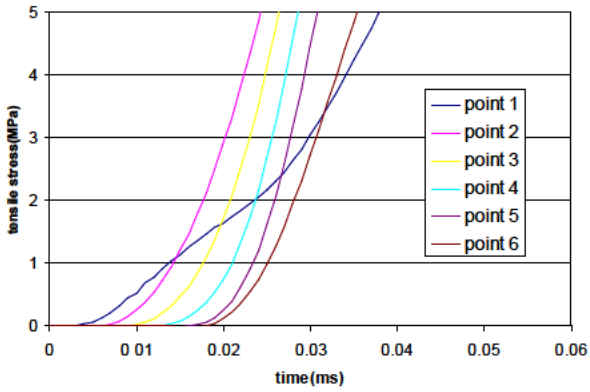

Figure 5-27: Observed tensile stress histories

From Fig. 5-28, the uniformity in the tensile Y-stress is achieved only after t = 0.06ms, at which time the tensile stress has reached about 35MPa, which would be far beyond the tensile strength of concrete even taking a substantial DIF into account. This observation indicates that a stress equilibrium and uniformity is unlikely to be achieved in a concrete specimen before failure at such a strain rate.

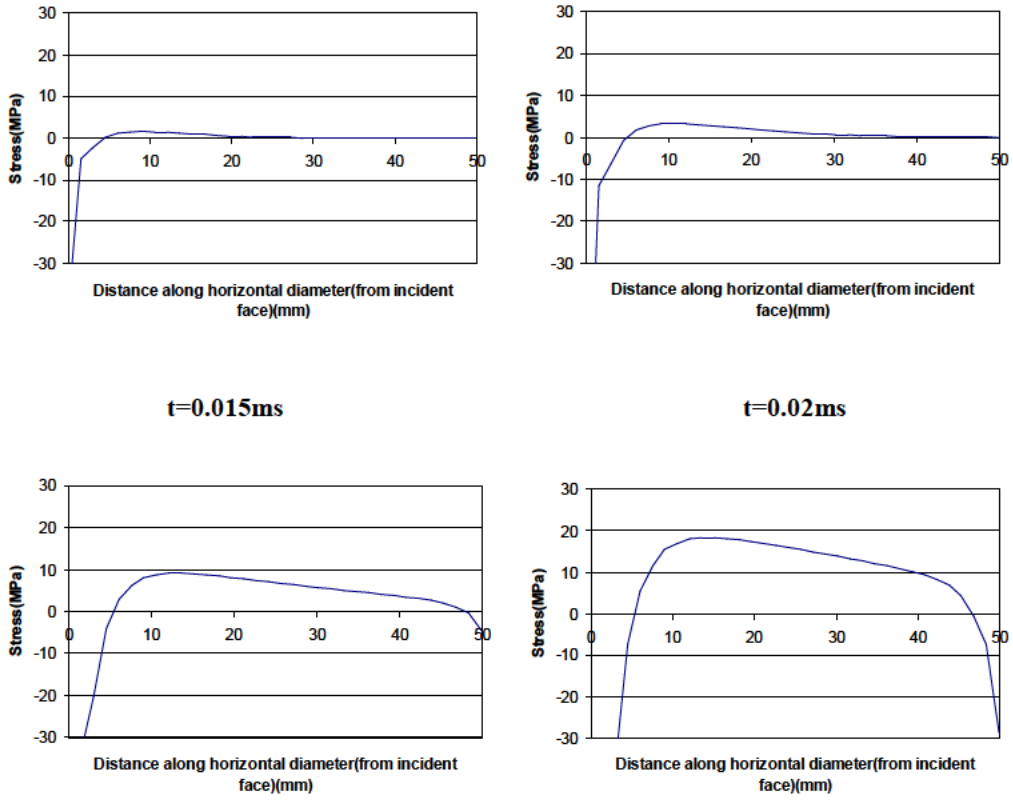

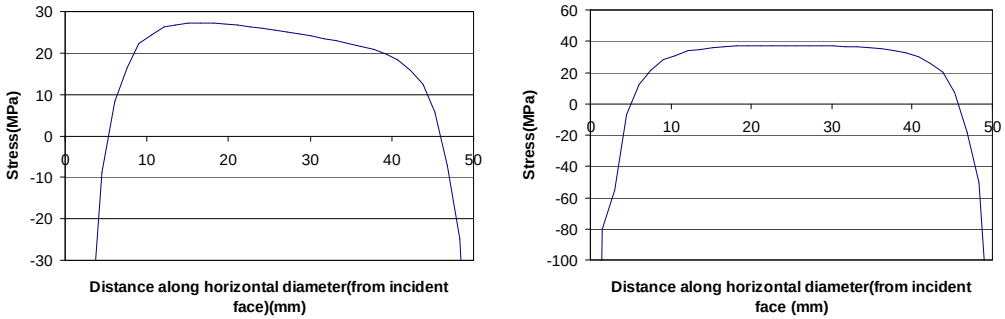

t=0.05ms **t=0.06ms**

Figure 5-28: Tensile stress profile using elastic material ($50s^{-1}$)

5.5 Numerical simulation with concrete material model and discussion

In this section we shall simulate the dynamic splitting test for concrete tensile strength using a more realistic concrete material model, herein the K&C model. We shall first consider no embedded strain rate increase (DIF) at the material model level, so as to observe whether any specimen-wide structural effect, e.g. inertia effect as discussed in Chapter 3 and 4 for compression, would play a significant role. A homogenous FE model as used in the elastic simulation is analysed at corresponding strain rates as considered in Section 5.4. The peak strength in the concrete model is assumed to be 30MP and the corresponding tensile failure strength automatically generated from model settings is 2.9MP.

5.5.1 Lower strain rate ($1s^{-1}$)

The boundary force history in Fig. 5-29 shows that the incident and transmission forces are developed simultaneously as is also found through the elastic model. The tensile stress within the effective tensile region is also uniform as can be seen from Fig. 5-30, despite the development of nonlinear response.

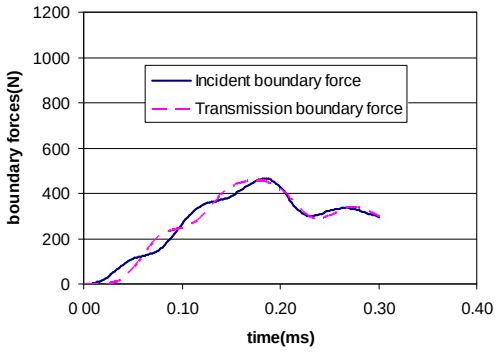

Figure 5-29: Incident and transmission boundary forces

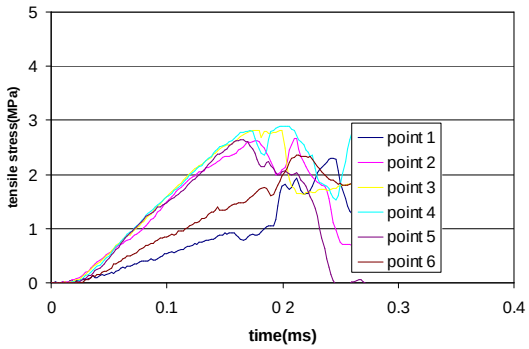

Figure 5-30: Observed tensile stress histories

Fig. 5-31 shows the development of Y-stress at different stages. From Fig. 5-29, it has been found that the peak strength is reached at about t = 0.175ms. In Fig. 5-31, one can observe that the uniformity of Y-stress is also attained, at about t = 0.1 ms, before the concrete reaches the tensile failure strength (about 3 MPa).

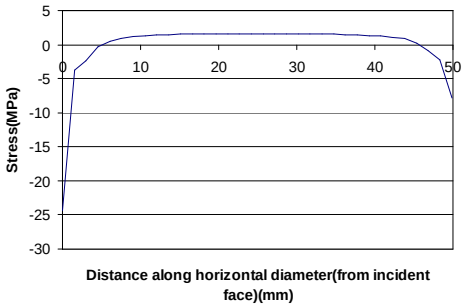

t=0.1ms

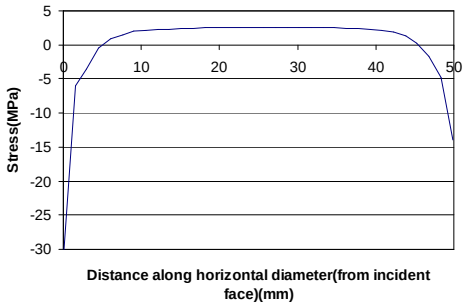

t=0.15ms

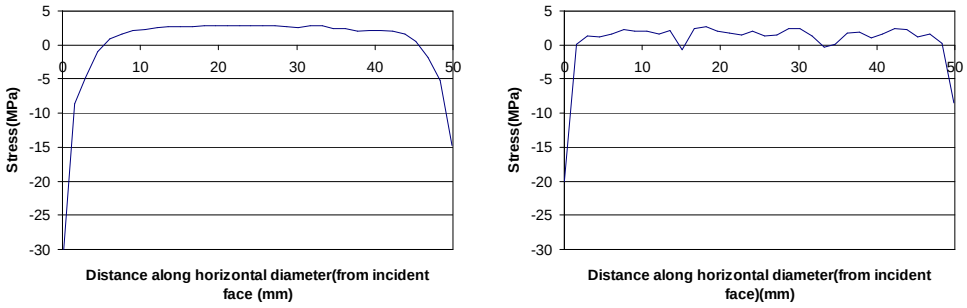

t=0.175ms **t=0.22ms**

Figure 5-31: Tensile stress profile using concrete material

Table 5-1 shows the calculated tensile stresses using Eq. 5.1 and the directly observed tensile stress from the relevant FE elements at different time points. Results from the elastic model are also included for a comparison. In the elastic case, the observed stress agrees with the values computed from Eq. 5.1. In the concrete model case, the observed values agree with the calculated ones before the peak strength is reached (at about t = 0.175ms). Both tensile strengths as extracted from the elements and from Eq. 5.1 do not exhibit any apparent increase from the given static tensile strength, suggesting that there is no sensible structural effect on the development of the dynamic tensile strength, at least at the present strain rate level.

Table 5-1: Comparison of observed and calculated tensile strength ($1s^{-1}$)

time	Elastic model		Concrete model	
	$\frac{2P}{\pi LD}$ (MPa)	Observed (MPa)	$\frac{2P}{\pi LD}$ (MPa)	Observed (MPa)
0.1ms	1.65	1.54	1.69	1.59
0.15ms	2.50	2.60	2.47	2.50
0.175ms	3.33	3.14	2.90	2.80
0.22ms	4.01	4.05	2.05	1.63

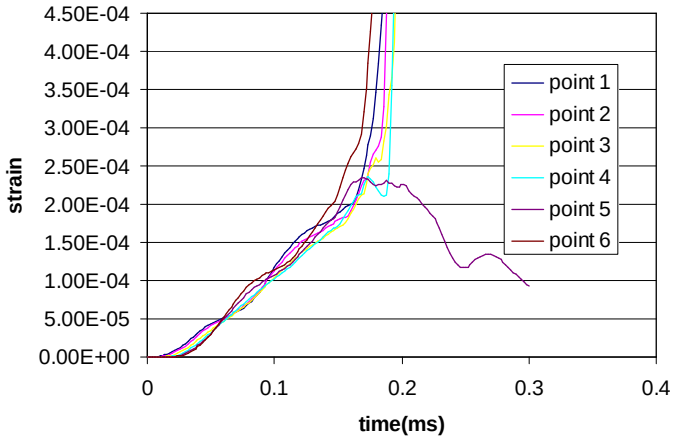

Figure 5-32: Observed tensile strain at different locations

In Fig. 5-32, the strain and strain rate uniformity in the central area along the loading diametric direction can be clearly observed before the peak strength is achieved. The strain rate calculated from the slope is $1.2s^{-1}$, which is also close to the value calculated from Eq. 5.6 ($1.05s^{-1}$ based on the result in Fig. 5-29). The Y-stress

contour in Fig. 5-33 also confirms the above observations. The uniformity in the tensile stress can be observed from about t = 0.1 ms. Fig. 5-34 shows that cracking starts from both ends and a splitting failure pattern is obtained eventually.

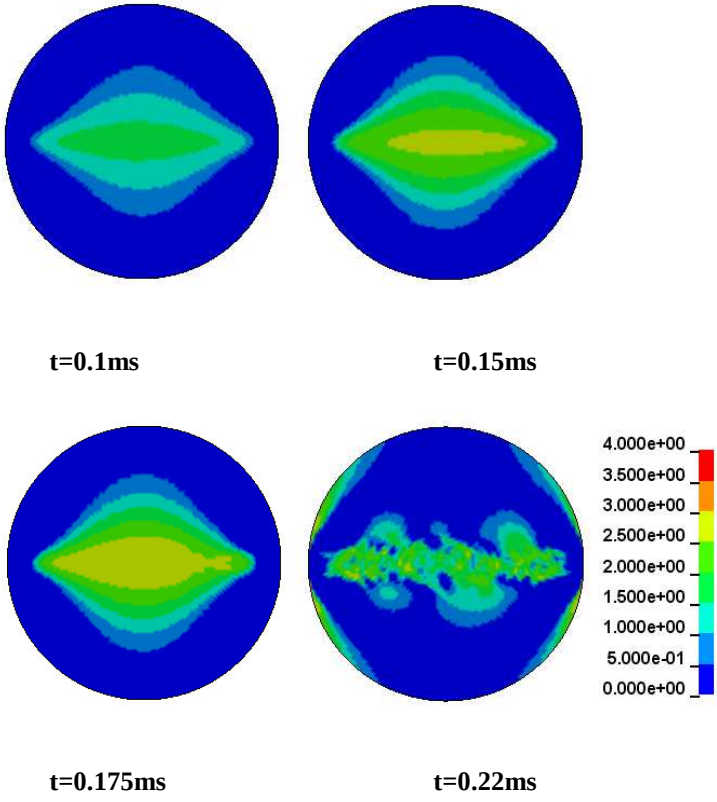

Figure 5-33: Tensile stress profile using concrete material

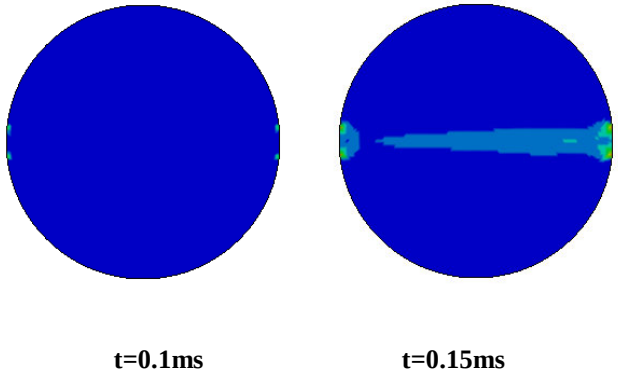

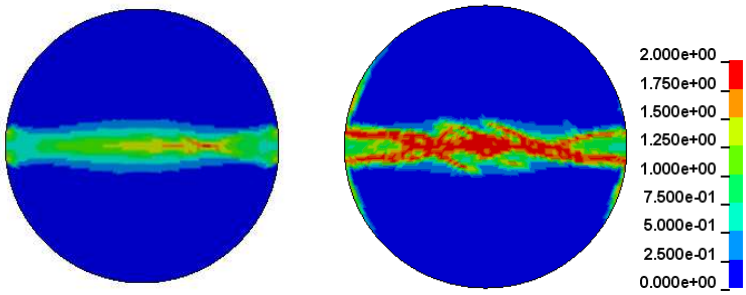

t=0.175ms **t=0.22ms**

Figure 5-34: Plastic damage profile using concrete material

5.5.2 Medium strain rate ($10s^{-1}$)

Under the medium strain rate of $10s^{-1}$, a marked delay in the transmission force as compared to the incident force occurs, as can be seen from Fig. 5-35. This delay in time indicates that using the averaging method to find the splitting force could be problematic. The magnitudes of the forces are found to be on similar, albeit at different times. Form Fig. 5-35, it can also be observed that the peak strength is reached at the loading end at about t=0.04 ms. From Fig. 5-36, the tensile stresses at points 2-5 evolve in a similar pace before the peak strength is reached. From Fig. 5-37 we can observe that a generally uniform tensile stress can be achieved at about t = 0.04ms.

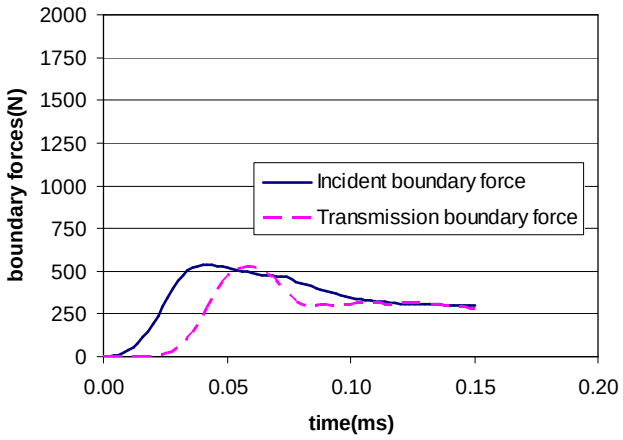

Figure 5-35: Incident and transmission boundary forces

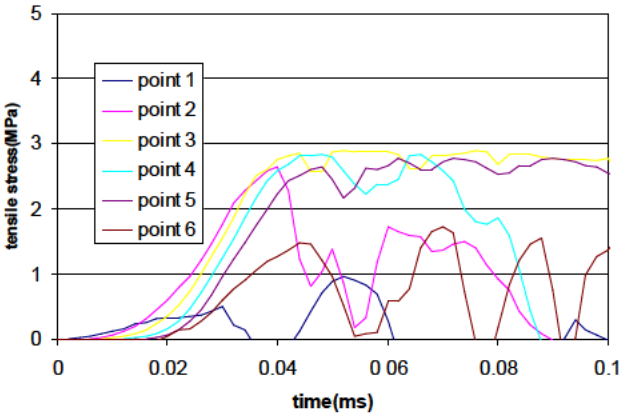

Figure 5-36: Observed tensile stress histories

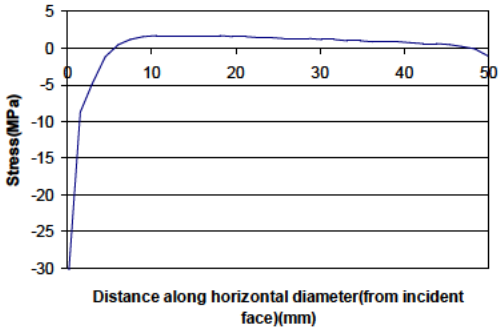

t=0.03ms

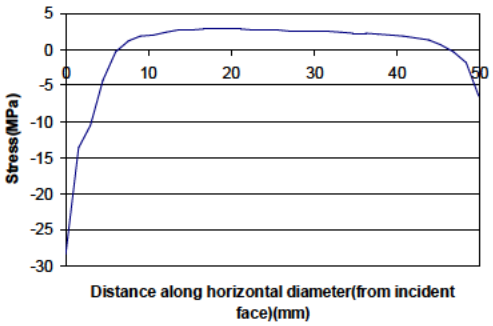

t=0.04ms

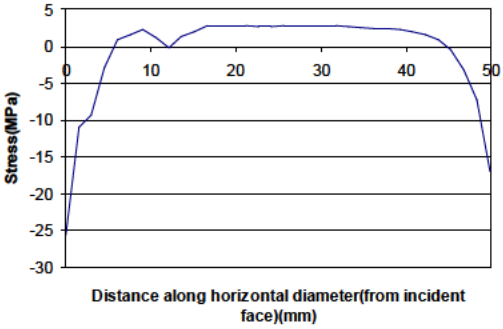

t=0.05ms

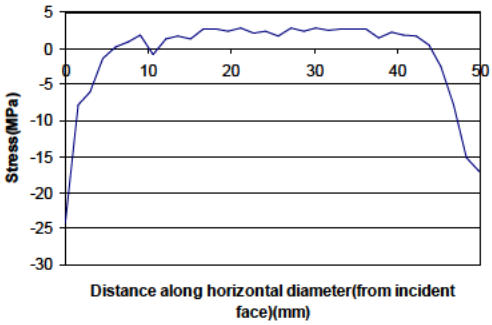

t=0.06ms

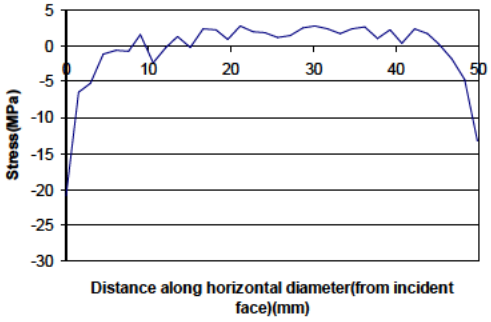

t=0.07ms

Figure 5-37: Tensile stress profile using concrete material

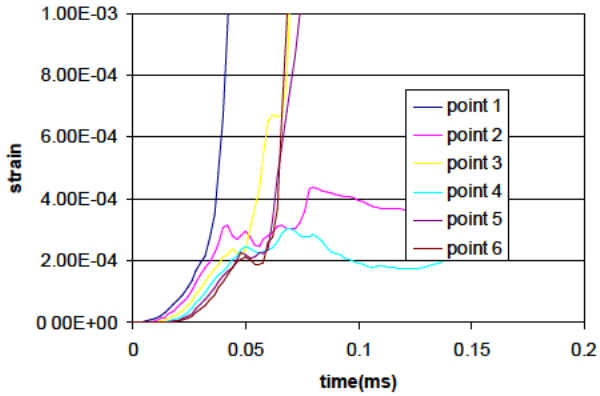

Figure 5-38: Observed tensile strain at different locations

Strain and strain rate uniformity can be observed at this loading rate if we ignore results in first stage (before t=0.02). The strain rates at different locations are very close before failure (different slope).

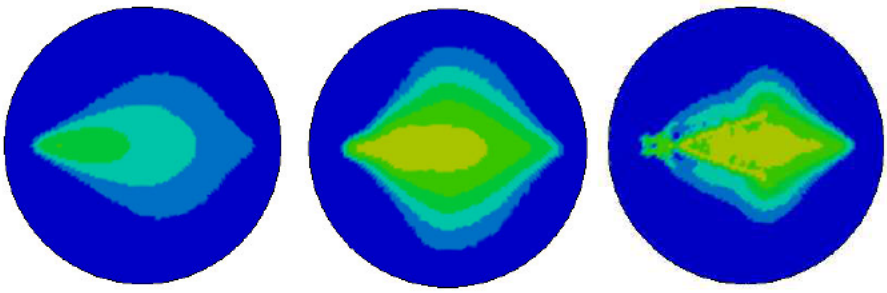

t=0.03ms **t=0.04ms** **t=0.05ms**

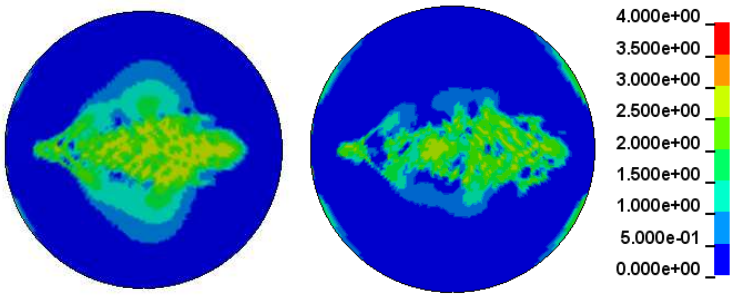

t=0.05ms **t=0.06ms**

Figure 5-39: Tensile stress profile using concrete material

From the tensile contour shown in Fig. 5-39, we can conclude that a rough uniform tensile stress can be achieve at t=0.04ms.

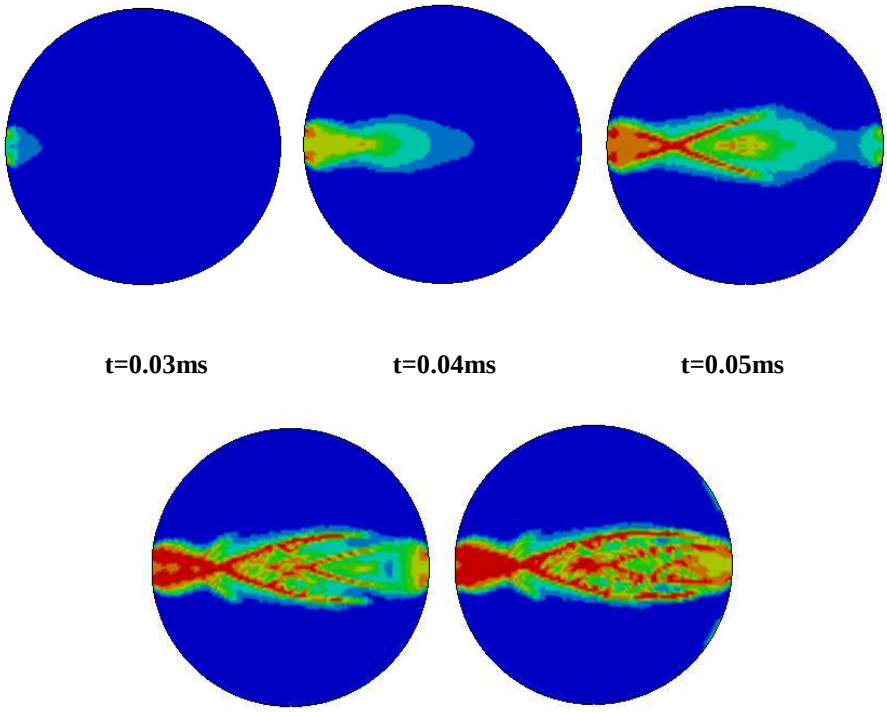

t=0.03ms **t=0.04ms** **t=0.05ms**

t=0.06ms **t=0.07ms**

Figure 5-40: Plastic damage profile using concrete material

Table 5-2 summarises the tensile stress values from the elastic and concrete models, obtained in different ways. The apparent discrepancy of the results from P_1 and P_2 at the early stages is due to the time delay in the development of P_1 and P_2 at the two ends of the specimen, as mentioned before. The maximum observed tensile

strength from the concrete model results remains to be close to the static tensile strength (about 2.75MPa), indicating that there is still no apparent enhancement being generated from any dynamic structural effect.

It should also be noted from that, as can be observed from the stress time histories and the damage contours, local tensile failure actually commences slightly before the target strain rate of $10s^{-1}$ (or constant boundary velocity of 2.5 m/s) is reached, which is given at 0.05 ms (see Fig. 5.4). This means the effective strain rate achieved is the present is slightly lower than the nominal value of $10s^{-1}$.

Table 5-2: Comparison of observed and calculated tensile strength ($10s^{-1}$)

time	Elastic model				Concrete model			
	$\frac{2P}{\pi LD}$ (MPa)			Observed (MPa)	$\frac{2P}{\pi LD}$ (MPa)			Observed (MPa)
	P_1	P_2	$(P_1+ P_2)/2$		P_1	P_2	$(P_1+ P_2)/2$	
0.03ms	3.02	0.32	1.67	1.25	2.81	0.32	1.56	1.33
0.04ms	5.23	1.45	3.34	2.77	3.40	1.46	2.43	2.40
0.05ms	6.90	3.83	5.37	4.51	3.31	**2.98**	3.15	**2.75**
0.06ms	7.69	7.31	7.50	6.54	3.12	**3.36**	3.24	2.14
0.07ms	8.39	10.92	9.66	8.19	2.99	2.80	2.89	1.52

5.5.3 High strain rate ($50s^{-1}$)

The incident and transmission forces evolve at significantly different paces when the target tensile strain rate is raised to $50s^{-1}$, as can be found in Fig. 5-41. Results in Fig. 5-42 to 5-43 show a complicated development path of the tensile stresses almost during the entire course of loading.

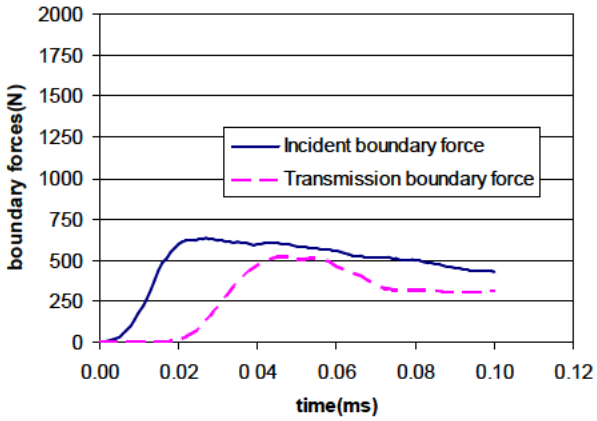

Figure 5-41: Incident and transmission boundary forces

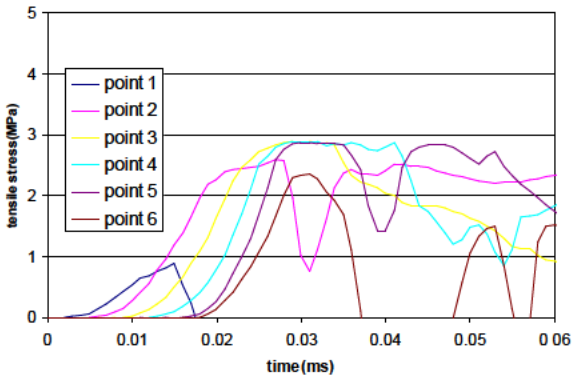

Figure 5-42: Observed tensile stress histories

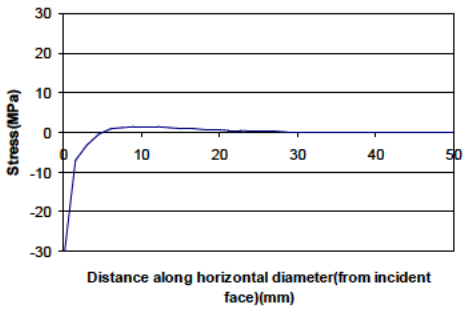

t=0.015ms

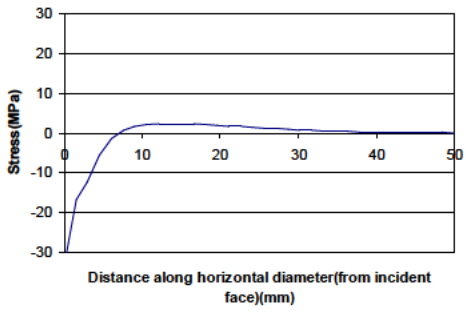

t=0.02ms

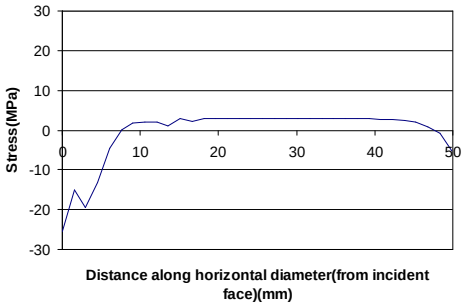

t=0.03ms

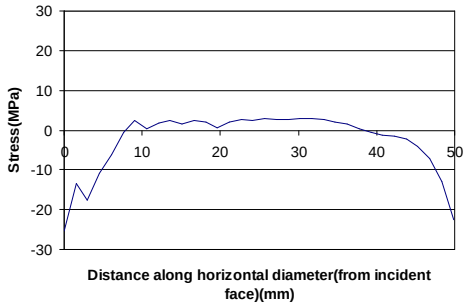

t=0.04ms

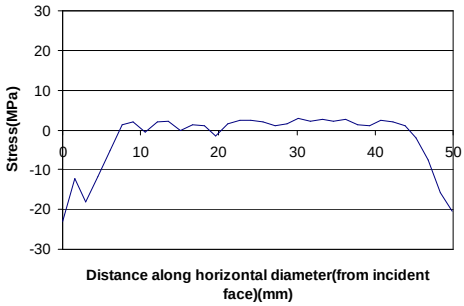

t=0.05ms

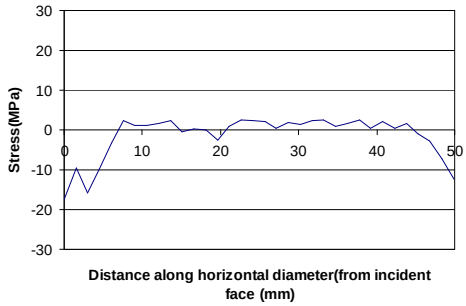

t=0.06ms

Figure 5-43: Tensile stress profile using concrete material

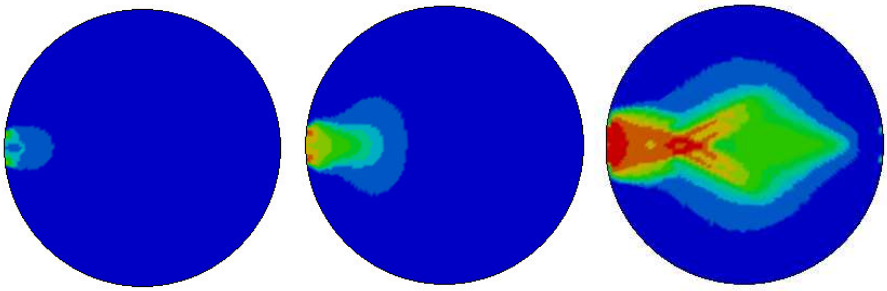

t=0.015ms t=0.02ms t=0.03ms

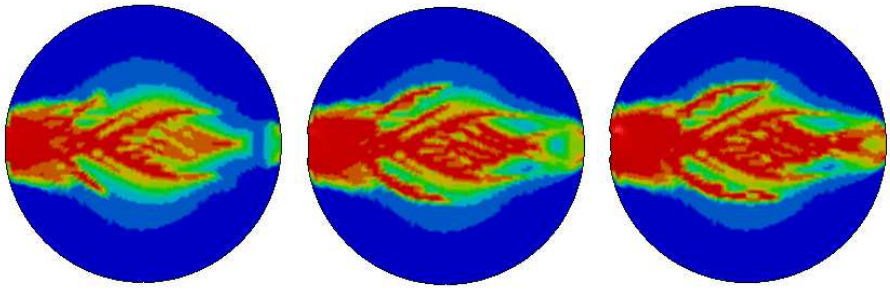

t=0.04ms **t=0.05ms** **t=0.06ms**

Figure 5-44: Plastic damage profile using concrete material

Table 5-3 summarise the tensile stresses. While the discrepancy in the P_1 and P_2 forces further enlarges, as can be expected, the achieved tensile strength from the concrete model simulation remains to be around the level of the static tensile strength, indicating that there is no significant enhancement on the dynamic tensile strength from any structural effect, even at the present high strain rate level.

It is important to note that, as can be observed from the stress time histories and the damage contours, local tensile failure actually commences well before the target strain rate of $50s^{-1}$ (or constant boundary velocity of 12.5m/s) would have been reached at 0.05 ms (see Fig. 5.4). Thus, the effective strain rate achieved in this case is well below the nominal value of $50s^{-1}$, despite that the loading has been given with that strain value as a target. This echoes the discussion mentioned in Section 5.3.1.

Table 5-3: Comparison of observed and calculated tensile strength ($50s^{-1}$)

time	Elastic model				Plastic model			
	$\frac{2P}{\pi LD}$ (MPa)			Observed (MPa)	$\frac{2P}{\pi LD}$ (MPa)			Observed (MPa)
	P_1	P_2	$(P_1+ P_2)/2$		P_1	P_2	$(P_1+ P_2)/2$	
0.02ms	2.93	0.00	1.47	0.49	2.76	0.00	1.38	0.47
0.03ms	5.91	0.08	2.99	1.40	3.81	0.09	1.95	1.19
0.04ms	15.11	1.48	8.30	6.56	3.97	1.38	2.68	2.70
0.05ms	26.08	7.20	16.64	14.53	3.80	2.99	3.39	2.03
0.06ms	34.46	19.14	26.80	23.69	3.73	3.22	3.48	1.52
0.07ms	38.45	36.41	37.43	34.32	3.54	2.95	3.25	1.23

5.6 Nonlinear FE analysis considering material DIF

In section 5.5, analysis has been based on non-DIF material model. The actually achieved dynamic tensile strength (Table 5.1-5.3) shows little increase with the strain rate. This clearly demonstrates that, unlike in dynamic compression as discussed in Chapter 3 and 4, the dynamic structural effect or inertia within a (splitting) tensile specimen does not appear to play a sensible role in promoting an increase in the dynamic tensile strength. In other words, the mechanisms underlying the experimentally observed apparent DIF in tension may only be attributed to micromechanical processes which are not represented in a continuum based FE model. It is therefore reasonable that in such a model, the tensile strength increase should be incorporated as a material description. Similar analyses as in Section 5.5 have be carried out with however an inclusion of the tensile DIF in the concrete material model. This section summarises the main results. The DIF chosen is the one suggested by Malvar and Crawford (1998), as a modified version of the CEB model (CEB, 1993). Fig. 5-45 shows the DIF curve vs. tensile strain rate.

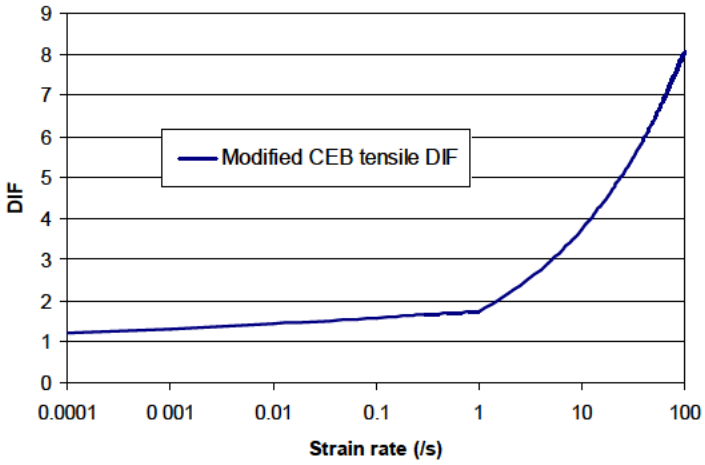

Figure 5-45: DIF incorporated to material model

Fig. 5-46 illustrates the development of the splitting forces on the loading and support ends, for the three different nominal strain rates. Similar to the observations in Section 5.5, the specimen can still nearly achieve a balanced loading condition before failure when the strain rate is up to $10s^{-1}$, but not for higher strain rates such as the "$50s^{-1}$" herein. It can also be observed that the splitting forces apparently

increases with the increase of the loading rate, indicating that the imposed DIF at the material model level is taking effect.

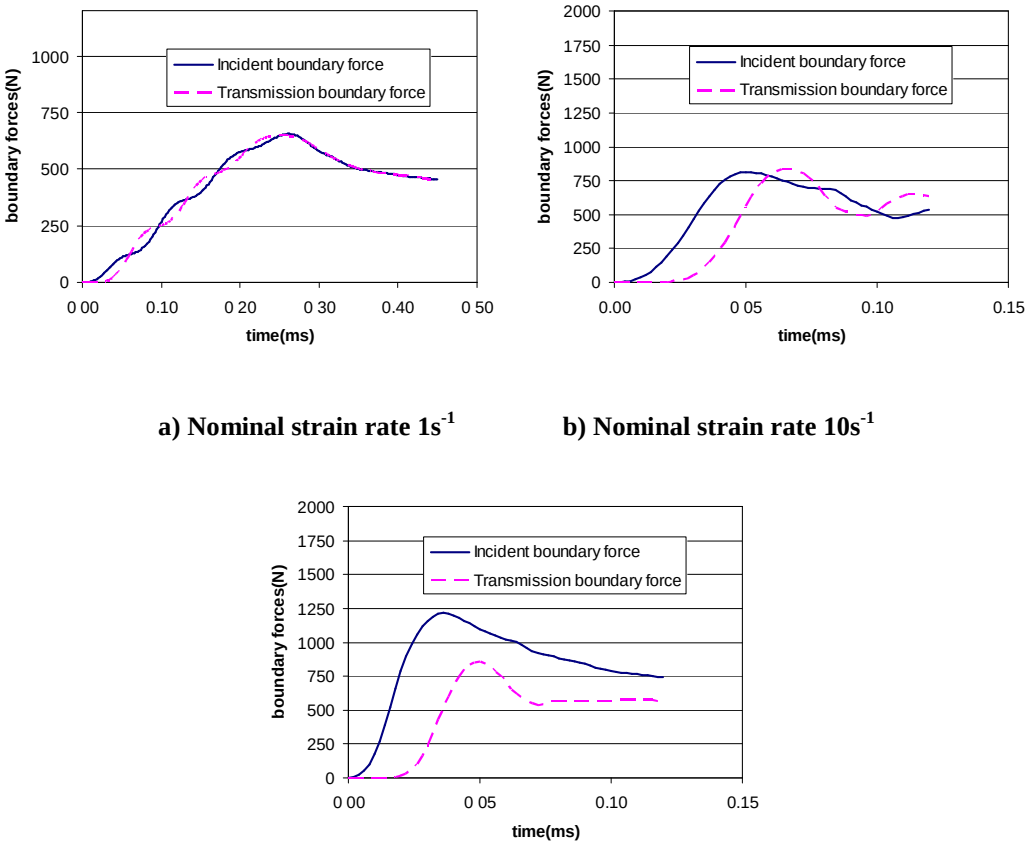

a) Nominal strain rate $1s^{-1}$ **b) Nominal strain rate $10s^{-1}$**

c) Nominal strain rate $50s^{-1}$

Figure 5-46: Incident and transmission boundary forces

The attainment of a relatively uniform tensile stress distribution up to the strain rate of $10s^{-1}$ can also be observed from the time histories of the tensile stresses at the selected locations in the loading diametric direction in Fig. 5-47.

Fig. 5-48 illustrates the development of damage in the specimens under the three different strain rates. Again, it can be observed that a clear splitting failure occurs under $1s^{-1}$ loading. Failure still initiates in a splitting fashion under $10s^{-1}$, but the damage process becomes much more complicated in the case of $50s^{-1}$ - even though actually achieved strain rate is well below this target value.

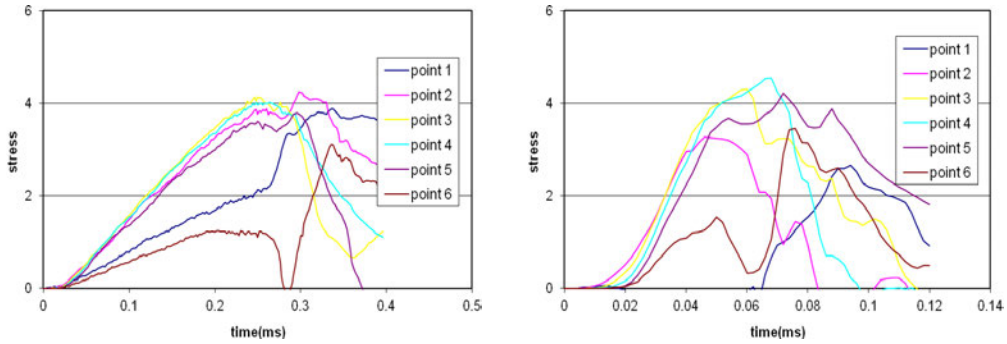

a) Nominal strain rate $1s^{-1}$ **b) Nominal strain rate $10s^{-1}$**

Figure 5-47: Tensile stress time histories

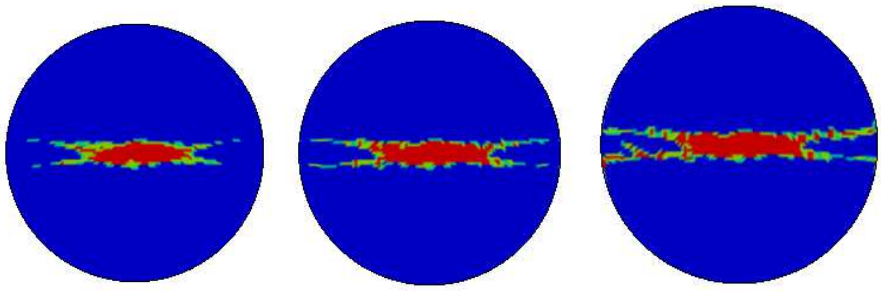

a) Nominal strain rate $1s^{-1}$ (0.3ms, 0.4ms, 0.5ms)

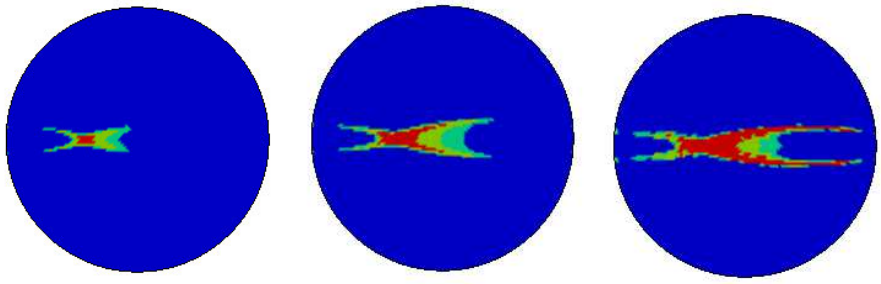

b) Nominal strain rate $10s^{-1}$ (0.06ms, 0.07ms, 0.08ms)

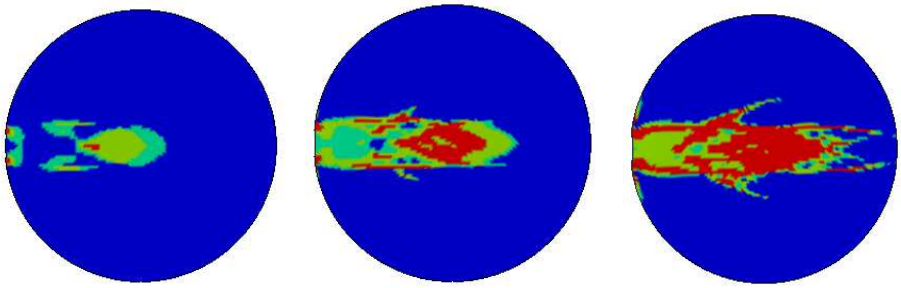

c) Nominal strain rate $50s^{-1}$ (0.04ms, 0.05ms, 0.06ms)

Figure 5-48: Illustration of the failure processes under different loading rates

5.7. Simulation of splitting tension using mesoscale model

In order to understand the possible effect of the mesoscale heterogeneity on the tensile behaviour of concrete in a splitting setup, the mesoscale model is adopted to perform the same analysis under different strain rates. The mesoscale model for the splitting specimen is constructed as a thin disk, incorporating random polygon-shaped coarse aggregates embedded in the mortar matrix, and the interfacial transition zone (ITZ) layer, as illustrated in Fig. 5-49. The diameter of this disk is 50 mm.

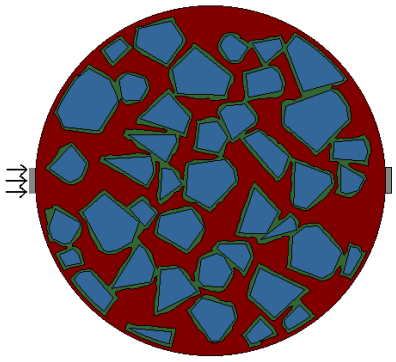

Figure 5-49: Mesoscale model for splitting tension simulation

The failure process of the mesoscale concrete at different nominal strain rates of $1s^{-1}$, $10s^{-1}$ and $50s^{-1}$ are shown in Fig. 5-50. For each strain rate, the failure stages are at rising-time, peak strength and final failure.

For the relatively low rate ($1s^{-1}$), the tensile damage develops in a rather uniform manner at different stages along the diameter, which agree with the results from the homogeneous concrete model in Fig. 5-34. Due to the presence of the aggregates, the damage (crack) region is irregular and has a broader band than that in the homogeneous model. Under the medium strain rate of $10s^{-1}$, crack initiates from the loading side and propagates along the diameter. However a general splitting pattern is still maintained. Under the higher nominal strain rate of $50s^{-1}$(actual achieved strain rate is much lower than this value as explained before), cracks appear to develop in a radiating fashion starting from the loading point, indicating a very different stress condition from the desired splitting tension. Consequently, the loading condition can no longer be considered as a valid splitting tension, and the

results should not be simply interpreted to arrive at an estimation of the dynamic tensile strength.

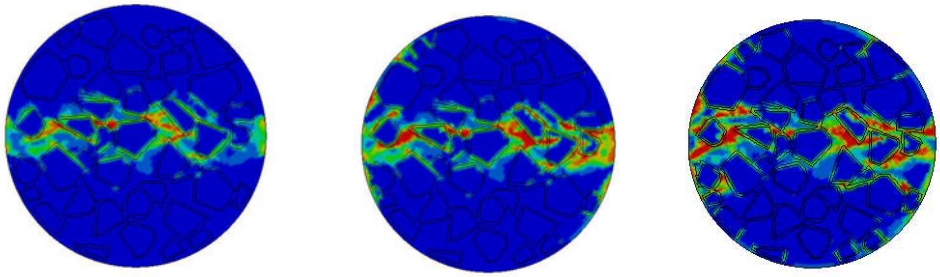

(a) Tensile strain rate=1s^{-1}

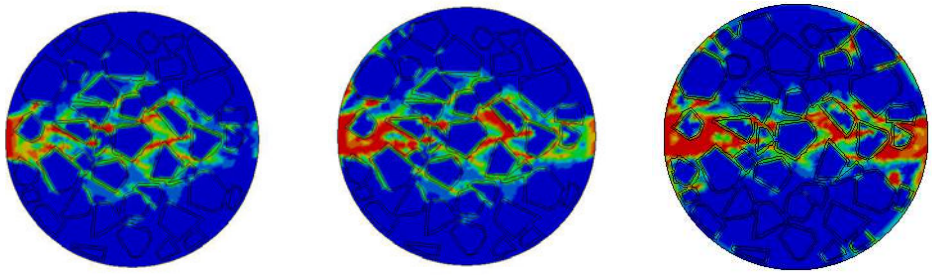

(b) Tensile strain rate=10s^{-1}

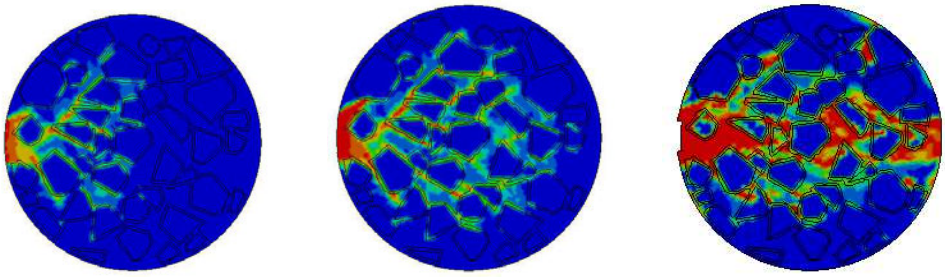

(c) Tensile strain rate=50s^{-1}

Figure 5-50: Failure process of the concrete plate at different strain rates

Further comparison of the splitting tensile strength as inferred from the maximum splitting forces with the results from the homogeneous models indicate that the presence of the stronger aggregates has an appreciable effect on the achieved apparent tensile strength. Based on the preliminary results herein, such an increase due to the mesoscale heterogeneity could amount to about 20%.

5.8 Concluding remarks

This chapter has presented a comprehensive evaluation of the soundness of using the Brazilian (splitting) technique for the dynamic tensile test of concrete-like materials under high strain rate. The key issues investigated include the variation of the stress state, tensile stress distribution with the specimen, as well as the involvement of the structural effect (transient wave) as the loading rate increases. Based on the results from analysing the split tension on a typical 50mm specimen, the following conclusions may be drawn:

1) For a strain rate up to about $10s^{-1}$, the assumptions of a static splitting equilibrium condition may be considered as valid. A generally uniform tensile stress distribution can be built up along the loading diametric direction. The formation of the crack failure takes place at the time consistent with the attainment of the peak boundary force. A splitting tension controlled failure can be achieved.

2) When strain rate further increases, herein for example with a nominal target rate of $50s^{-1}$, the stress and strain rate states become much more complicated. Firstly, due to a significant wave propagation effect, the strain rate is not uniform within the specimen. Strong non-uniformity in the tensile stress distribution is also found.

3) Examination of the development of stresses and the damage indicates that failure initiates within the specimen well before the above specified target strain rate of $50s^{-1}$ could be reached. Associated simulation studies also indicate that any attempt to promote the attainment of such a higher strain rate in a splitting setup could cause localized compressive damage in the specimen rather than a tensile controlled failure mode. These observations effectively suggest that for dynamic splitting test of concrete a valid strain rate limit may reasonably be set on the order of $10s^{-1}$.

4) Results from the numerical analysis without the consideration of the DIF at the material model level tend to show little change in the achieved dynamic tensile strength. This suggests that the experimentally observed large DIF in tension cannot be associated with the dynamic structural effect as in the case of dynamic

compression. This observation is consistent with those obtained in some other recent studies. Furthermore, analysis using the current mesoscale model suggests that the presence of the strong aggregates could make an appreciable contribution (order of 20%) in the increase of the dynamic tensile strength.

Chapter 6: Development of a 3D mesoscopic finite element model

Strategy is about making choices, trade-offs; it's about deliberately choosing to be different.

--Michael Porter (Economist, 1947-)

6.1 Introduction

Mesoscale analysis of concrete-like materials in 2D has inherent limitations in representing a realistic stress environment under dynamic loading, particularly with regard to capturing lateral inertia confining effect. Thus a pseudo 3D model has been developed and applied in the analysis of the strain rate effect under dynamic compression in Chapter 3 and 4. Understandably, a true 3D mesoscale model is a more desirable solution in representing more realistically the material heterogeneous structure.

Previous research on the modelling of 3D aggregate particles has simplified the aggregate geometry into simple shapes. A common approach is to represent the aggregates with spheres (Wriggers and Moftah, 2005; Mishnaevsky, 2006; Zhou and Hao, 2009). A mixture of spherical shapes and ellipsoids has also been used (Leite et al., 2004). A modified version of the ellipsoid function was proposed by Hafer et al. (2006), and this method made it possible to model different shapes to lead to a better approximation of real aggregates. An alternative idea of generating the meso-structure is creating aggregate domain from prescribed array of voxels (or lattice) with given shapes of aggregates (Mishnaevsky, 2006). This method has great advantage in terms of FE meshing. However, unsmooth elements exist alongside the boundary. A new method based on polytope representation, which is generated from Delaunay tessellation and gives more accurate approximation of particle shapes, was given in Caballero's research (Caballero, 2006). The Delaunay tessellation is

employed to yield natural partition of the structure, and aggregate shapes can then be generated using a shrinking method. This technique cannot ensure a desirable side grading in the process.

The polytope representation is arguably the best approximation of the shapes of natural and crushed aggregates. This chapter presents a method to build 3D concrete meso-structure based on 3D polyhedral-shaped aggregates. In this method, the polytope is represented by convex hull in R^3, which is the minimum convex set containing a series of points generated randomly. The algorithm of building a convex hull is then used to generate aggregate particles. To enable greater flexibility in the simulation of the real shapes of the aggregate particles, flaky and elongated shapes are also considered.

Similar to the generation of the 2D mesoscale model, the generation of a complete 3D meso-structure herein also uses the take-and-place procedure (Schlangen and van Mier, 1992; Wang et al., 1999). In the 3D case, the take-procedure involves the generation of an independent polyhedron whose nominal size follows a predefined size distribution; while the place-procedure involves placing the particle centred at a random position in a pre-defined 3D space, e.g. a cube or a cylinder, without intersection with other polyhedrons. A modified intersection detecting algorithm is proposed and used in the place procedure based on Dobkin's separation algorithm (1985). A shrinking strategy is used in the generation of the ITZ domain.

The chapter consists of five sections. Following the introduction, Section 6.2 provides a short review of literature on the geometry and modelling of aggregate, and presents a convex hull based approach for generation aggregates in 3D. The procedure to generate a meso-structure is discussed in Section 6.3, together with a method to model the ITZ in the 3D mesoscale model with solid elements. To mesh the highly unstructured meso-structure, a Delaunay triangulation refinement mesh code is utilized, and this is discussed in Section 6.4. Some preliminary simulation results are introduced and discussed in the last part of the chapter.

6.2 3D random aggregate particle generation

Aggregates are generally random 3D granular materials, which are mostly made of natural rocks and sands, although synthetic materials like lightweight concretes are also used to some extent. The shape and texture of aggregates can have significant influence on the physical and mechanical properties of concrete. Aggregate shapes affect the workability, which is determined by the surface-to-volume ratio of aggregate particles; they also affect the adhesion condition between mortar and aggregate particles.

The granular materials used for concrete mix usually fall into two categories: natural sand or gravel material, and angular material (such as crushed stones) with sharp edges and corners. The particle shape and surface texture of aggregates can be classified as (British Standard 812, 1975): rounded or well-rounded, irregular (naturally), flaky (material of which the thickness is small relative to the other two dimensions), elongated (material in which length is considerably larger than the other two dimensions). For the sake of simplification, highly irregular shapes are ignored in the current modelling.

One classic approach to modelling the shape of gravel aggregates is based on the morphological analysis developed by Beddow and Meloy(1980). The trace of aggregate shape is represented as a Fourier series:

$$r(\theta) = r_0 + \sum_{m=1}^{\infty} A_m (\cos m\theta + x) \tag{6.1}$$

In this equation r_0 is average radius. The term $\sum_{m=1}^{\infty} A_m (\cos m\theta + x)$ reflects the characteristic of particle contour where A_m represents the magnitude and m represents frequency. Meloy's morphological law showed that the relation of $\ln(A_m)$ and $\ln(m)$ can be approximated by a straight line:

$$\ln(A_m) = g \ln(m) + h \tag{6.2}$$

Based on this law, the shape of a gravel particle may be approximated by a series of short straight line segments (Wang and Kwan?, 1999). The approximation of 2D angular particles using polygons is straightforward; details of this method can be found in (Wang et al., 1999; Carlos et al., 2006). In some 3D mesoscale modelling researches, a spherical particle shape is assumed for all kinds of particles (Wriggers and Moftah, 2006; Schlangen and van Mier, 1992; Zhou and Hao, 1999), while in some other studies, a 3D elliptical shaped was used (Hafner et al., 2006), which covers the elongated and flaky shaped particles. Carlos et al. (2006) also proposed a method to model 3D particles with polytopes, which were generated from Voronoi diagram of a prescribed point set. This method provides a better approximation than spherical shape; however, size grading cannot be made to satisfy a pre-defined curve but rather is dependent upon the pattern of random points.

In the present research, a framework of generating random 3D concrete meso-structure is proposed. Both gravel and angular particles are approximated with polytopes. The points used to generate the polytope have random numbers, which makes it possible to generate gravel shapes with larger point numbers and angular shapes with small point numbers. Once polytopes become available, flaky and elongated shapes are generated based on a shrinking and elongation method. The take and place procedure is used so that a prescribed aggregate size grading can be guaranteed.

In what follows, the method to generate common polytopes and flaky, elongated particles is presented. Some geometry terms regarding the polytope generation and the intersection issue are introduced at the outset.

6.2.1 Geometry preliminaries

In the 3D meso-structure considered herein, the aggregate particles are geometrically modelled as disconnected polytopes (bounded polyhedra). A polytope can be defined equivalently as a convex hull of a finite point set in R^3. Thus it is possible to generate a random shaped aggregate particle from a set of 3D random points. Several terms will be used frequently in this chapter, and these terms are explained below.

An oriented plane $H(n,c)$ in 3D in vector form:

$$H(n,c) = \{x; n \cdot x = c\} \tag{6.3}$$

where n is the normal vector of the plane. Base on this plane, two half spaces

$$H^+(n,c) = \{x; n \cdot x > c\},\ H^-(n,c) = \{x; n \cdot x < c\} \tag{6.4}$$

can be defined. Along with the list of vertices V, a 3D polytope can be represented by a list of plane indicating a facet.

A d-simplex, is an n-dimensional polytope with (n+1) vertices. For instance, a 2-simplex is a triangle and 3-simplex is a tetrahedral. The d-simplex is a fundamental polytope that is useful in the intersection detection. More details about concepts and algorithms on convex hull in the field of computational geometry can be found in Berg and Cheong (1998).

6.2.2 Generating regular aggregates

As is stated earlier, the shape of regular aggregates (excluding the flaky and elongated ones) is represented by a convex hull. The convex hull for a set of points L is the minimal convex set containing P. In the 3-D simulation, the convex hull is the smallest convex 3D polytope that contains predefined points.

The generation of a random shaped convex polytope starts from a set of random points L. Each point in the list L is represented in the spherical coordinates by radius r, inclination angle θ and azimuth angle φ. They are random numbers from a uniform distribution:

$$\begin{aligned} r &\sim U[r_0 - d/2, r_0 + d/2] \\ \theta &\sim U[0, 2\pi] \\ \varphi &\sim U[0, 2\pi] \end{aligned} \tag{6.5}$$

In the equations above, r_0 is the nominal size discretized from an aggregate grading curve. d is the discretization length.

The spherical coordinates are then transformed to Cartesian coordinates by:

$$R_x = r\sin\theta\cos\varphi \tag{6.6}$$

$$R_y = r\sin\theta\sin\varphi \tag{6.7}$$

$$R_z = r\cos\theta \tag{6.8}$$

There are various approaches which may be used to compute convex hull in the field of computational geometry. The beneath-beyond algorithm, which is used in the current research to construct a polytope, is one of these methods that can be found in literature (e.g. Berg and Cheong, 1998; Edelsbrunner, 1987). This method works incrementally, i.e., it adds one point at a time to an already constructed convex hull. Matlab uses the implementation of Qhull, which is a computational geometry library, for their computational geometry functions. Thus the construction of aggregate shape can be easily implemented in Matlab.

An example of the above algorithm to create a convex hull is shown in Fig. 6-1.

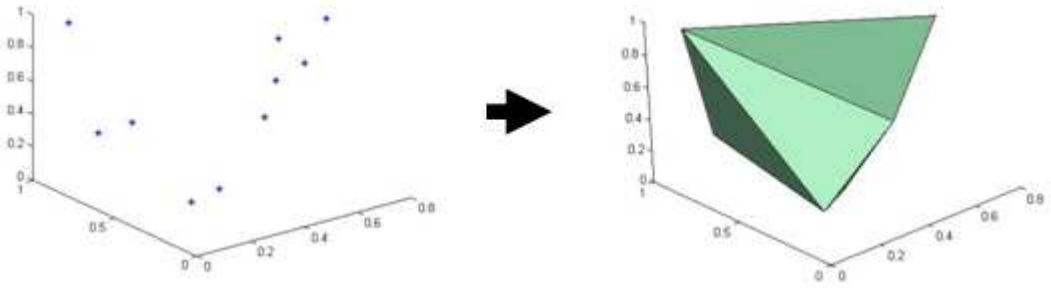

Figure 6-1: Generation of one aggregate particle

6.2.3 Generating flaky and elongated aggregates

The idea of elongation on individual particle to build a elongated one can be found in Wang et al. (1999) and Tu and Lu (2011). In this study, both flaky and and elongated aggregates are generated based on the regular polytope generated by the algorithm described in 6.2.1. A flaky shape is implemented by introducing a shrinkage ratio on

one dimension. To keep the volume at a constant value during shrinking, the other dimensions are expanded.

The shrinkage algorithm can be represented by:

$$R_x' = s * R_x \tag{6.9}$$

$$R_y' = R_y / \sqrt{s} \tag{6.10}$$

$$R_z' = R_z / \sqrt{s} \tag{6.11}$$

In above equations, R (whose three components are R_x R_y and R_z) is the coordinate of each vertex in a regular polytope. For s > 1, the transform generates an elongated polyhedral; while for s < 1, the transform generates flaky polyhedral. In the implementation, the ratio *s* is taken as random number from 0.5 to 1.5. To make sure the shrinkage is conducted on a random orientation, the coordinates are rotated to a random direction after the operation. In R^3, coordinate system rotations of the *x*-, *y*-, and *z*-axes are represented in Euler angle. The vector form of the rotation is given by:

$$R = T * R' \tag{6.12}$$

where *R'* is column vector of Cartesian coordinates. The rotation matrix *T* is given by,

$$T = \begin{bmatrix} \cos\gamma & \sin\gamma & 0 \\ -\sin\gamma & \cos\gamma & 0 \\ 0 & 0 & 1 \end{bmatrix} \begin{bmatrix} 1 & 0 & 0 \\ 0 & \cos\beta & \sin\beta \\ 0 & -\sin\beta & \cos\beta \end{bmatrix} \begin{bmatrix} \cos\alpha & \sin\alpha & 0 \\ -\sin\alpha & \cos\alpha & 0 \\ 0 & 0 & 1 \end{bmatrix} \tag{6.13}$$

where α , β and γ are the Euler angles. α and γ are random numbers from uniform distribution U(- π , π) and β is random number from U(0, π).

Fig. 6-2 presents a comparison of individual aggregate shapes generated with different parameters. For each group of parameters, orthogonal views in x-y, y-z and z-x plane are shown. Figure 6-2 (a) and (b) shows the result with 10 random points. In these graphs, clear angular edges and corners can be found whether there is elongation or not. When the number of random point taken is a greater value such as

20, as in Figure 6-2 (c) and (d), the shape of the polytope becomes smoother. The effect of elongation is more obvious than the 10 point group, in which small number of points actually generates irregular shapes. Further smoother shapes are found in groups (e) and (f) which are generated with 30 random points.

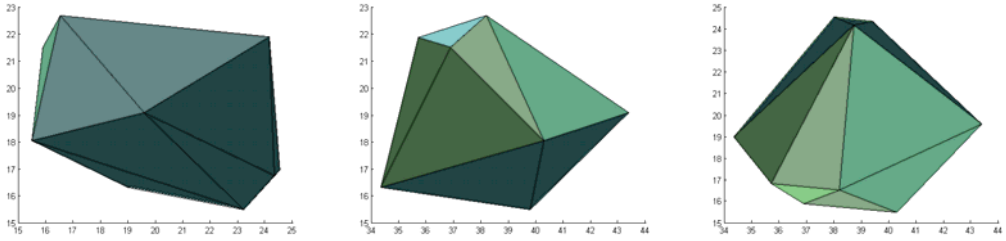

(a) Number of random point=10, regular polytope

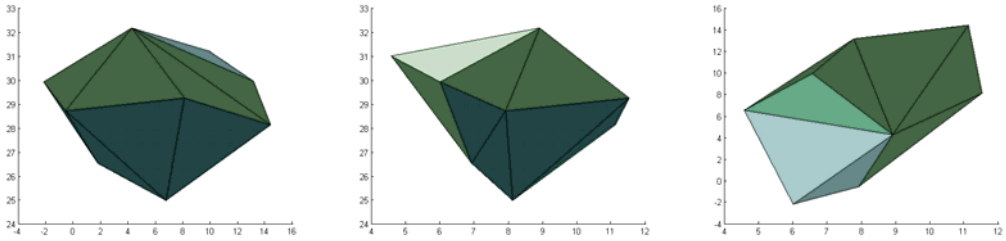

(b) Number of random point=10, elongation ratio s=1.5

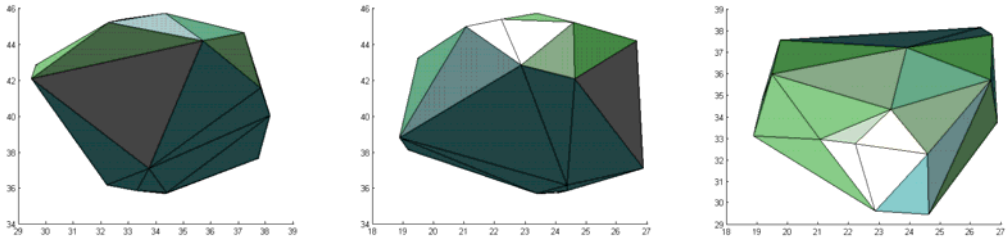

(c) Number of random point=20, regular polytope

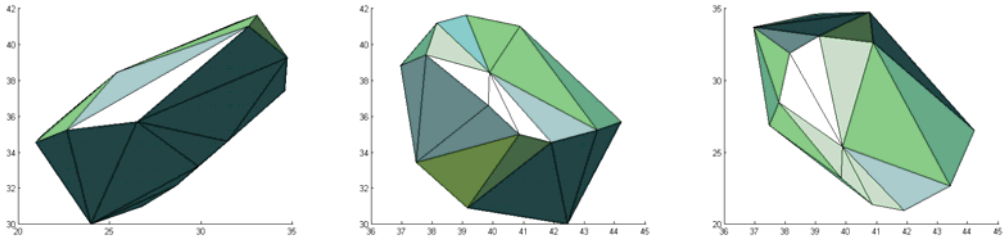

(d) Number of random point=20, elongation ratio s=1.5

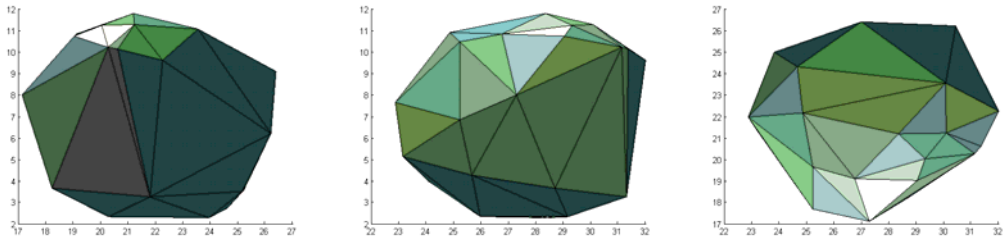

(e) Number of random point=30, regular polytope

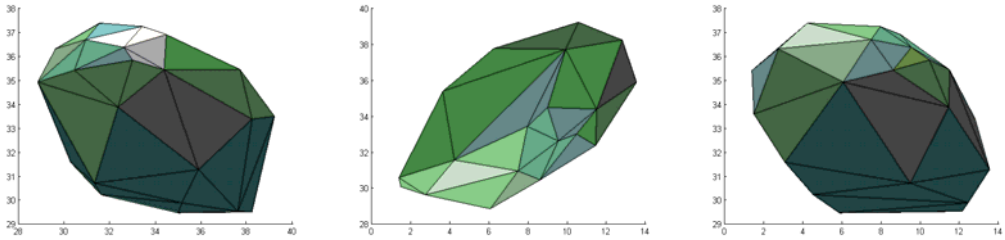

(f) Number of random point=30, elongation ratio s=1.5

Figure 6-2: Aggregate shapes with different parameters

6.3 Modelling concrete meso-structure

The main purpose of this chapter is to develop more realistic 3D mesoscale model for the analysis of the influence of heterogeneity under various loading conditions. Before incorporating the ITZ phase, we will generate only a two phase concrete meso-structure, i.e., with aggregates and mortar matrix.

6.3.1 Size grading

Like in the 2D mesoscale model described in Chapter 3, aggregates should be graded in order to mimic the natural aggregates and also minimise the "gap" between aggregate particles. A grading curve is usually employed to define the accumulated distribution of aggregate particles. Generally, the volumetric ratio of all aggregates, including fine aggregates is 0.7-0.8 (Mindess et al., 2002), and coarse concrete is around 0.4-0.5 (Wriggers and Moftah, 2006).

In the generation of the 3D meso-structure, the grading of aggregates follows also the Fuller Curve. Briefly, the Fuller Curve gives the volumetric ratio of aggregates as a function of aggregate size D:

$$P(d) = 100.0 * (d / d_{\max})^n \tag{6.14}$$

where $d_{\max}$ is the maximum size of aggregates and parameter n is in the range 0.45-0.7 (Wriggers and Moftah, 2006). In a basic 3D mesoscale model considered herein, a cubic concrete specimen of 50mm in each side will be simulated. The maximum size of aggregate is about 10mm to make a good concrete mix. *n* is taken as 0.5 in the Fuller's curve.

The Fuller curve in a 3D implementation can be expressed as (Wriggers and Moftah, 2006)

$$V_{agg}[d_s, d_{s+1}] = \frac{P(d_{s+1}) - P(d_s)}{P(d_{\max}) - P(d_{\min})} \times R_{agg} \times V_{con} \tag{6.15}$$

where:

$[d_s, d_{s+1}]$ is the discretized aggregate size range

$P()$: Grading curve

V_{agg} : Volume of aggregate

R_{agg} : Volume ratio

V_{con} : Volume of concrete

It is noted that in a typical sieve analysis, concrete aggregates are usually divided into coarse and fine fractions. The coarse aggregates are usually considered to be the particle that is larger than 4.75mm (retained on the 4.75mm sieve). The fine fractions mix with cement and form the mortar matrix. Similar to the treatment in the 2D mesoscale model, only the "course" aggregates are modelled explicitly as aggregate

particles, and the size range can be further divided into a few sub groups for the sake of numerical implementation, For example if aggregates of 3-10 mm (small aggregate concrete) is considered, they may be discretized to three ranges of 3-5mm, 5-7mm, 7-10mm. From the Fuller curve shown in Fig. 6-3, we can calculate their relative volume percentage in aggregates as 17%, 15% and 19% respectively. If the volume ratio of all aggregates in the total concrete volume is considered to be 40%, the final percentage of the above three aggregate groups will be 13.5%, 11.5% and 15%.

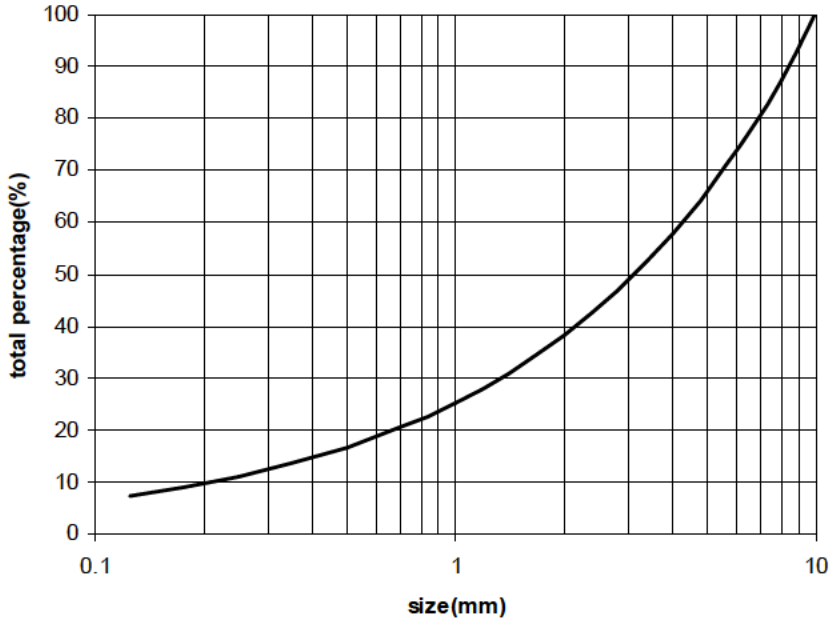

Figure 6-3: Typical aggregate size grading curve

6.3.2 Take-and-place procedure in 3D

The take-and-place procedure is commonly used in the generation of meso-structure as described in Chapter 3. Herein this strategy is also used for constructing the 3D mesoscale model. In the take-procedure, the Fuller Curve is first discretized into several segments. The algorithm described in Section 6.2 is then used to generate a polytope according to a randomly sampled radius R. Cartesian coordinate is used in the place-procedure. A randomly generated point within the concrete space is then considered as the reference point for the aggregate particle to be placed.

A summary of the integrated take-and-place procedure for 3D is given below:

Step 1: Starting from the maximum aggregate size range, generate one polytope from the current size level according to the algorithm in Section 6.2.

Step 2: Place the particle into the concrete space. Three conditions need to be satisfied:

a) The aggregate particle should be within the boundary the concrete space;

b) There is no overlapping among aggregate particles;

c) A minimum gap

If n particle overlaps with an earlier placed one, then a new position is assigned and the place procedure is tried again.

For placing, a random position within the specimen space is chosen to place the polytope. Thus, the transformation of the coordinates is made by:

$$R' = R + D \tag{6.16}$$

D is a random number from U(0, D_{max}), where D_{max} is the side length of the specimen.

Step 3: Repeat step 1-2 until there is not enough space for placing any more particles in the current grading segment or the volume ratio of current grading segment is reached.

Step 4: Go to next level of grading segment; the algorithm in terminated if all size grading segments are finished.

In order to make the checking procedure in step 3 more efficient, only a limited area around the reference point is considered, and a speed-up algorithm is developed as will be described in the next section. For condition (a) it is easy to satisfy as long

as all vertexes are placed within the boundary of the concrete. More details on checking of condition (b) is also given in next section.

6.3.3 Intersection detection of aggregate particles

The place procedure involves a significant step: checking the intersection of polytopes with already placed ones in the concrete meso-structure. In the 2-D situation, this can be done by assuring: 1) all vertices are outside the boundary of adjacent particles and 2) no edge intersects with the edges of adjacent particles (Wang et al., 1999). The same idea can be extended to 3D as well. However, it would require much more intensive computation, especially for the checking of the second condition, i.e. no intersection between all the surfaces.

6.3.3.1 A fast detection algorithm for two particle inclusions

A few advanced algorithms have been proposed for constructing the intersection of 3D polytopes. Muller and Preparata (1978) proposed an algorithm to determine the intersection in $O(n\log(n))$ time. Dobkin and Kirkpatrick (1985) presented an linear algorithm for determining the separation of two convex polytope P and Q in k-dimensional space. Dobkin's algorithm is based on a hierarchical representation of polytopes. For a 3-dimensional polytopes P, the hierarchical representation $H(P)$ are a nested sequence of polytopes $P_1 \supset P_2 \supset \ldots \supset P_k$, where P_1=P, P_k is a d-simplex and the vertices of $V(P_i)$ - $V(P_{i+1})$ are independent set in P_i. A complete algorithm to generate the hierarchy representation of a polytope was given by Edelsbrunner (1987).

With the nested polytope hierarchy, linear time $O(n)$ (i.e. computation time increase linearly with number of vertex) is available to determine the separation of two polytopes (Dobkin and Kirkpatrick, 1985). The separation of two convex polytopes is the minimal distance, which is not necessarily realised on the vertices, between P and Q.

A modified version to determine the intersection of 3D polytopes based on Dobkin's algorithm is given in the following flow chart:

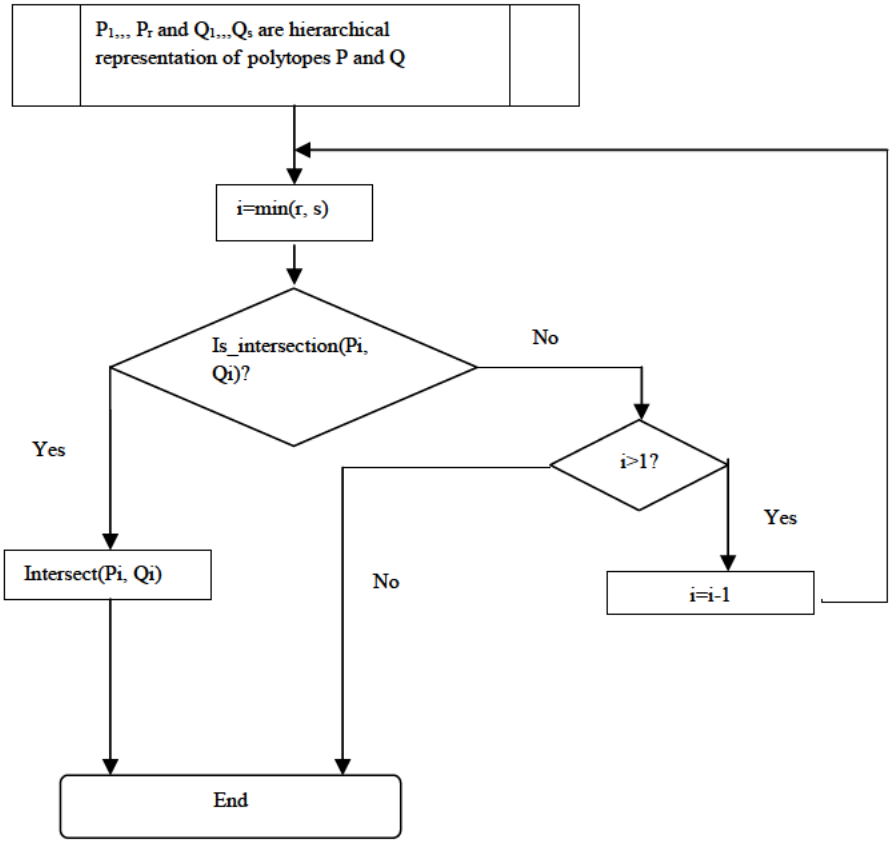

Figure 6-4: The flow Chart for 3D intersection detection

The procedure "Is_intersection" returns a Boolean value upon whether Pi intersects with polytope Q_i..

6.3.3.2 Speed-up detection checking by bounding sphere

In the take-place procedure, the larger aggregates are first placed at a random position. When small particles are to be placed at a random position, trials are more likely to fail than placing the larger size ones, and there are usually more numbers of smaller particles that need to be placed. The computational time can be substantial, thus an efficient intersection detection algorithm is necessary. The algorithm described in 6.3.3.1 gives a $O(n)$ time algorithm for the detection of intersection of two polytopes. In the place procedure, it is apparent that there is no need to check the possibility of intersection with all polytopes that have already been placed. A pre-

selection process can be employed to choose the polytopes that are “possible” to intersect with the current one.

To assess the possibility of intersection, for each new polytope, a bounding sphere can be defined. The bounding sphere for a particular polytope is a sphere that has the same centre with this polytope, while its radius is defined as the distance between the centre and the furthest vertex, as shown in Fig. 6-5. Before the intersection detection, a linear lookup algorithm can be realised first to detect which bounding sphere intersects with the current one. For the intersection of spheres, the detection calculation is straightforward. After the looking-up process, the actual intersection detecting algorithm need only be performed with polytopes whose bounding sphere intersects with that of the current one.

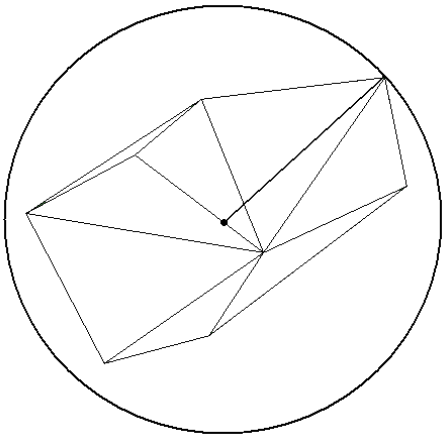

Figure 6-5: Illustration of bounding sphere of aggregate particle

Fig. 6-6 shows some examples of the placement of aggregate particles. Only one range of aggregate size is shown here just to illustrate the effects of random point numbers and elongation ratio. The aggregate size is taken as 10mm and the volume ratio is 10%. Fig. 6-6 a) and Fig. 6-6 b) shows the shapes generated from 10 and 20 random points, and no shrinking and elongation are employed. Fig. 6-6 c) and Fig. 6-6 d) shows the shapes with a shrinking and elongation ratio between 1.0 and 2.0. Quasi-round shapes are found if no shrinking and elongation is applied, while more random points reduce the sharpness of aggregate angles.

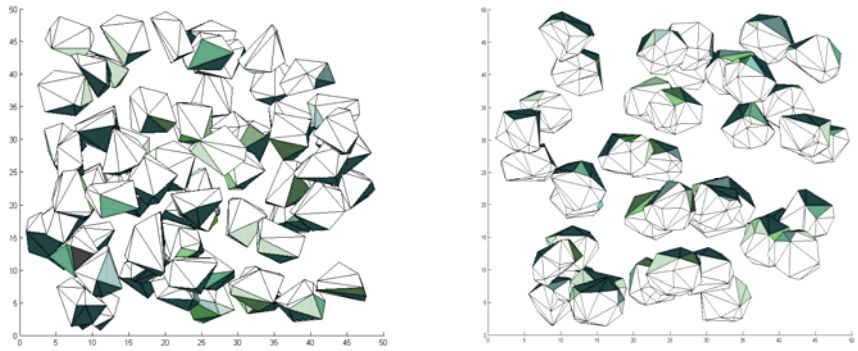

a) Points=10, no shrinking and elongation b) Points=20, no shrinking and elongation

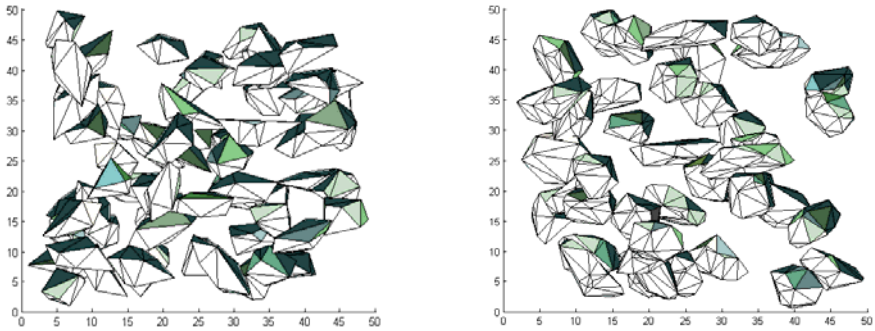

c) Points=10, shrinking and elongation ratio 1~2 d) Points=20, shrinking and elongation ratio 1~2

Figure 6-6: Aggregate particle distributions

6.3.4 Modelling of ITZ in 3D mesoscale model

Similar to the treatment in the 2D mesoscale model in Chapter 3 and 4, herein we use an equivalent layer of thin solid elements surrounding the aggregates to represent the effect of ITZ. In 3D situation, the ITZ layer is generated by shrinking the 3D aggregate particles by a certain small fraction, while the mortar space will be kept unchanged.

A schematic diagram of shrinking procedure is shown in Fig. 6-7.

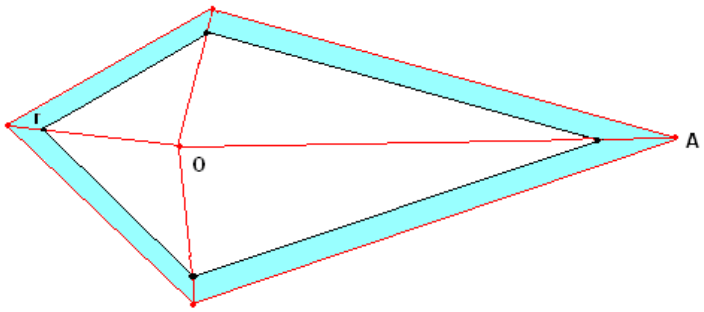

Figure 6-7: Generation of ITZ by Shrinking of aggregates

A shrinking strategy, which has been used as an alternative method to generate aggregate particles (Caballero et al., 2006) is extended here to generate the ITZ layer. The shrinking is done with respect to the centre of a polytope. Two options of shrinking are considered here because the radius of vertices varies. To minimise the thickness of the ITZ elements, the distance between the centre of the polytope and each vertex is shrunk by a constant thickness ratio for all vertex:

$$OA' = OA * r \tag{6.17}$$

To keep a generally uniform thickness for all the ITZ elements among aggregates with different size levels, the ratio r is related to a common nominal aggregate size R_0. For a target element size of l_{elem} in the final FE mesh, it follows:

$$r = \frac{l_{elem}}{R_0} \tag{6.18}$$

Once the shrinking is completed for all aggregates, the space created in the shrinking process (i.e. between the shrunk aggregates and their original space) is allocated to be a new group of polytopes (convex hull), which becomes the ITZ domain.

6.4 Finite element mesh generation

When the generation of aggregate particles and the ITZ domain is completed, the remainder of the concrete space automatically forms the mortar matrix. Thus, all three phases are generated resulting in a complicated 3D structure.

For meshing of the mesoscale structure, triangle and tetrahedral meshing techniques are the most common forms of unstructured mesh generation in 2D and 3D, respectively. Specific smoothing algorithms for meshing unstructured domain include Octree, advancing front and Delaunay refinement (Owen, 1998). In the Octree method, an unstructured domain is subdivided into small cubes until a required resolution is reached. The advancing front method, also known as moving front, first triangulate the boundary surface then progressively generates tetrahedral mesh from these boundaries (Lohner, 1996). The Delaunay refinement is an algorithm for generating meshing based on Delaunay triangulation. A typical way is to first mesh the boundary of the geometry to generate the initial node set. The boundary nodes are then triangulated with Delaunay triangulation.

The meshing code used in the present research, namely TetGen, developed by Si (Si and Cartner, 2005; Si, 2006), is one type of Delaunay refinement. This algorithm is based on what is termed “constrained Delaunay triangulation”, which represents a situation that boundaries of the structure are not conforming to the Delaunay Triangulation.

In TetGen, the 3D unstructured geometry is represented by a more general input called piecewise linear complex (PLC). A method to decompose an PLC into a constrained Delaunay tetrahedralization (CDT) is developed in (Si and Cartner, 2004). A key problem in meshing a PLC is determining the existence of a CDT. The method successfully resolves the problem of non-existence of a CDT by updating the input PLC into another PLC which is topologically and geometrically equivalent to the original one and does have a CDT.

One potential problem in the current generation algorithm for ITZ is that the ITZ volume is a portion from the initial volume of aggregates, and thus the aggregate particle generated in the take-procedure should considered the size of neighbour ITZ

An example of the 3D structure and meshing result is shown in Fig. 6-8 and 6-9. Note that in the mesh setting, the length of the tetrahedron has a nominal size 1.5mm-3mm, resulting in 300,000 to 400,000 elements for a 50mm cube specimen.

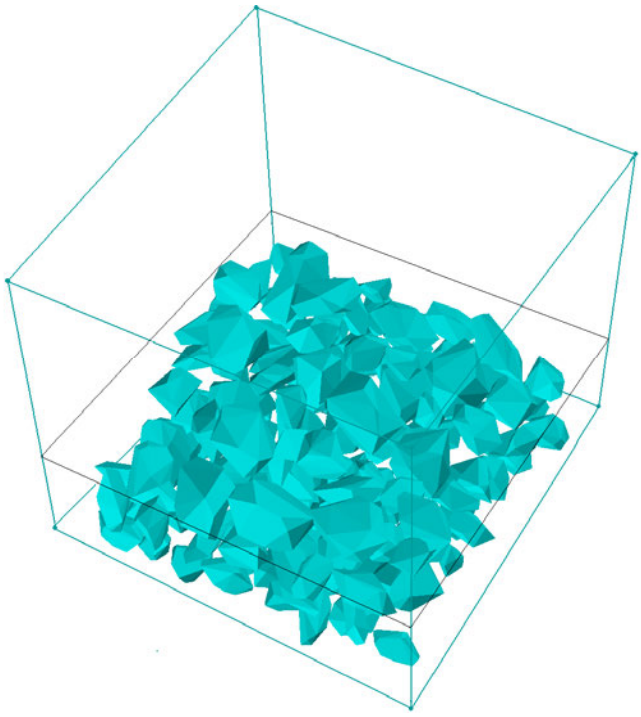

Figure 6-8: A slice of aggregate particles before meshing

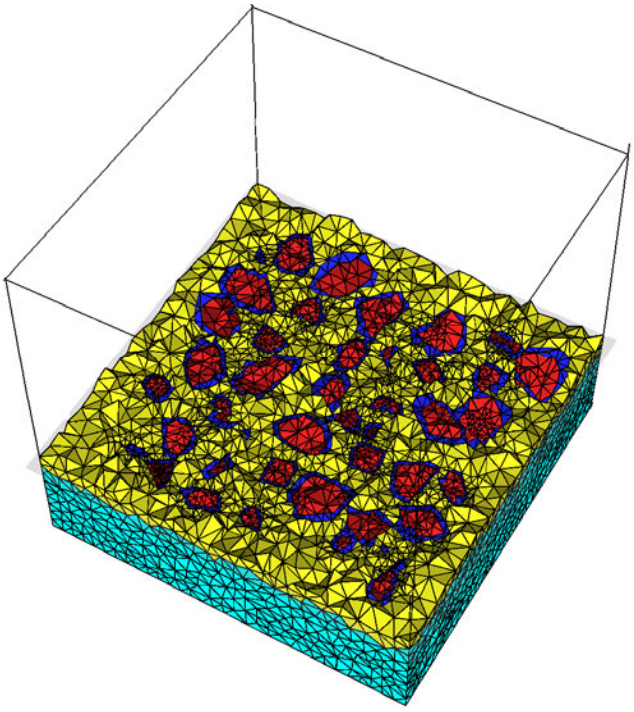

Figure 6-9: A slice of elements after meshing

6.5 Example modelling results using the 3D mesoscale model

An example simulation is carried out to test the general performance of the 3D mesoscale model. A cubic specimen of 50mm side length is modelled. The model parameters used in the simulation are the same as in the 2D studies (Chapter 3 and 4), as listed in Table 3-1. Similar to the 2D analysis, ITZ elements are modelled using the same material model as for mortar but with a reduced strength.

6.5.1 Stress and strain relation

Fig. 6-10 shows the compressive stress-strain curve with a loading rate of $10s^{-1}$. The stress-strain curves agree well with general experimental observations for this class of concrete considering the imposed strain rate. The result with consideration of the loading face friction shows an increased strength than the friction-free case, which is also reasonable.

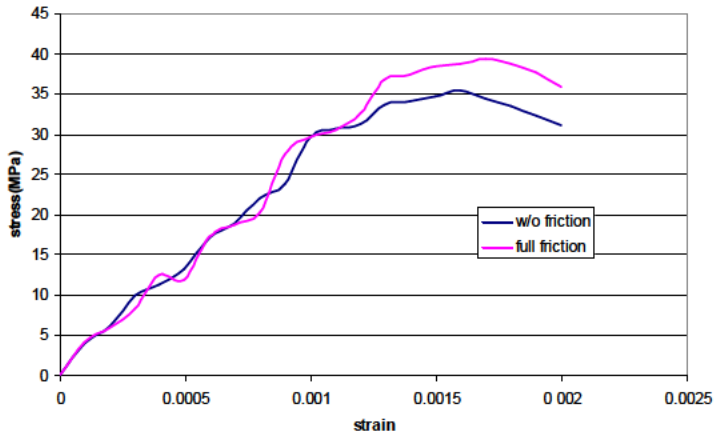

Figure 6-10: Stress-Strain relationship (Strain rate =$10s^{-1}$)

6.5.2 Damage patterns

Fig. 6-11 shows the final damage contours of the 3D mesoscale model, with comparison to typical failure patterns from experiments. As can be seen, classical difference in the failure patterns under the two different loading face friction conditions are re-produced well in the simulated results. In the friction-free boundary setting, the loading surface is severely damaged, along with distributed damage

within the specimen. On the other hand, under the fully friction-constrained loading condition, a confined area is created near the loading ends, and a double-cone pattern of failure is evident.

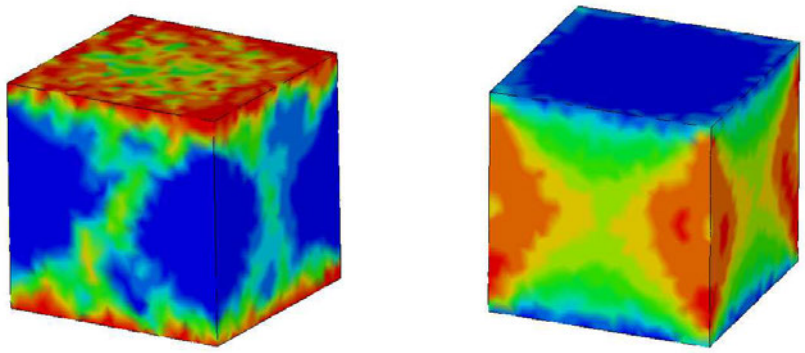

Figure 6-11: Concrete specimen Damage patterns from numerical simulation (left-free boundary, right-fully constrained)

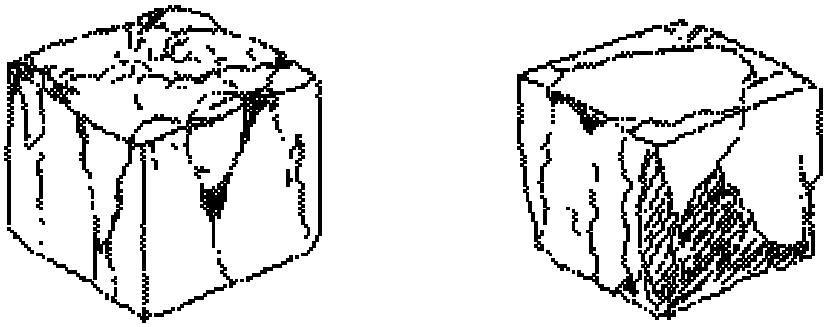

Figure 6-12: Concrete specimen Damage patterns from experiment after (Vliet, 1996) (left- Low friction, right- High friction)

6.6 Conclusions

In this chapter, a method for generating 3D meso-structure of concrete is presented by integrating the algorithms for generating random polytypos using convex hull and the take-and-place procedure. An algorithm for the creation of the ITZ domain is also provided. All the procedures are implemented using Matlab codes.

To control the computational time in the generation of the 3D meso-structure, a linear time intersection detection algorithm is proposed and implemented to speed up the process of the place-procedure.

A suitable meshing code with constrained Delaney triangulation refinement is utilised to mesh the unstructured shapes of the mesoscale structure, leading to a complete FE model for loading applications.

Example analyses using the 3D mesoscale model demonstrate stable and consistent performances in terms of the stress-strain response and the damage patterns. The 3D mesoscale model can be applied in the future, both for general loading and for high strain rate applications.

Chapter 7: Conclusions and recommendations for future work

The principle objective of this research has been to develop a realistic and effective mesoscale modelling framework, especially in a 3D environment, for concrete-like materials subject to high strain rate loading. Specific mesoscale models are subsequently developed to investigate into the dynamic compressive and tensile behaviour of this composite material, with a particular focus on the possible contributions of the structural dynamic effect (inertia) and the mesoscopic heterogeneity towards the apparent DIF in loading conditions, as well as the validity and adequate interpretation of high dynamic experimental information.

7.1 Summary of main conclusions

7.1.1 Strain rate effect on dynamic compressive behaviour of concrete

A comprehensive mesoscopic investigation has been conducted into the dynamic compressive behaviour of concrete using a novel pseudo 3D mesoscale model. Comparisons have been made with 2D mesoscale as well as and 3D homogeneous models. The development and distribution of stresses in concrete specimens under dynamic compression with various strain rates were studied, and a general DIF curve was also derived based on the numerical experiment data. Further study was carried out to investigate the stress wave effect and the resulting progressive damage in the specimens, especially in the strain rate regime that exceeds the strain rate limit governing a stress uniformity condition. The contribution of lateral confinement and mesoscale property are clearly identified. More specifically, the following conclusions have been drawn:

1) Numerical simulation results using the more realistic mesoscale model are found to support the augmentation that the compressive dynamic strength enhancement (compressive DIF) is primarily caused by the lateral inertia confinement within the sample specimen structure. A simulated DIF curve using homogeneous model without material DIF in the constitutive model could explain

nearly most of DIF curve observed in experiment. Furthermore, the mesoscale heterogeneity also plays a sensible contribution and the contribution tends to increase as the strain rate increases.

2) For strain rates up to the theoretical strain rate limit for compression, in a typical case about $50s^{-1}$ for the 50mm specimen, a reasonable uniformity of stress can generally be maintained. Consequently, the nominal dynamic strength and strain quantities as obtained from the end face responses (measured from the pressure bars in the case of SHPB tests) appear to represent well the actual bulk dynamic behaviour of the concrete.

3) With increase of the strain rate beyond the theoretical limit, the stress distribution tends to become increasingly non-uniform as the strain rate increases, and this results in progressive failure in a layer by layer fashion as the stress wave propagates from the front face towards the end face. Consequently, the nominal strength and strain response derived using any of the three different wave methods cannot produce consistent results. In lieu of a universal approach to tackle the situation, a dedicated numerical analysis would generally be required to provide necessary correlation for the interpretation and corrections of any test data that exceed the respective strain rate limits.

4) The presence of (strong) aggregates tends to develop increasingly higher stress than the mortar matrix as the strain rate increases. This gives rise to a non-negligible mechanism that contributes to the measured bulk DIF in the concrete specimens under compressions. Based on the numerical data obtained in this study, the contribution from the aggregates could amount to 20% or even more in the total dynamic strength enhancement at the higher end region of the strain rate spectrum.

7.1.2 Dynamic tensile strength and dynamic splitting tensile test

A comprehensive investigation into the extent of validity of the splitting test for determining the dynamic tensile strength has been conducted. The study focuses on the stress and strain states in a splitting configuration as the nominal tensile strain

rate increases, and hence the adequacy of deducing the tensile strength from the applied/measured splitting compression force.

1) At a strain rate smaller than $10s^{-1}$, the assumptions of the attainment of a static equilibrium condition in a splitting test are found to be general valid. A reasonable uniform distribution of the tensile stress can be built up before failure initiates.

2) When strain rate further increases, the stress and strain rate states become much more complicated. The strain rate is no longer uniform within the specimen, and significant non-uniformity in the tensile stress distribution develops. Failure initiates within the specimen well before the higher target strain rate, e.g. $50s^{-1}$ could actually be reached.

3) Results from the numerical analysis without the consideration of the DIF at the material model level tend to show little change in the achieved dynamic tensile strength, suggesting that the experimentally observed large DIF in tension is not inherently associated with the dynamic structural effect as in the case of dynamic compression. Furthermore, analysis using the current mesoscale model suggests that the presence of the strong aggregates could make an appreciable contribution (order of 20%) in the increase of the dynamic tensile strength.

7.1.3 Development and preliminary application of a true 3D Mesoscale model

To more realistically model the meso-mechanical processes and their effect on concrete under high strain rate loading, a true 3D representation of aggregate particles as 3D convex hulls enable the handling of the mesostructure generation by means of computational geometry algorithms.

To control the computational time in the generation of the 3D mesostructure, a linear time intersection detection algorithm is proposed and implemented to speed up the process of the place-procedure. A suitable meshing code with constrained Delaney triangulation refinement is utilised to mesh the unstructured shapes of the mesoscale structure, leading to a complete FE model for loading applications.

Example analyses using the 3D mesoscale model demonstrate stable and consistent performances in terms of the stress-strain response and the damage patterns. The 3D mesoscale model can be applied in the future, both for general loading and for high strain rate applications.

7.2 Recommendations for further research

With the availability of the 3D mesoscale model, comprehensive numerical studies can be carried out to more systematically evaluate the effect of the meso-mechanical processes in influencing the dynamic, as well as quasi-static, and complex stress conditions.

Continued improvement of the 3D mesoscale modelling framework should also be carried on. This will focus on a more rigorous ways of modelling the interfacial transition zone (ITZ, as well as more explicit representation of the fracture process and the resulting anisotropic effect.

The study should also be extended into the more general situation of reinforced concrete structures and the mesoscale processes in influencing the interaction between concrete and steel reinforcement under high rate loading. The mesoscale model also provides a useful means to investigate into other classical problems associated with concrete and reinforced concrete, such as the effect of confining reinforcement, shear cracking and shear resistance, the behaviour of 3-dimensional beam-column joints, and so on.

Mesoscale numerical studies could also be conducted to explore the optimized design of cement-based composite materials under dynamic loading, as well as effective strengthening and retrofitting methods against shock and blast effects.

Chapter 8: References

ANSYS Academic Research, v. 11.0.

ASM Handbook Volume 8: Mechanical Testing and Evaluation. (2000). ASM International.

Bacon, C. (1999). Separation of waves propagating in an elastic or viscoelastic Hopkinson pressure bar with three dimensional effects. International Journal of Impact Engineering, 22, 55–69.

Brara, A., Camborde, F., Klepaczko, J.R. and Mariotti, C. (2001). Experimental and numerical study of concrete at high strain rates in tension. Mechanics of Materials, 33(1), 33–45.

Bazant, Z. P. (1983). Scaling laws in mechanics of fracture. Journal of Engineering Mechanics., 119, 1828–1844.

Bazant, Z., Tabbara, M., Kazemi, M. and Pijaudier-Cabot, G. (1990). Random particle model for fracture of aggregate or fiber composites. Journal of Engineering Mechanics, 116, 1686-1705.

Beddow, J.K. and Meloy, T. (1980). Testing and characterization of powders and fine particles, Heyden.

Berg, M. and Cheong,O. (1998). Computational Geometry-Algorithms and Applications(3ed), Springer.

Bertholf, L.D. and Karnes, C.H. (1975). Two dimensional analysis of the split Hopkinson pressure bar system. Journal of the Mechanics and Physics of Solids, 23, 1–19.

Bischoff, P.H. and Perry, S.H. (1991). Compression behavior of concrete at high strain-rates. Materials and Structures, 24, 425–450.

Bolander, J. E., Jr., Hong, G. S. and Yoshitake, K. (2000). Structural concrete analysis using rigid-body-spring networks. Computer-Aided Civil and Infrastructure Engineering, 15, 120-133.

Bolander, J. E. and Le, B. D. (1999). Modeling crack development in reinforced concrete structures under service loading. Construction and Building Materials, 13(1-2), 23-31.

Brace, W.F. and Jones, A.H. (1971). Comparison of uniaxial deformation in shock and static loading of three rocks. Journal of Geomechanics Abstracts, 13(6), 4913–4921.

BS EN-812.(1975). Aggregates for concrete.

Caballero, A., Lopez, C. and Carol, I. (2006). 3D meso-structural analysis of concrete specimens under uniaxial tension. Computer Methods in Applied Mechanics and Engineering, 195, 7182-7295.

Carol, I., López, C.M. and Roa, O. (2001). Micromechanical analysis of quasi-brittle materials using fracture-based interface elements. Internternational Journal for Numerical Methods in Engineering 52(1-2), 193–215.

CEB-FIP Model Code 1990. (1993). Comite Euro-International du Beton. Redwood Books, Trowbridge, Wiltshire, UK.

Cotsovos, D.M. and Pavlovic, M.N. (2008). Numerical investigation of concrete subjected to compressive impact loading. Part 1: A fundamental explanation for the apparent strength gain at high loading rates. Computers & Structures 86, 145-163.

Cusatis, G., Bazant, Z.P. and Cedolin, L. (2006). Confinement-shear lattice csl model for fracture propagation in concrete. Computer Methods in Applied Mechanics and Engineering, 195(52), 7154-7171.

Davies, E.D.H. and Hunter, S.C. (1963). The dynamic compression testing of solids by the method of the split Hopkinson pressure bar. Journal of the Mechanics and Physics of Solids 11, 155–179.

Dioh, N. N., Ivankovic, A., Leevers, P. S. and Williams, J. G. (1995). Stress Wave Propagation Effects in Split Hopkinson Pressure Bar Tests. Proceedings: Mathematical and Physical Sciences, 449(1936), 187-204.

Dobkin, D. and Kirkpatrick, D., (1985). A linear algorithm for determining the separation of convex polyhedra. Journal of Algorithms 6, 381-392.

Dong, A.A., Lu, Y. and Ma, G.W. (2006). Numerical simulation study of strain rate effect on dynamic behaviour of concrete material. Proc., DAPS-2006, Singapore.

Donze, F. V., Magnier, S.A., Daudeville, L., Mariotti, C. and L. Davenne, C. (1999). Numerical study of compressive behavior of concrete at high strain rates. Journal of Engineering Mechanics, 125(10), 1154-1163.

Dugdale, D. S. (1960). Yielding of sheets containing slits. Journal of Mechanics and Physics of Solids, 8, 100–104.

Eckardt, S., Hafner, S. and Konke, C. (2004). Simulation of the fracture behaviour of concrete using continuum damage models at the mesoscale. Proceedings of ECCOMAS 2004, Jyvaskyla, Finland.

Edelsbrunner, H. (1987). Algorithms in Combinatorial Geometry. Springer.

Follansbee, P.S. (1985). The Hopkinson Pressure Bar, Mechanical Testing. ASM Handbook American Society for Metals.

Forrestal, M.J., Wright, T.W. and Chen, W. (2007). The effect of radial inertia on brittle samples during the split Hopkinson pressure bar test. International Journal of Impact Engineering, 34, 405–411.

Frocht, M.M. (1948). Photoelasticity. John Wiley, New York.

Garboczi, E.J., and Bentz, D.P. (1997). Analytical formulas for interfacial transition zone properties. Journal of Advanced Cement Based Material, 6, 99-108.

Gary, G. (1990). Tests of high speed concrete-specific problems. Report distro specific GRECO, GRECO Publisher.

Georgin, J.F., Reynouard, J.M. and Merabet, O. (1998). Modeling of concrete at high strain rate. Computational Modeling of Concrete Structures, Rotterdam, 593–601.

Gomez, J., Shukla, A. and Sharma, A. (2001). Static and dynamic behaviour of concrete and granite intension with damage. Theoretical and Applied Fracture Mechanics, 36, 37–49.

Gong, J.C., Malvern, L.E. and Jenkins, D.A. (1990). Dispersion investigation in the split Hopkinson pressure bar. Journal of Engineering Materials and Technology, 112, 309–14.

Gorham, D.A. (1997) An empirical method of dispersion correction in the compressive Hopkinson Bar test. Journal of Physics IV France, C3-223.

Gray III, G.T. (2000). Classic Split Hopkinson Pressure Bar Testing. ASM Handbook Vol 8. Mechanical testing and evaluation. ASM. 462-476.

Grote, D.L., Park, S.W. and Zhou, M. (2001). Dynamic behavior of concrete at high strain-rates and pressures: I. Experimental characterization. International Journal of Impact Engineering, 25, 869–886.

Hafner, S., Eckardt, S., Luther, T. and Konke, C. (2006). Mesoscale modelling of concrete: Geometry and numerics. Computers and Structures, 84, 450–61.

Hillerborg, A., Modeer, M. and Petersson, P.E. (1976). Analysis of crack formation and crack growth in concrete by means of fracture mechanics and finite elements, Cement Concrete Res., 6, 773–782.

Hughes, M.L., Tedesco, W. and Ross, C.A. (1993). Numerical analysis of high strain rate splitting-tensile tests. Computers & Structures, 47, 653–71.

John, R., Antoun, T.and Rajendran, A.M. (1992). Effect of Strain Rate and Size on Tensile Strength of Concrete. APS Topical Conference on Shock Compression of Condensed Matter, Williamsburg, VA.

Kenmochi, Y., Imiya, A. and Ezquerra, N. (1996). Polyhedra generation from lattice points. Lecture Notes in Computer Science, 1176, 127-138

Leite, J.P.B., Slowik, V. and Mihashi, H. (2004). Computer simulation of fracture processes of concrete using mesolevel models of lattice structures. Cement and Concrete Research, 34(6), 1025–33.

Li, Q.M., Lu, Y.B. and Meng, H. (2009). Further investigation on the dynamic compressive strength enhancement of concrete-like materials based on split Hopkinson pressure bar tests. Part II: Numerical simulations. Int. J. Impact Eng. 6, 1335–1345.

Li, Q.M. and Meng, H. (2003). About the Dynamic strength enhancement of concrete like materials in a split Hopkinson pressure bar test. Int J Solids and Structures, 40, 343-360.

Lilliu, G. and van Mier, J.G.M. (2003) 3D lattice type fracture model for concrete. Engineering Fracture Mechanics, 70(7–8), 927–941

Lohner, R. (1996). Progress in Grid Generation via the Advancing Front Technique. Engineering with Computers, 12, 186-210.

LS-DYNA Keyword User's Manual-version 971. (2007). Livermore Software Tech. Co.

Lu, Y. and Tu, Z.G. (2008). Simulation of concrete fragmentation with a mesoscale approach. 4th International Conference on Advances in Structural Engineering and Mechanics, Jeju, Korea.

Lu, Y., Song, Z.H. and Tu, Z.G. (2009). Numerical simulation study of the strain rate effect on concrete in compression considering material heterogeneity. Proc., DYMAT 2009, Brussels, Belgium.

Lu, Y., Song, Z.H. and Tu, Z.G. (2010). Analysis of dynamic response of concrete using a mesoscale model incorporating 3D effects. International Journal of Protective Structures, 1(2), 197-217.

Lu, Y. and Xu, K. (2004). Modelling of concrete materials under blast loading. International Journal of Solids and Structures, 41(1), 131-143.

Malvar, L.J. and Crawford, J. E. (1998). Dynamic increase factors for concrete. Twenty-Eighth DDESB Seminar, Orlando, FL.

Malvar, L.J., Crawford, J.E. and Wesevich, J.W. (1997). A plasticity concrete material model for DYNA3D. International Journal of Impact Engineering, 19(9/10), 847–73.

Maso, J.C. (1980). The Bond Between Aggregates and Hydrated Cement Pastes. Proceedings 7th International Congress on the Chemistry of Cement.

Mellinger, F.M. and Birkimer, D.L., (1966). Measurement of Stress and Strain on Cylindrical Test Specimens of Rock and Concrete under Impact Loading. Technical Report 4-46, U.S. Army Corps of Engineers.

Meng, H. and Li, Q.M. (2003a). An SHPB set-up with reduced time-shift and pressure bar length. International Journal of Impact Engineering, 28, 677–696.

Meng, H. and Li, Q.M. (2003b). Correlation between the accuracy of a SHPB test and the stress uniformity based on numerical experiments. International Journal of Impact Engineering, 28, 537–555.

Mindness S., Young,F. and Darwin, D.(2002) Concrete. Prentice Hall.

Mishnaevsky Jr, L. (2006). Mesostructural effects on damage in composites: computational analysis, Journal of Theoretical and Applied Mechanics, 3(44), 533-552.

Muller, D. and Preparata, F. (1978). Finding the intersection of two convex polyhedra. Theoretical Computer Sciences, 7, 217-236.

Mogi, K. (2006). Experimental rock mechanics. Taylor & Francis Group.

Neville, A.M. (1995). Properties of concrete. Pitman.

Owen, S.J. (1998). A Survey of Unstructured Mesh Generation Technology. Proceedings 7th International Meshing Roundtable.

Pankow, M., Attard, C. and Waas, A.M. (2009). Specimen size and shape effect in split Hopkinson pressure bar testing. Journal of Strain Analysis, 44, 689-698.

Park, S.W., Xia, Q. and Zhou, M. (2001). Dynamic behavior of concrete at high strain rates and pressures: II. Numerical simulation. International Journal of Impact Engineering, 25, 887–910.

Reinhardt, H.W. (1984). Tensile Fracture of Concrete at High Rates of Loading. Application of Fracture Mechanics to Cementitious Composites, S.P. Shah editor,559-590.

Riedel, W., Wicklein, M and Thoma, K. (2008). Shock properties of conventional and high strength concrete: Experimental and mesomechanical analysis. International Journal of Impact Engineering, 35, 155–171.

Riedel, W., Kawai, N., and Kondo, K. (2009). Numerical assessment for impact strength measurements in concrete materials. International Journal of Impact Engineering, 36, 283–293.

Rodriguez, J., Navarro, C. and Sanchez-Galvez, V. (1994). Splitting tests: an alternative to determine the dynamic tensile strength of ceramic materials. Journal de Physique IV 4(c8),101-106.

Roelfstra, P. E., Sadouki, H. and Wittmann, F. H. (1985). Le beton numerique. Materials Structures,18, 327–335.

Ross, C.A. (1991). Fracture of Concrete at High Strain Rate. Proceedings-NATO Advanced Research Workshop: Toughening Mechanism in Quasi-Brittle Materials, Evanston, Illinois.

Ross, C.A. (1998). Effects of strain rate and moisture on then tensile strength of heterogeneous materials. Internal Report, University of Florida.

Ross, C.A., Jerome, D.M., Tedesco, J.W. and Hughes, M.L. (1996). Moisture and Strain Rate Effects on Concrete Strength. ACI Materials Journal, 93(3), 293-300.

Ross, C.A., Tedesco, J.W. and Kuennen, S.T. (1995). Effects of strain rate on concrete strength. ACI Materials Journal, 92, 75–81.

Ross, C.A., Thompson, P.Y. and Tedesco, J.W. (1989). Split-Hopkinson Pressure-Bar Tests on Concrete and Mortar in Tension and Compression. ACI Materials Journal, 86(5), 475-481.

Ruiz, G., Ortiz, M. and Pandol, A. (2000). Three-dimensional finite-element simulation of the dynamic Brazilian tests on concrete cylinders. International Journal of Numerical Method and Engineering, 48, 963-994

Schlangen, E., van Mier, J. (1992). Simple lattice model for numerical simulation of fracture of concrete materials and structures. Materials and Structures, 25, 534-542.

Scrivener, K. (1999). Characterization of the ITZ and its quantification by Test Methods. Engineering and Transport Properties of the Interfacial Transition Zone in Cementitious Composites, RILEM Publications.

Si, H. (2006). Tetgen: A Quality Tetrahedral Mesh Generator and a 3D Delaunay Triangulator User's Manual.

Si, H. and Gartner, K. (2004). An Algorithm for Three-Dimensional Constrained Delaunay Tetrahedralizations. Proceeding of the Fourth International Conference on Engineering Computational Technology, Lisbon, Portugal.

Si, H. and Gartner, K. (2005). Meshing Piecewise Linear Complexes by Constrained Delaunay Tetrahedralizations. Proceeding of the 14th International Meshing Roundtable.

Tedesco. J.W and Landis, D.W. (1989). Wave propagation through layered system. Computers and Structures, 32, 3-4.

Tedesco, J.W. and Ross, C.A. (1998). Strain-rate-dependent constitutive equations for concrete. ASME Journal of Pressure Vessel Technology, 120, 398–405.

Tedesco, J.W., Ross, C.A. and Brunair, R.M. (1989). Numerical Analysis of Dynamic Split Cylinder Tests. Computers and Structures, 32(3/4), 609-624.

Tu, Z.G. and Lu, Y. (2009). Evaluation of typical concrete material models used in hydrocodes for high dynamic response simulations. International Journal of Impact Engineering, 36, 132-146.

Tu, Z.G. and Lu, Y. (2011). Mesoscale modeling of concrete for static and dynamic response analysis Part 1: model development and implement. Structural Engineering and Mechanics, 37, 197-213.

van Mier, J.G.M. (1996). Fracture Process of Concrete. Taylor & Francis.

van Vliet, M. R. A. and van Mier, J. G. M. (1996). Experimental investigation of concrete fiacture under uniaxial compression. Mechanics of Cohesive-Frictional Materials, 1(1), 115- 127.

Vonk, R. (1992). Softening of concrete loaded in compression. PhD thesis, Eindhoven Univ. of TechnoI., Eindhoven, The Netherlands.

Wang, Q.Z., Li, W. and Song, X.L. (2006). A method for testing dynamic tensile strength and elastic modulus of rock material using SHPB. Pure Applied Geophysics, 163, 1091–100.

Wang, Z.M., Kwan, A.K.H., and Chan. H.C. (1999). Mesoscopic study of concrete I: generation of random aggregate structure and finite element mesh. Computers and Structures, 70, 533-544.

Weerheijm, J. and Reinhardt, H.W. (1989). Modelling of Concrete Fracture under Dynamic Tensile Loading, Fracture of Concrete and Rock - Recent Developments. 721-728.

Wittmann, F.H., Roelfstra, P.E. and Sadouki, H. (1984). Simulation and analysis of composite structures. Material Sciences & Engineering, 68, 239-248.

Wriggers, P. and Moftah, S.O. (2006). Mesoscale models for concrete: Homogenisation and damage behaviour. Finite Elements in Analysis and Design, 42, 623-636.

Yu, Y.B. and Li, Q.M. (2011). Aout the dynamic uniaxial tensile strength of concrete like materials. International Journal of Impact Engineering, 38, 171-180.

Zhang, M., Wu, H.J., Li, Q.M. and Huang, F.L. (2009). Further investigation on the dynamic compressive strength enhancement of concrete-like materials based on split Hopkinson pressure bar tests, Part-I: experiments. International Journal of Impact Engineering, 36(12),1327-1337

Zhao, H. and Gary, G. (1996). On the use of SHPB techniques to determine the dynamic behavior of materials in the range of small strains. International Journal of Solids and Structures, 33, 3363–3375.

Zhao, H. and Gary, G. (1997). A new method for the separation of waves: application to the SHPB technique for an unlimited duration of measurement. Journal of the Mechanics and Physics of Solids, 45, 1185–202.

Zhou, X.Q. and Hao, H. (2008a). Mesoscale modelling of concrete tensile failure mechanism at high strain rates. Computers and Structures, 86,2013-2026.

Zhou, X.Q. and Hao, H. (2008b). Modelling of compressive behaviour of concrete-like materials at high strain rate. International Journal of Solids and Structures, 45, 4648–4661.

Zhou, X.Q. and Hao, H. (2009). Mesoscale modelling and analysis of damage and fragmentation of concrete slab under contact detonation. International Journal of Impact Engineering, 36(12), 1315-1326.

Zubelewicz, A. and Bazant, Z. P. (1987). Interface element modeling of fracture in aggregate composites. Journal of Engineering Mechanics, 113(11), 1619–1630.